國立交通大學

物理研究所

博士論文

I. 低維半導體中的電子自旋馳豫 和
II. 微生物鞭毛間的流體動力交互作用

I. Spin relaxations in low dimensional semiconductors and
II. Hydrodynamic interactions between microorganism flagella

研 究 生：蔡政展

指導教授：張正宏 教授

中華民國一百零貳年七月

I. 低維半導體中的電子自旋馳豫 和
II. 微生物鞭毛間的流體動力交互作用
I. Spin relaxations in low dimensional semiconductors and
II. Hydrodynamic interactions between microorganism flagella

研究生：蔡政展　　Student：Jengjan Tsai

指導教授：張正宏　　Advisor：Cheng-Hung Chang

國立交通大學
物理研究所
博士論文

A Thesis
Submitted to Institute of Physics
College of Science
National Chiao Tung University
in partial Fulfillment of the Requirements
for the Degree of
Doctor
in

Physics

July 2013

Hsinchu, Taiwan, Republic of China

中華民國一百零貳年七月


E
S
A
1896

I. 低維半導體中的電子自旋馳豫 和
II. 微生物鞭毛間的流體動力交互作用

學生：蔡政展　　　　　　　　　　　　　　　指導教授：張正宏

國立交通大學物理研究所博士班

摘　　要

在這篇論文中，我們主要探討兩個主題：I．低維半導體中的電子自旋馳豫 II．微生物鞭毛間的流體動力交互作用。這兩個主題分別隸屬於凝態和軟物質兩個不同的物理領域。

在主題 I 中，我們探究低維半導體 (二維電子氣) 中，基於 Elliott-Yafet 和 D’yakonov-Perel’ 自旋馳豫機制所導致的電子自旋馳豫現象。我們運用 Ensemble Monte Carlo (EMC) 和 Semiclassical path integral (SPI) 方法來研究這些問題。藉由運用 EMC 和 SPI 這兩個方法來加以計算，我們發現其結果與一些理論推演和實驗數據互相一致。並且我們也預測出一些有趣的結果，這些發現可作為將來實驗設計的指導方針。

在主題 II 中，我們試著揭露出細菌地毯鞭毛運動的集體行為。我們提出兩個簡單模型 Microorganism-flagellum-rotor matrix ($\mathrm{MFR}_{\mathrm{matrix}}$) 和 Microorganism-flagellum-rotor sweep ($\mathrm{MFR}_{\mathrm{sweep}}$) 來摹擬真實世界中複雜萬分的細菌鞭毛轉動和甩動的行為。我們使用 Blake-Oseen tensor (BOT) 來描述細菌鞭毛彼此之間和鞭毛與示蹤粒子之間的流體動力交互作用。藉由運用 $\mathrm{MFR}_{\mathrm{matrix}}$ 和 $\mathrm{MFR}_{\mathrm{sweep}}$ 這兩個模型以及 BOT 來研究微生物鞭毛陣列的行為，我們提出一些合理的見解來解釋最近的一些實驗結果。此外我們也預測出一些有趣的現象，這些發現可作為將來實驗設計的指導方針。

I. Spin relaxations in low dimensional semiconductors and
II. Hydrodynamic interactions between microorganism flagella

student：Jengjan Tsai　　Advisors：Dr. Cheng-Hung Chang

Institute of Physics
National Chiao Tung University

ABSTRACT

In this thesis we explore two main topics: I. Spin relaxations in low dimensional semiconductors and II. Hydrodynamic interactions between microorganism flagella. These two topics belong to two different physical fields, condensed matter and soft matter fields.

In Part I we focus on exploring the Elliott-Yafet and D'yakonov-Perel' spin relaxation mechanisms inducing electron spin relaxation in low dimensional semiconductors (two-dimensional electron gas). The main exploration approaches are Ensemble Monte Carlo (EMC) and Semiclassical path integral (SPI) methods. By utilizing these two methods, some consistent results between our study and some theoretical and experimental results are obtained. In addition our study also predicts some interesting findings which may offer as design guidance for future experiments setting up.

In Part II we try to reveal the bacterial carpet collective behavior. We propose two minimal models Microorganism-flagellum-rotor matrix ($\mathrm{MFR}_{\mathrm{matrix}}$) and Microorganism-flagellum-rotor sweep ($\mathrm{MFR}_{\mathrm{sweep}}$) to mimic the real and complex bacterium flagella rotation and sweep behavior, respectively. And in order to properly describe the hydrodynamic interaction between the bacterium flagella themselves and between the bacterium flagellum and tracer particle, the hydrodynamic interaction Blake-Oseen tensor (BOT) is employed. By utilizing these two models and BOT in studying microorganism matrix, we give some reasonable explanation to account for recent experimental results. Besides, our study also predicts some interesting findings which may offer as design guidance for future experiments setting up.

誌謝

Academic adventure is an interesting and a so long road… I think that cost some time of my life in this adventure is a worth thing… Thanks to the so many teachers, classmates, friends, and my family, who care me, support me and take a walk with me during such a little bit long PhD research career… Thank you so much!

At present, I finish this PhD program, and shall enter into a new field in my life… Wish myself can go ahead, go better, and go success in near future~~ Well…, all my friends, thank you so much~~ Good bye~~

Contents

I Spin Relaxations In Low Dimensional Semiconductors 1

List of Figures

Part I

Spin Relaxations In Low Dimensional Semiconductors

Chapter 1

Spin Relaxation Mechanisms

1.1 Introduction

The achievement of modern science and technology is largely based on the blooming development of electronics, which mainly make use of the charge property of carriers in solid state physics. However, charge is not the only intrinsic carrier property one can take advantage of from carriers. In addition to it, spin is a not yet widely utilized degree of freedom which may enrich device functions. Sophisticated manipulation on the carrier charge has revolutionized our daily life over a century. The possibility of utilizing carrier spin creates another hope for a new generation of spin-based devices. This expectation has attracted numerous studies in the past decades and boosted our understanding on spin systems in solid state physics. Researches along this direction have formed the field of spin electronics, or simply spintronics.

The expectation for a spin technology era is not a pure mirage. In fact, some spin-based devices have been realized and even in use commercially. A prominent example is the read head and the memory-storage cell of the giant-magnetoresistive (GMR) multilayer structure, composed of alternating ferromagnetic and nonmagnetic metal layers, developed around 1988 [1,2]. Since the magnetoresistance of the device depends on the relative orientation of the magnetizations in the magnetic layers, it can be used to sense changes in magnetic fields. After GMR, the studies on spintronics devices have split into two branches. While one of them tends to perfect the existing GMR-based technology, the other seeks more radically for new mechanisms for tailoring desired spin transport properties from, for instance, semiconductors. The idea of spin field-effect-transistor proposed by Datta and Das for semiconductors served as a milestone example, which stimulates extensive theoretical and numerical studies in spintronics [3]. Despite of those promising progresses, the route towards a spin era of technology is not obstacle free. From the aspect of basic physics, spin flipping energy can be readily affected by thermal fluctuations. How to retain a spin information unaffected against thermal fluctuations and extract a spin information from the noisy environment are tricky problems. Without a solution to these problems, spintronics is only a laboratory toy at low temperature environments and cannot be coupled into daily used electric circuits functioning at the room temperature. Furthermore, from the aspect of material science, band unmatching on the metal-semiconductor interface and the fast spin relaxation rate in semiconductors are other notorious problems for device designs. As a whole, problems in constructing spin-based semiconductor devices can be summarized into three key issues: spin injection, detection, and manipulation [4]. During spin manipulation, the life time of a polarized spin state is of special concern, which leads to numerous investigations on various spin relaxation mechanisms. The importance of life time of spin state can be reflected from the recent interest on the persistent spin mode experimentally created and measured by IBM scientists in 2012 [5]. These spin helices of synchronized electrons persisting for more than a nanosecond is longer than the duration of a modern processor clock cycle, which is regarded as a hope for spin information processing. In fact, the existence of a similar kind of long-lived spin mode along a quasi one-dimensional system has been analytically proved and numerically confirmed in our previous study [6]. Doubtlessly, spin relaxation is a central problem in spintronics. It is the main ingredient in Part I of this thesis.

The samples studied in this thesis are focused on low-dimensional systems, such as quasi-two dimensional (quasi-2D) quantum wells (QWs) and quantum wires (QWires), as well as two dimensional electron gas (2DEG), built of III-V semiconductor heterostructures. Spin evolutions in these systems are strongly affected by the Elliott-Yafet and the D'yakonov-Perel' spin relaxation mechanisms. To analyze these mechanisms, we employee the Ensemble Monte Carlo Method for carrier dynamics and develop the Semiclassical Path Integral Method for spin dynamics. Our theoretical results agree very well with the existing experimental data, unravel some experimental puzzling questions, and predict several sample behaviors beyond experimentally accessible parameters regimes.

The spin relaxation, or spin de-coherence, of electrons and holes are frequently observed phenomenon in solid materials. There exist many relaxation mechanisms responsible for this phenomenon. The most prominent ones are the Elliott-Yafet(EY) mechanism [7, 8, 9, 10], the D'yakonov-Perel'(DP) mechanism [11, 12, 13, 14, 15], the Bir-Aronov-Pikus (BAP) mechanism, and the hyperfine-interaction

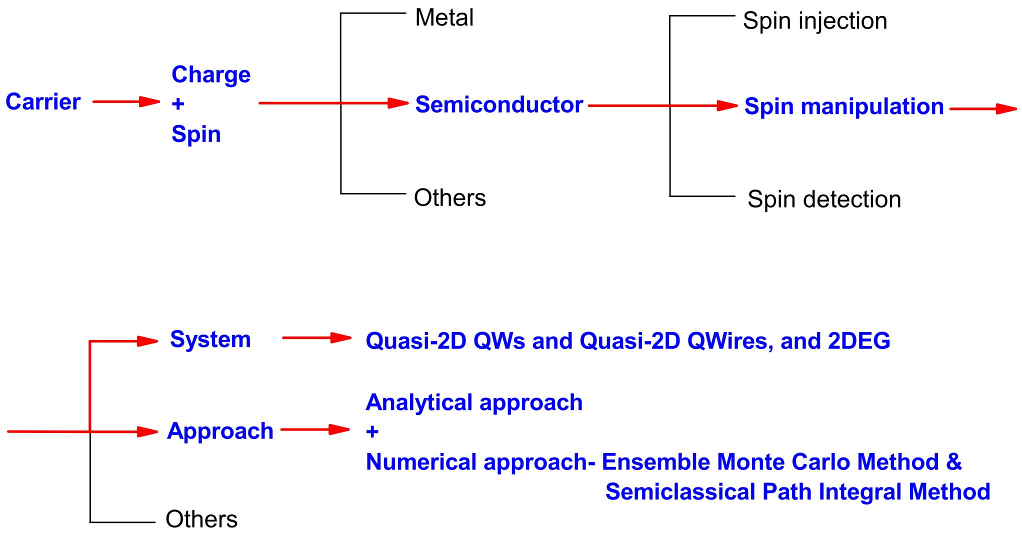

Figure 1.1: A tree plot shows the main concepts and key words which is included in Chapters 1 and 2. They highlight the necessary theoretical foundation and our study approaches in the spin relaxation issue which explored in Part I.

mechanisms. In this chapter we briefly sketch the EY and DP mechanisms.

1.2 Elliott-Yafet mechanism

An electron in a crystal is usually modeled as a particle moving in a perfect lattice described by a periodic lattice potential. The Schrödinger equation of the electron is

$$\left[\frac{\mathbf{p}^2}{2m} + V(\mathbf{r})\right]\Psi = E\Psi, \tag{1.1}$$

where m, $\mathbf{p}$ and $\mathbf{r}$ are the free electron mass, momentum operator and position vector. Here, $V(\mathbf{r})$ is the lattice potential, which follows both point and translational symmetries of the lattice. The wave function Ψ is the well-known Block function

$$u_k e^{i\mathbf{k}\cdot\mathbf{r}}, \tag{1.2}$$

where u_k obeys the above both symmetries of the lattice. In order to introduce the spin-orbit interaction into (2.1), we start with the four-component Dirac equation and reduce it to two components in the usual way [16]. After taking some approximations, it yields the Schrödinger equation

$$\left[\frac{\mathbf{p}^2}{2m} + V(\mathbf{r}) + \frac{\hbar}{4m^2c^2}(\nabla V(\mathbf{r}) \times \mathbf{p}) \cdot \boldsymbol{\sigma}\right]\Psi = E\Psi, \tag{1.3}$$

where c and $\boldsymbol{\sigma}$ are the speed of light and Pauli matrices and the third term is the spin-orbit coupling. The corresponding Hamiltonian operator and the wave functions of the electron still have the point and translational symmetries of the lattice. Since the spin-orbit coupling is present in this Hamiltonian, the eigenfunctions Ψ will be linear combinations of different spin functions,

$$[a_k|S_z+\rangle + b_k|S_z-\rangle]\, e^{i\mathbf{k}\cdot\mathbf{r}}, \tag{1.4}$$

where a_k and b_k are two functions with the same symmetry as $V(\mathbf{r})$ and u_k and the spin states $|S_z\pm\rangle$, which have the angular momentum $\pm\frac{1}{2}\hbar$ along the $\mathbf{z}$ direction. The system we are interested in contains two kinds of symmetries: the inversion symmetry of space and the time-reversal symmetry. Combining the former, which changes wave vector from $\mathbf{k}$ into $-\mathbf{k}$, with the latter, which flips the spin states, it yields another set of eigenfunctions with the same $\mathbf{k}$ and energy,

$$[a_{-k}{}^*|S_z-\rangle - b_{-k}{}^*|S_z+\rangle]\, e^{i\mathbf{k}\cdot\mathbf{r}}. \tag{1.5}$$

The expressions (2.4) and (2.5) indicate that if the spin-orbit interaction (the third term in (2.3)) is present, the eigenfunctions of the Schrödinger equation (2.3) are generally no longer a pure spin state. It makes sense to call the eigenfunctions (2.4) and (2.5) the spin-up (+) and spin-down (−) states, respectively, since typically $|a_k|$ and $|a_{-k}| \approx 1$ and $|b_k|$ and $|b_{-k}| \ll 1$.

In the EY mechanism, the spin can be flipped only when its carrier collides with impurities. To discuss this process, let us consider an extra interaction H_{int} for scattering, which can be caused by the impurities, heavy holes, phonons, piezo-acoustic modes, or boundaries, etc. [7,8,9]. If H_{int} scatters the electron from $\mathbf{k}$ to $\mathbf{k}'$ without changing its spin, its matrix element is

$$\int a_{k'}{}^* H_{\text{int}}\, a_k\, e^{i(\mathbf{k}-\mathbf{k}')\cdot\mathbf{r}} d\mathbf{r}. \tag{1.6}$$

If H_{int} can cause spin flip, the matrix element must be replaced by

$$\int (a_{-k'} H_{\text{int}} b_k - b_{-k'} H_{\text{int}} a_k) e^{i(\mathbf{k}-\mathbf{k}')\cdot\mathbf{r}} d\mathbf{r}. \tag{1.7}$$

The transition rate is proportional to the square of the matrix elements of an interaction H_{int} between the electron and the impurity or the lattice as represented in Appendix and the reference paper therein [17]. For a collision process without spin change, the transition rate is related to the electron momentum relaxation time τ_p by

$$\frac{1}{\tau_p} \propto \left| \int (a_{k'}{}^{*} H_{\mathrm{int}} a_k) e^{i(\mathbf{k}-\mathbf{k}')\cdot\mathbf{r}} d\mathbf{r} \right|^2 . \tag{1.8}$$

If this process contains spin flip, the rate is

$$\frac{1}{2T_1} \propto \left| \int \left(a_{-k'} H_{\mathrm{int}} b_k - b_{-k'} H_{\mathrm{int}} a_k \right) e^{i(\mathbf{k}-\mathbf{k}')\cdot\mathbf{r}} d\mathbf{r} \right|^2 , \tag{1.9}$$

where T_1 is the spin relaxation time, which is also referred to the longitudinal time or spin-lattice time [18].

1.3 D'yakonov-Perel' mechanism

In the discussion of EY mechanism in Sec. 2.1, the combined effect of inversion symmetry of space and time reversal symmetry yields a twofold degeneracy of single-particle energies

$$E_+(\mathbf{k}) = E_-(\mathbf{k}), \tag{1.10}$$

where for convenience $(+)$ and $(-)$ denote the two states (2.4) and (2.5). If the spatial inversion symmetry is lifted, the spin-orbit interaction shall lead to a spin splitting of the electron state even at zero magnetic field, $B = 0$. The spin splitting can be caused by the bulk inversion asymmetry (BIA) of the underlying crystal structure. Examples include the zinc blende structure of III-V (such as GaAs and InSb) and II-VI (such as ZnSe and HgCdTe) compounds without center of inversion. These materials are different from Si and Ge, which have a diamond structure. Furthermore, the spin splitting can be caused by the structure inversion asymmetry (SIA) of the confined potential $V(\mathbf{r})$. This potential may contain a built-in or an external potential, as well as the effective potential from the position-dependent band edges. To the lowest order of the wave vector $\mathbf{k}$, the BIA induced spin splitting is caused by the so-called Dresselhause term, whereas the SIA induced one is generated by the so-called Rashba term. The spin splitting of higher orders of $\mathbf{k}$ can be described by, for instance, the 8×8 or the 14×14 extended Kane model.

For BIA, examples can be found in the conduction bands Γ-point of [001] grown GaAs/AlAs and alike (type-I) quasi-2D quantum wells or two dimensional electron gas (2DEG) systems. In these systems, the Hamiltonian matrix $H_{k_\parallel}$ of the Dresselhause term is

$$H_{k_{\parallel}}=\begin{bmatrix} E_c+\tilde{e}+\frac{\gamma}{2}\tilde{k}_z(k_x^2-k_y^2) & \frac{\gamma}{2}\left[\tilde{k}_z^2(k_x+ik_y)-ik_xk_y(k_x-ik_y)\right] \\ \frac{\gamma}{2}\left[\tilde{k}_z^2(k_x-ik_y)+ik_xk_y(k_x+ik_y)\right] & E_c+\tilde{e}-\frac{\gamma}{2}\tilde{k}_z(k_x^2-k_y^2) \end{bmatrix}, \tag{1.11}$$

where E_c is the energy at the bottom of the conduction band, $\tilde{e} = \hbar^2/2m^*(k_x^2 + k_y^2 + \tilde{k}_z^2)$ is the energy operator, k_x and k_y are the electron momenta in $\mathbf{x}$ and $\mathbf{y}$ directions, m^* is the Γ-point conduction-band effective electron mass, γ is the spin-splitting parameter, and $\tilde{k}_z$ is the operator id/dz [19, 20]. This Hamiltonian can be reduced as

$$H_{BIA} = \beta\left[\sigma_x k_x\left(k_y^2-\langle k_z^2\rangle\right)+\sigma_y k_y\left(\langle k_z^2\rangle-{k_x}^2\right)\right], \tag{1.12}$$

with a material-specific coefficient β, where σ_x and σ_y are two components of the Pauli matrices.

For SIA, examples can also be found in the conduction bands Γ-point of [001] grown GaAs/AlAs and alike (type-I) quasi-2D quantum wells or two dimensional electron gas (2DEG) systems. In these systems, the Hamiltonian matrix $H_{k_{\parallel}}$ of the Rashba term is

$$H_{k_{\parallel}} = \alpha\left(\boldsymbol{\sigma}\times\mathbf{k}\right)\cdot\boldsymbol{\nu}, \tag{1.13}$$

where α is a pre-factor which depends on the constituting materials and on the geometry of the quasi-2D or 2DEG systems, $\boldsymbol{\sigma}$ are the Pauli matrices, $\hbar\mathbf{k}$ is the electron momentum, and $\boldsymbol{\nu}$ is a unit vector perpendicular to the 2D plane. If we assume that $\boldsymbol{\nu}$ is in the $\mathbf{z}$ direction, then this Hamiltonian becomes

$$H_{SIA} = \alpha\left(\sigma_x k_y-\sigma_y k_x\right). \tag{1.14}$$

A comparison shows that the energy degeneracy of spin orbit interaction or the quasi-spin up and down states can be lifted in different ways in BIA and SIA. The former can be achieved by removing spatial inversion symmetry or time reversal symmetry, while the latter can be accomplished by applying an external magnetic field. The expressions (1.12) and (1.14) have a general form

$$H_{SOI} = \frac{1}{2}\hbar\boldsymbol{\sigma}\cdot\boldsymbol{\Omega}(\mathbf{k}), \tag{1.15}$$

where SOI denotes the spin orbit interaction, $\boldsymbol{\sigma}$ are the Pauli matrices, $\mathbf{B}(\mathbf{k})$ is a $\mathbf{k}$-dependent effective magnetic field around which electron spins precess with the Larmar frequency $\mathbf{\Omega}(\mathbf{k}) = (e/m^*)\mathbf{B}(\mathbf{k})$, with the effective electron mass m^* [12,13,15]. This expression gives a clear picture why the effective magnetic field $\mathbf{B}(\mathbf{k})$ causes the electron spin relaxation. That is, a collision event will change the electron momentum $\hbar\mathbf{k}$ and subsequently the electron spin precession axis. Therefore, the randomized precession axis will help smearing the electron spin coherence. If the momentum relaxation time is longer than the spin precession period, e.g., under dilute impurities, the electron spins shall precess freely and lose their coherence between two collision events. In contrast, if the momentum relaxation time is shorter than the spin precession period, e.g., under dense impurities, the electron spins will not precess much before the carrier changes its momentum or the carrier spin changes its precession axis. It shall lead to the dynamical narrowing which helps preserving spin coherence.

Owing to different underlying mechanisms, the EY and DP spin relaxation times have opposite impurity density dependence. Under the EY mechanism, spin flip is a temporally discrete event and can only happen at a electron-impurity collision. Thus, more frequent collision events will cause faster spin relaxation. Under the DP mechanism, each single spin precesses between two collisions. Less collision events will lead to longer precession and faster spin decoherence. Accordingly, there exists a trend between the momentum relaxation time τ_p and the spin relaxation times τ_s^{EY} and τ_s^{DP} of EY and DP mechanisms, respectively

$$\tau_s^{EY} \propto \tau_p \quad \text{and} \quad \tau_s^{DP} \propto \frac{1}{\tau_p}. \tag{1.16}$$

1.4 Supplement: general definition of spin relaxation time

To study spin relaxations, let us consider a system consisting of N_+ electrons with spin state $|S_z+\rangle$ and N_- electrons with spin state $|S_z-\rangle$. The total electron number is $N = N_+ + N_-$ and the net magnetization at any instance can be defined as

$$D = N_+ - N_-. \tag{1.17}$$

If at equilibrium the net magnetization is D_{eq}, one expects that the evolution of D will follow the equation

$$\frac{dD}{dt} = \frac{D_{eq} - D}{T}, \tag{1.18}$$

with the relaxation time T. Let $N_{\mp\rightarrow\pm}$ be the number of spins which flip per second from $|S_z\mp\rangle$ to $|S_z\pm\rangle$ and $W_{\mp\rightarrow\pm}$ be the transition rate of electrons from $|S_z\mp\rangle$ to $|S_z\pm\rangle$. The evolution of D is then given by

$$\frac{dD}{dt} = \frac{D_{eq} - D}{T} = \frac{2\left(N_{-\rightarrow+} - N_{+\rightarrow-}\right)}{1} = 2\left(W_{-\rightarrow+} - W_{+\rightarrow-}\right). \tag{1.19}$$

These transition rates $W_{\mp\rightarrow\pm}$ are proportional to the square of the matrix elements of an interaction H_{int} between the electron and the impurity or the lattice that causes a spin flip [17].

Bibliography

[1] M. N. Baibich, J. M. broto, A. Fert, F. Nguyen Van Dau, F. Petroff, P. Etienne, G. Creuzet, A. friederich and J. Chazelas, Phys. Rev. Lett. **61**, 2472 (1988).

[2] G. Binasch, P. Grünberg, F. Saurenbach and W. Zinn, Phys. Rev. B **39**, 4828 (1989).

[3] S. Datta and B. Das, Appl. Phys. Lett. **56**(7), 665 (1990).

[4] I. Žutić, J. Fabian and S. Das Sarma, Rev. Mod. Phys. **76**, 323 (2004).

[5] M. P. Walser, C. Reichl, W. Wegscheider and G. Salis, Nature Physics **8**, 757 (2012).

[6] C.-H. Chang, J. Tsai, H.-F. Lo, A. G. Mal'shukov, Phys. Rev. B **79**, 125310 (2009).

[7] R. J. Elliott, Phys. Rev. **96**, 266 (1954).

[8] W. Zawadzki and W. Szymańska, Phys. Status Solidi (b) **45**, 415 (1971).

[9] G. Fishman and G. Lampel, Phys. Rev. B **16**, 820 (1977).

[10] F. Beuneu and P. Monod, Phys. Rev. B **18**, 2422 (1978).

[11] G. Dresselhause, Phys. Rev. **100**, 580 (1955).

[12] M. I. D'yakonov and V. I. Perel', Sov. Phys. JETP **33**, 1053 (1971).

[13] M. I. D'yakonov and V. I. Perel', Sov. Phys. Solid state **13**, 3023 (1972).

[14] Yu. A. Bychkov and E. I. Rashba, J. Phys. C: Solid State Phys. **17**, 6039 (1984).

[15] M. I. D'yakonov and V. Yu. Kachorovskii, Sov. Phys. Semicond. **20**(1), 110 (1986).

[16] E. U. Condon and G. H. Shortley, *The theory of atomic spectra* (Cambridge University Press, Cambridge, 1957).

[17] A. W. Overhauser, Phys. Rev. **89**, 689 (1953).

[18] I. Žutić, J. Fabian and S. Das Sarma, Rev. Mod. Phys. **76**, 323 (2004).

[19] N. E. Christensen and M. cardona, Solid State Commun. **51**, 491 (1984).

[20] R. Eppenga and M. F. H. Schuurmas, Phys. Rev. B **37**, 10923 (1988).

Chapter 2

Methods for Carrier Transport, Carrier Scattering, and Spin Evolution

Using full quantum mechanical approach to study the carrier transport, carrier scattering, and spin evolution of many-body systems in solids is a formidable task. To overcome this complexity, we introduce the Ensemble Monte Carlo (EMC) method and Semiclassical Path Integral to tackle these dynamical problems.

2.1 Carrier transport

When we consider the carrier transport, e.g., electron transport, in a semiconductor crystal, it is essentially an extremely complicated many-body problem. However, we can focus on the motion of an electron and approximate the effective influence of atomic nuclei and other electrons on the studied electron by a potential $V(\mathbf{r})$. Then the original many-body problem can be reduced to the problem of a single electron [1,2]. Under this reduction, $V(\mathbf{r})$ is still periodic with the same periodicity as that of the crystal lattice. The electronic state under such $V(\mathbf{r})$ can be obtained by solving the Schrödinger equation

$$\left[\frac{\mathbf{p}^2}{2m} + V(\mathbf{r})\right]\Psi(\mathbf{r}) = E\Psi(\mathbf{r}), \tag{2.1}$$

where m is the free electron mass, $\Psi(\mathbf{r})$ is the eigenfunction to be determined, and E is the energy eigenvalue. The Bloch theorem tells us that the solutions for a perfectly periodic potential have the form

$$\Psi_{\mathbf{k}}(\mathbf{r}) = u_{\mathbf{k},n}(\mathbf{r})e^{i\mathbf{k}\cdot\mathbf{r}} \tag{2.2}$$

where $u_{\mathbf{k},n}(\mathbf{r})$ is periodic with the same periodicity of $V(\mathbf{r})$, $\mathbf{k}$ is the wave vector of electron and n is the index of bands. Besides, the energy eigenvalue $E_{\mathbf{k},n}$ is periodic with the periodicity of the reciprocal lattice.

The relation between $E_{\mathbf{k},n}$ and $\mathbf{k}$, that is the energy band structure, can be expressed in one period of the reciprocal lattice because of the periodicity of $E_{\mathbf{k},n}$. Conventionally, the first Brillouin zone, which is a period centered about at the origin of the $\mathbf{k}$-space, is used to show the energy band structure. This structure is usually depicted along some significant crystallographic orientations, such as Λ, Δ, and Σ directions. The energy band structure reveals an energy region where electronic states can not be found. This forbidden energy region is termed the energy gap and electronic states are permitted above and below this gap. While the bands above the gap are the conduction bands, those below it are the valence bands. The energy separation between the minimum of the lowest conduction band and the maximum of the highest valence band is the band gap energy E_g. The band model offers the information about the energy levels of the band extremes and the relations between the electron energy $E_{\mathbf{k}}$ and the electron wave vector $\mathbf{k}$, described by various band parameters.

The structures near the conduction band minima and the valence band maxima are important, because carriers located near the band edges are responsible for the transport property. The conduction band near the minimum is frequently approximated by a quadratic function of $\mathbf{k}$. If the band minimum is located at $|\mathbf{k}| = 0$, $E_{\mathbf{k}}$ can be expressed as

$$E_{\mathbf{k}} = \frac{\hbar^2 k^2}{2m^*}, \tag{2.3}$$

where $k^2 = (k_x^2 + k_y^2 + k_z^2)$ and

$$\frac{1}{m^*} \equiv \frac{1}{\hbar^2}\frac{\partial^2 E_{\mathbf{k}}}{\partial k^2} \tag{2.4}$$

is the inverse of the effective mass. The $E_{\mathbf{k}}$ relation given by (2.3) shows that the electrons in a crystal behave just like electrons moving in a free space, except for a change in the mass. Here $\hbar\mathbf{k}$ plays the role of momentum, which is termed the crystal momentum. $E_{\mathbf{k}}$ represents the electron kinetic energy measured from the conduction band minimum. Such simple model is rather widely used for simplifying the calculation of carrier transport.

Since electrons in crystal behave just like electrons in free space, except for the change in the mass. This picture suggests that the motion of electrons in a crystal may be described by the classical equations of motion. The idea is valid when the potential energy felt by the electrons varies slowly compared to the crystal potential so that quantum mechanical effects such as reflection, interference and tunneling can be ignored. Following this concept, the classical motion of an electron can be described by the equation of motion based on its total energy Hamiltonian

$$H = E_{\mathbf{k}} + U, \tag{2.5}$$

where $E_{\mathbf{k}}$ is the kinetic energy and U is the potential energy. For an electron in a conduction band, one has

$$H = E_{\mathbf{k}} + E_c(\mathbf{r}), \tag{2.6}$$

where $E_{\mathbf{k}}$ represent the kinetic energy in terms of the crystal momentum and the effective mass and $E_c(\mathbf{r})$ is the conduction band minimum. Then the equations of motion of the system are the Hamiltonian dynamics

$$\frac{d\mathbf{k}}{dt} = -\frac{1}{\hbar}\nabla_{\mathbf{r}} H \tag{2.7}$$

$$\frac{d\mathbf{r}}{dt} = \frac{1}{\hbar}\nabla_{\mathbf{k}} H, \tag{2.8}$$

where $\nabla_{\mathbf{r}}$ is del operator with respect to position vector $\mathbf{r}$ and $\nabla_{\mathbf{k}}$ is the del operator with respect to wave vector $\mathbf{k}$. We can easily check that for the quadratic band, the group velocity $\mathbf{v} = d\mathbf{r}/dt$ simply gives

$$\mathbf{v} = \frac{\hbar\mathbf{k}}{m^*}, \tag{2.9}$$

which has the similar form of the free electron momentum divided by mass.

Due to the advances of modern semiconductor fabrication techniques, we can easily grow compositionally non-uniform heterostructure semiconductors. For instance, by placing two compositionally different materials next to each other, a heterojunction is established. A thin two-dimensional conducting layer, termed two dimensional electron gas (2DEG), is formed at the interface of the heterojunction, for example, the interface between GaAs and AlGaAs. Besides, with the use of modern epitaxial growth techniques, the alloy composition can be varied on an atomic scale, so a very sophisticated layer structures consisting of several barriers and wells can be fabricated. For example, a triple alloys compound AlGaAs-GaAs-AlGaAs offers a quantum well in the layer GaAs which the thickness of the well may be about 100Å or less. Because of the confined electron motion in the well, the electrons behavior just like a quasi-two dimensional motion. The electrons running at the thin two dimensional conducting layer or the confined well are called the two dimensional electron gas (2DEG). Studying 2DEG is important, since quantum confinements frequently exist in modern heterostructure devices.

Let us assume the aforementioned electron motion is confined in the **z** direction and the electron can move freely in the **xy** plane. The corresponding three-dimensional Schrödinger equation is

$$-\frac{\hbar^2}{2m^*}\nabla^2\Psi(\mathbf{r})+E_c(\mathbf{r})\Psi(\mathbf{r})=E\Psi(\mathbf{r}). \tag{2.10}$$

The strategy to solve (2.10) is trying to separate the variables. We assume the plane wave solutions in the **xy** direction since the electrons are free to move on the **xy** plane. So the total wave function is represented as

$$\Psi(\mathbf{r})=C\psi(z)e^{ik_xx}e^{ik_yy}, \tag{2.11}$$

where C is the normalization coefficient. Substituting (2.11) into (2.10), we get an equation for $\psi(z)$,

$$-\frac{\hbar^2}{2m^*}\frac{\partial^2\psi(z)}{\partial z^2}+E_c(z)\psi(z)=E_n\psi(z), \tag{2.12}$$

where

$$E_n=E-E_{\parallel} \tag{2.13}$$

is the energy associated with confinement in the **z** direction and $E_{\parallel}=\frac{\hbar^2}{2m^*}(k_x^2+k_y^2)$ is the kinetic energy associated with the motion parallel to **xy** plane.

2.2 Carrier scattering

Carrier motion in semiconductor crystals is mainly made up of the scattering and drift processes. Here we briefly introduce the theory for scattering process, which plays a role in our study. The scattering theory is based on Fermi's golden rule, which is derived from the first-order time-dependent perturbation theory. It gives the transition probability per unit time between two eigenstates of the unperturbed Hamiltonian H_0 caused by the perturbation potential $H'(\mathbf{r},t)$. While H_0 can be the free electron Hamiltonian in general, it is the effective mass electron

Hamiltonian in solid crystals. At first let us write down the Schrödinger equation

$$\left[H_0 + \lambda H'(\mathbf{r},t)\right]\Psi(\mathbf{r},t) = i\hbar\frac{\partial\Psi(\mathbf{r},t)}{\partial t}, \tag{2.14}$$

where λ is a real dimensionless parameter. We assume the equation for the unperturbed Hamiltonian H_0 has been solved as

$$H_0\psi_{\mathbf{k}} = E_{\mathbf{k}}\psi_{\mathbf{k}}, \tag{2.15}$$

where E_k is the energy eigenvalue and $\psi_{\mathbf{k}}$ is the corresponding eigenfunction. The time evolution of the eigenfunction can be represented as

$$\Psi^0_{\mathbf{k}}(\mathbf{r},t) = \psi_{\mathbf{k}}(\mathbf{r})e^{\frac{-iE_{\mathbf{k}}t}{\hbar}}. \tag{2.16}$$

Since the eigenfunctions $\Psi^0_{\mathbf{k}}(\mathbf{r},t)$ form a complete and orthonormal set, the solution of the perturbed problem can be constructed by the linear combinations of $\Psi^0_{\mathbf{k}}(\mathbf{r},t)$,

$$\Psi(\mathbf{r},t) = \sum_{\mathbf{k}} c_{\mathbf{k}}(t)\Psi^0_{\mathbf{k}}(\mathbf{r},t), \tag{2.17}$$

where the coefficient $c_{\mathbf{k}}(t)$ describes how the perturbation makes the component at $\Psi^0_{\mathbf{k}}(\mathbf{r},t)$ vary with time. Substituting (2.17) into (2.14) and multiplying both sides of the arranged equation by $\psi^*_{\mathbf{k}'}e^{\frac{-iE_{\mathbf{k}'}t}{\hbar}}$, integrating with respect to $\mathbf{r}$, and using the orthogonality of $\psi_{\mathbf{k}}$, we obtain the following differential equation for $c_{\mathbf{k}}(t)$

$$i\hbar\frac{\partial c_{\mathbf{k}'}(t)}{\partial t} = \lambda\sum_{\mathbf{k}}\langle\mathbf{k}'|H'|\mathbf{k}\rangle c_{\mathbf{k}}(t)e^{\frac{i(E_{\mathbf{k}'}-E_{\mathbf{k}})t}{\hbar}}, \tag{2.18}$$

where $\langle\mathbf{k}'|H'|\mathbf{k}\rangle$ is the expectation value defined as

$$\langle\mathbf{k}'|H'|\mathbf{k}\rangle = \int_\Omega \psi^*_{\mathbf{k}'}(\mathbf{r})H'\psi_{\mathbf{k}}(\mathbf{r})d\mathbf{r}, \tag{2.19}$$

with Ω the volume of the crystal.

The expression (2.18) indicates that $c_{\mathbf{k}}(t)$ depends on time if λ is not zero. Since $c_{\mathbf{k}}(t)$ is expected to vary slowly with time if the perturbation is weak, it can be expanded as a power series of λ,

$$c_{\mathbf{k}}(t) = c^{(0)}_{\mathbf{k}} + \lambda c^{(1)}_{\mathbf{k}}(t) + \lambda^2 c^{(2)}_{\mathbf{k}}(t) + \cdots. \tag{2.20}$$

Substituting (2.20) into (2.18) and equating terms of like powers of λ on the two sides, we have

$$\begin{array}{rcl} i\hbar\frac{\partial c^{(0)}_{\mathbf{k}'}(t)}{\partial t} & = & 0 \\ i\hbar\frac{\partial c^{(1)}_{\mathbf{k}'}(t)}{\partial t} & = & \sum_{\mathbf{k}}\langle\mathbf{k}'|H'|\mathbf{k}\rangle c^{(0)}_{\mathbf{k}} e^{\frac{i(E_{\mathbf{k}'}-E_{\mathbf{k}})t}{\hbar}} \\ i\hbar\frac{\partial c^{(2)}_{\mathbf{k}'}(t)}{\partial t} & = & \sum_{\mathbf{k}}\langle\mathbf{k}'|H'|\mathbf{k}\rangle c^{(1)}_{\mathbf{k}}(t) e^{\frac{i(E_{\mathbf{k}'}-E_{\mathbf{k}})t}{\hbar}} \\ & \vdots & \end{array} \tag{2.21}$$

The first equation of (2.21) shows that the zero-order coefficients $c^{(0)}_{\mathbf{k}'}$ are time independent. The first-order approximation $c^{(1)}_{\mathbf{k}'}(t)$ of $c_{\mathbf{k}'}(t)$ can be evaluated from the second equation of (2.21). The first-order approximation will be sufficient precise, provided that the interaction is very weak.

For an initial state in a definite unperturbed eigenstate $\mathbf{k}_i$, the above results give

$$\begin{array}{l} c_{\mathbf{k}'}(t) = c^{(0)}_{\mathbf{k}_i} = 1 \\ c_{\mathbf{k}}(t) = c^{(0)}_{\mathbf{k}} = 0, \ \text{for } \mathbf{k} \neq \mathbf{k}_i \end{array} \tag{2.22}$$

and subsequently

$$i\hbar\frac{\partial c^{(1)}_{\mathbf{k}'}(t)}{\partial t} = \langle\mathbf{k}'|H'|\mathbf{k}_i\rangle c_{\mathbf{k}}(t) e^{\frac{i(E_{\mathbf{k}'}-E_{\mathbf{k}_i})t}{\hbar}}. \tag{2.23}$$

As an application of (2.23), we consider a constant perturbation turned on at $t = 0$

$$H'(t) = \begin{cases} 0, & \text{for t<0} \\ H', & \text{for t}\geq\text{0.} \end{cases} \tag{2.24}$$

Substituting (2.24) into (2.23) and carrying out some integrations, we obtain

$$c^{(1)}_{\mathbf{k}'}(t) = \frac{1}{i\hbar}\langle\mathbf{k}'|H'|\mathbf{k}_i\rangle c_{\mathbf{k}}(t) e^{\frac{\omega t}{2}} \frac{\sin(\frac{\omega t}{2})}{\left(\frac{\omega t}{2}\right)} t, \tag{2.25}$$

where $\omega = \frac{(E_{\mathbf{k}'}-E_{\mathbf{k}_i})}{\hbar}$. The probability of finding an electron with the wave vector $\mathbf{k}'$ at time t is then given by $|c^{(1)}_{\mathbf{k}'}(t)|^2$. Thus, the transition rate $S(\mathbf{k}_i, \mathbf{k}')$ from the state $\mathbf{k}_i$ to the state $\mathbf{k}'$ is

$$S(\mathbf{k}_i, \mathbf{k}') = \lim_{t\to\infty} \frac{|c^{(1)}_{\mathbf{k}'}(t)|^2}{t}. \tag{2.26}$$

By using the relation $\lim_{t\to\infty} \frac{1}{\pi}\frac{\sin^2 \alpha x}{\alpha x^2} = \delta(x)$, the transition rate becomes

$$S(\mathbf{k}_i, \mathbf{k}') = \frac{2\pi}{\hbar}\left|\langle\mathbf{k}'|H'|\mathbf{k}_i\rangle\right|^2 \delta(E_{\mathbf{k}'} - E_{\mathbf{k}_i}). \tag{2.27}$$

Integrating $S(\mathbf{k}_i, \mathbf{k}')$ given by (2.27), with respect to all accessible final states $\mathbf{k}'$, we obtain the scattering rate,

$$W(\mathbf{k}) = \frac{\Omega}{(2\pi)^3} \int S(\mathbf{k}_i, \mathbf{k}') d\mathbf{k}. \tag{2.28}$$

This formula is independent of the dimension of the systems. For quasi 2DEG, we need only to put the wave function given by (2.11) to obtain the corresponding scattering formula.

2.3 Ensemble Monte Carlo method

The Monte Carlo transport calculation is usually referred to the single particle Monte Carlo method or the ensemble Monte Carlo *(EMC)* method. As discussed above, carrier transport in a semiconductor crystal is a many-body problem with a huge number of mutually interacting carriers. However, if in some parameter regimes the carriers can be approximately treated as an ensemble of independent carriers, the macroscopic behaviors of the system might be approached by the long time behavior of a single particle. It is the principal idea of the single particle Monte Carlo method. This method is a useful for calculating carrier transport, especially in the case of steady-state carrier transport under a static and uniform electric field. However, if the problems of interest are not steady, the long time average has to be replaced by ensemble average, which gives rise to the ensemble Monte Carlo method. This method can be used more widely for many other purposes, such as carrier diffusion, the carrier transport in an inhomogeneous field, the non-stationary behavior of carriers, etc. In the study of spin evolution, we need to use the ensemble Monte Carlo method to monitor the transient process of electron spin. But each member, i.e., single particle, in the ensemble follows the same calculation process as that in the single particle Monte Carlo method.

The ensemble Monte Carlo method is based on the successive and simultaneous calculations of the motions of many carriers during a small time increment Δt. The method is essentially dynamic and thus is suitable for the analysis of transient carrier motion. A key step to execute the ensemble Monte Carlo calculation is deciding the free flight time, that is the duration between two successive scattering events. This duration depends on the total scattering rate which is the sum of various scattering rates of individual scattering mechanisms. The probability density, $P(\tau)$, of finding an electron traveling for a time τ without being scattered is expected to follow the relation

$$\frac{dP(\tau)}{d\tau} = -\frac{P(\tau)}{\left(\frac{1}{W_T(E_{\mathbf{k}})}\right)}, \tag{2.29}$$

where the total scattering rate

$$W_T(E_{\mathbf{k}}) = \sum_{j=1}^{N} W_j(E_{\mathbf{k}}) \tag{2.30}$$

is the sum of the scattering rates of N different scattering mechanisms. Since the scattering rate of each scattering mechanism is a function of electron energy $E_{\mathbf{k}}$, the total scattering rate is also a function of $E_{\mathbf{k}}$.

The solution of (2.29) is

$$P(\tau) = W_T(E_{\mathbf{k}}) \exp\left[-\int_0^{\tau} W_T(E_{\mathbf{k}})dt\right]. \tag{2.31}$$

To determine the free flight time by $P(\tau)$, we have to evaluate the integral in (2.31). Unfortunately, there is no analytical form for that integral because of the complicated form of general $W_j(E_{\mathbf{k}})$. A simple strategy to get rid of this problem is adding a virtual scattering process, called self-scattering, with the scattering rate $W_0(E_{\mathbf{k}})$ to the original total scattering process, so that the new total scattering rate Γ becomes a constant [3],

$$W_0(E_{\mathbf{k}}) = \Gamma - \sum_{j=1}^{N} W_j(E_{\mathbf{k}}) \quad \text{or} \quad \Gamma = \sum_{j=0}^{N} W_j(E_{\mathbf{k}}). \tag{2.32}$$

The inclusion of the self-scattering makes no change to the $\mathbf{k}$ wave vector of the particle and has an advantage that (2.31) can be recast simply as

$$P(\tau) = \Gamma \exp^{-\Gamma\tau}. \tag{2.33}$$

The free flight time τ for a carrier scattering process is a random variable following the distribution $P(\tau)$. This distribution gives the mean free flight time $\tau_m = \int_0^{\infty} \tau P(\tau)\, d\tau = 1/\Gamma$. To see which value Γ should is taken, let us consider a carrier with Fermi velocity v_F, which has the free flight length $l = v_F\tau$ and the mean free path $l_{\mathrm{mfp}} = \int_0^{\infty} lP(\tau)\, d\tau = v_F/\Gamma$. That is, once v_F and l_{mfp} of a system are known, Γ can be decided. In numerical simulations, τ can be generated by substituting a uniformly distributed random number $x \in [0, 1]$ into the following the formula

$$\tau = -\frac{\ln(x)}{\Gamma}. \tag{2.34}$$

Equivalently, one can calculate its mean free path by

$$l = -l_{\mathrm{mfp}} \ln(x). \tag{2.35}$$

This classical picture is valid, when the sample size is larger than the de Broglie wave length of the carriers.

2.4 Semiclassical Path Integral formalism

With the knowledge of carrier transport and scattering, now we proceed to the evolution of carrier spin. Since the spin dynamics of the semiconductors discussed below is related to the electron dynamics by the spin-orbit coupling, how the spin evolves is decided by the carrier evolution discussed in the last chapter. While the former is stochastic due to impurity collisions, the latter is deterministic and fully decided by the former. In the following, in combination with the ensemble Monte Carlo method, we apply the Semiclassical Path Integral *(SPI)* method to the EY and DP spin relaxation mechanisms in a quasi-2DEG system to reveal the intriguing behaviors of carrier spin evolution.

The original semiclassical path integral method was formulated for Rashba systems [4, 5, 6], which has the Hamiltonian

$$H = H_0 + H_{\mathrm{SOI}}, \tag{2.36}$$

where H_0 consists of the kinetic and potential energies of an electron in the system and H_{SOI} represents its spin orbit interaction *(SOI)*. Since the energy of spin orbital coupling in the interested material is usually much smaller than the kinetic and potential energies, the electron trajectory γ can be determined purely by H_0. The spin dynamics of this electron will be described by an evolution operator in the path integral formalism,

$$U_\gamma = \exp\left[-\frac{i}{\hbar}\int_\gamma H_{\mathrm{SOI}}(t)\, dt\right]. \tag{2.37}$$

If the electron collides with the impurities or boundaries n_γ times at points ξ_1, ξ_2,

$\cdots$, ξ_{n_γ}, its trajectory γ will comprise n_γ straight segments,

$$\gamma = \gamma_{n_\gamma} + \cdots + \gamma_2 + \gamma_1. \tag{2.38}$$

The corresponding spin evolution operator U_γ becomes a product

$$U_\gamma = U_{\gamma_{n_\gamma}} \times \cdots \times U_{\gamma_2} \times U_{\gamma_1} \tag{2.39}$$

of the individual operators $U_{\gamma_j} = \exp\left[-\frac{i}{\hbar} H_{\mathrm{SOI}} t_{\gamma_j}\right]$, where t_{γ_j} is the time the electron spends to travel through the distance γ_j. These operators own a time order property and do not commute with each other. This formalism is originally for Rashba Hamiltonian, but can be easily extended to other systems governed by the DP mechanism, such as the Dresselhaus Hamiltonian, and even to the EY mechanism as we shall show below.

2.5 Spin evolution under EY mechanism

For systems under EY mechanism, the Hamiltonian of the electron can be separated into two parts

$$H = H_0 + H_{\mathrm{int}}. \tag{2.40}$$

The unperturbed part H_0 has the form shown in the expression (1.1). The second term H_{int} can be treated as a perturbed Hamiltonian which contains several interactions responsible for electron scattering. These scattering potentials could arise from impurities, heavy holes, phonons, piezo-acoustic modes, and boundaries.

For EY mechanism, the spin may flip when the carrier is scattered. The crucial task is to determine the spin flip probability in each scattering event. Let us consider a scattering described by H_{int}, which changes the electron momentum from $\mathbf{k}$ to $\mathbf{k}'$. According to Sec. 1.1, if the electron spin does not flip during this scattering, the electron momentum relaxation time τ_p is related to H_{int} by

$$\frac{1}{\tau_p} \propto \left| \int a^*_{k'} H_{\mathrm{int}} a_k e^{i(\mathbf{k}-\mathbf{k}')\cdot\mathbf{r}} d\mathbf{r} \right|^2 . \tag{2.41}$$

If the spin flips during the scattering, the spin relaxation time T_1, often called the longitudinal time or spin-lattice time, is given by

$$\frac{1}{2T_1} \propto \left| \int (a_{-k'} H_{\mathrm{int}} b_k - b_{-k'} H_{\mathrm{int}} a_k) e^{i(\mathbf{k}-\mathbf{k}')\cdot\mathbf{r}} d\mathbf{r} \right|^2 , \tag{2.42}$$

which has around the same proportionality constant as (2.41). When the electron encounters a scattering at event ξ, whether its spin state flips or not will be determined by the stochastic operator [8]

$$U_\xi = \begin{cases} \begin{pmatrix} 0 & 1 \\ 1 & 0 \end{pmatrix} := I_{\text{flip}}, & \text{flip probability } \phi \\ \begin{pmatrix} 1 & 0 \\ 0 & 1 \end{pmatrix} := I_{\text{nonflip}}, & \text{nonflip probability } 1-\phi \end{cases} \tag{2.43}$$

where $0 \le \phi \le 1$. To realize this process in a calculation, one can randomly take a number x between 0 and 1 at a scattering. Then the operator

$$U_\xi = \Theta(\phi - x) I_{\text{flip}} + \Theta(x - \phi) I_{\text{nonflip}} \tag{2.44}$$

will decide stochastically whether the spin will flip, where Θ is the Heaviside function. The flip probability ϕ is related to the flip rate in Eqs. (2.41) and (2.42) by

$$\frac{\frac{1}{\tau_p}}{\frac{1}{2T_1}} = \frac{1-\phi}{\phi} \quad \text{or} \quad \phi = \frac{\tau_p}{2T_1 + \tau_p}. \tag{2.45}$$

That is, ϕ can be calculated from T_1 and τ_p, provided they have been measured from experiments.

In a simulation, if an electron encounters n_γ times of scattering at points ξ_1, ξ_2, $\cdots$, ξ_{n_γ}, the corresponding spin evolution operator U_γ will be

$$U_\gamma = U_{\xi_{n_\gamma}} \times \cdots \times U_{\xi_2} \times U_{\xi_1}. \tag{2.46}$$

Since this formula for the EY mechanism resembles (2.39) for the Rashba systems, one can regard (2.46) as a generalization of (2.39). However, U_γ in (2.46) is assumed to flip the spin only at discrete times when scattering events occur, whereas that in (2.39) changes the spin at any time. With the microscopic information on each individual spin from (2.46), any macroscopic average of a crowd of spins can be calculated. Suppose the quasi-2DEG system is on the **xy** plane. The main quantity of concern is the spin polarization in **z** direction

$$P_z(t) = \frac{1}{n_{(t,D)}} \sum_{\text{electrons at } (t,D)} s_z(t), \tag{2.47}$$

which averages over the **z** component of the spin states $s_z(t)$ of all $n_{(t,D)}$ electrons in an observation window D at time t. When the spin of an electron is polarized to $\mathbf{z}$ direction, s_z is set to 1. Therefore, the maximum value of $|P_z(t)|$ is 1, which corresponds to all electrons being aligned in $\mathbf{z}$ direction.

2.6 Spin evolution under DP mechanism

For systems with Rashba SOI, the Hamiltonian consists of two parts

$$H = H_0 + H_R, \tag{2.48}$$

where H_0 represents the sum of the kinetic and potential energies of an electron with its effective mass in a quasi-2DEG. The second part $H_R = \alpha\,(\boldsymbol{\sigma} \times \mathbf{k}) \cdot \mathbf{z}$ represents the Rashba SOI, where α is the spin orbit coupling constant, $\boldsymbol{\sigma}$ stands for Pauli matrices, $\hbar\mathbf{k}$ denotes the electron momentum, and $\mathbf{z}$ is the unit vector perpendicular to the quasi-2D sample. The Hamiltonian H_R will cause spin precession, when the carrier of the spin moves along a classical trajectory. A characteristic length determining this precession is the spin rotation length $L_{so} = \frac{\hbar^2}{\alpha m^*}$, where m^* is the effective mass of the particle. In real semiconductor materials, the energy ratio H_R/H_0 can be as large as 1/10, such as that in the InSb sample [9]. But even for this ratio, H_R is still small compared with H_0. In such systems, the electron dynamics is not affected strongly by its spin dynamics, so that in the leading approximation classical trajectories are determined by H_0. Thus, we can apply the ensemble Monte Carlo method to determine the trajectory and scattering process for each electron in quasi-2DEG system.

For a free electron moving along a straight trajectory γ of length l, the dynamics of its spin state is governed by the evolution operator U in the path integral formalism [6]

$$U = \exp\left[-\frac{i}{\hbar}\int_\gamma H_R(t)\,dt\right] = \exp\left[-i\frac{l}{L_{so}}\boldsymbol{b}\cdot\boldsymbol{\sigma}\right], \tag{2.49}$$

where $\boldsymbol{b} = \mathbf{z} \times \mathbf{k}/|\mathbf{k}|$. This operator represents simply the spin rotation. If an electron collides with impurities or boundaries n_γ times, its trajectory γ will consist of n_γ straight segments $\gamma = \gamma_{n_\gamma} + \cdots + \gamma_2 + \gamma_1$, The corresponding spin evolution operator U_γ becomes a product

$$U_\gamma = U_{\gamma_{n_\gamma}} \times \cdots \times U_{\gamma_2} \times U_{\gamma_1}, \tag{2.50}$$

where the individual operators

$$\begin{aligned} U_{\gamma_j} &= \exp\left[-i\frac{l_j}{L_{so}}\boldsymbol{b}_j\cdot\boldsymbol{\sigma}\right] \\ &= \mathbf{1}\cos\left(\frac{l_j}{L_{so}}\right)-i(\boldsymbol{b}_j\cdot\boldsymbol{\sigma})\sin\left(\frac{l_j}{L_{so}}\right) \end{aligned} \tag{2.51}$$

along different straight segments do not commute with each other. In analogy to the case in of EY mechanism, the microscopic information on each individual spin from (2.50) allows us to calculate any macroscopic average of a crowd of spins, as discussed in (2.46), in analogy to (2.47).

Bibliography

[1] C. Jacobono and P. Lugli, *The Monte Carlo Method for Semiconductor Device Simulation* (Springer-Verlag Wien New York, 1989).

[2] K. Tomizawa, *Numerical Simulation of Submicron Semiconductor Devices* (Artech House, Boston, London, 1993).

[3] K. Kurosawa, Journal of the Physical Society of Japan **21**, Supplement, 424 (1966).

[4] A. G. Mal'shukov, V. V. Shlyapin and K. A. Chao, Phys. Rev. B **66**, 081311(R) (2002).

[5] C.-H. Chang, A. G. Mal'shukov and K. A. Chao, Phys. Lett. A **326**, 436 (2004).

[6] C.-H. Chang, A. G. Mal'shukov and K. A. Chao, Phys. Rev. B **70**, 245309 (2004).

[7] S. Datta, *Quantum Phenomena* (Addison-Wesley, 1989), 185.

[8] J. Tsai and C.-H. Chang, J. Phys.: Condens. Matter **24**, 075801 (2012).

[9] H. Chen, J. J. Heremans, J. A. Peters, A. O. Govorov, N. Goel, S. J. Chung, and M. B. Santos, Appl. Phys. Lett. **86**, 032113 (2005).

Chapter 3

EY Spin Relaxation in Quantum Wells and Narrow Wires

In the following, we apply the ensemble Monte Carlo method and the semiclassical path integral method to study the spin relaxation of the Elliott-Yafet mechanism in low-dimensional systems. In quantum wells, the spin properties calculated by these methods confirmed the experimental results. In two dimensional narrow wires, size and impurity effects on the Elliott-Yafet relaxation were predicted, including the wire-width-dependent relaxation time, the polarization evolution on the sample boundaries, and the relaxation behavior during the diffusive-ballistic transition. For ballistic narrow wires, we derived an exact relation between the Elliott-Yafet relaxation time and the wire width, which confirmed the above simulations.

3.1 Introduction

Spin relaxation is one of the central issues in the study of spintronics [1, 2, 3]. This phenomenon is ubiquitous in materials with spin polarization and has a long research history dating back to the Elliott-Yafet (EY) relaxation in simple metals (see [3] and recent papers citing this review). The study in this context is largely motivated by a fundamental interest in material properties. However, pursuing efficient spin manipulation in devices might further boost the progress in this field. Today, several types of mechanisms responsible for different spin relaxations have been found [4, 5, 6, 7], and among these, the D'yakonov-Perel' (DP) and EY mechanisms play an essential role. The former is due to spin precession between the momentum scattering events, while the latter happens "during" the momentum scattering events. These mechanisms affect the spin dynamics in various materials. For instance, in zinc-blende semiconductors at low temperatures, the spin relaxation is dominated by the DP mechanism [8, 9, 10, 11, 12, 13]. In InGaAs/InP multiple-quantum wells at room temperature [14, 15] and the Te-doped InSb/$Al_{0.15}In_{0.85}Sb$ at low temperatures [16], the spin lifetime depends mainly on the EY mechanism [17, 18, 19, 20]. In the past, a large number of experimental and theoretical studies have been devoted to the DP mechanism, either in the 3D bulk or in low-dimensional systems like quantum wells (QWs) and 2D narrow wires [13, 21, 22, 23, 24, 25, 26, 27, 28]. However, comparatively less effort has been put into studying the EY relaxation, especially in low-dimensional systems [29].

In this work, we apply the ensemble Monte Carlo method and the semiclassical path integral method to investigate the EY relaxation in QWs and 2D narrow wires in both diffusive and ballistic regimes. The study gave results in accordance with the experimentally measured values in real samples [16]. Based on this consistency, we used these methods to study the impurity and sample size effects on the EY relaxation under broad sample conditions. The main issues were how the relaxation time changed with sample width, how the polarization evolved on the boundary, and how the impurity density variation from diffusive to ballistic regimes affected the EY relaxation. Furthermore, the DP relaxation was calculated under the same sample conditions in order to compare it with the EY results. Finally, an analytical formula was derived for ballistic narrow wires, which confirmed our simulations and revealed exactly how the EY relaxation time varied with the wire width.

This chapter is organized as follows. In Sec. 2, the validity and precision of using the EMC and the SPI methods on the experimental samples are examined and compared with the theoretical results. In Sec. 3 and Sec. 4, the effects of size and impurity, respectively, on the EY relaxation are studied and compared with the DP relaxation. Finally, a summary and discussion are given in Sec. 5, and a supplementary material for spin relaxation process is represented in Sec. 6.

3.2 The EMC and SPI methods on experimental samples

The spin relaxation caused by the EY mechanism has been explored by some experimental groups [14, 15, 16]. In [16], a sample is InSb/$Al_{0.15}In_{0.85}Sb$ single QW grown by MBE on the GaAs substrates. The QW has a well width of 20 nm (corresponding to the height in Figure 3.1) and was uniformly Te-doped (sample number me1831F). The electron density in this sample is 5.7×10^{11} cm^{-2} at 77K

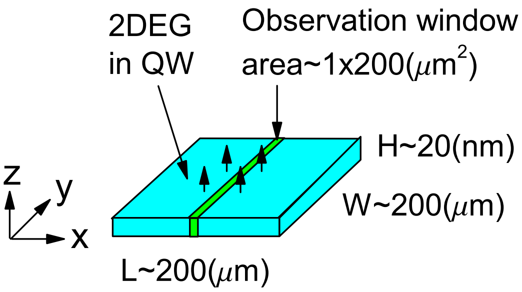

Figure 3.1: A quasi-2D sample and an observation window which is a stripe of area 1×200 μm^2. For a quantum well with large L and W, the stripe is long and the average spin behavior therein is almost the same as that in the whole well (for cases in Figures 3.2 and 3.3). For a narrow wire with large L but small W, the stripe is short and the average spin behavior inside it is a local spin dynamics along the wire (for the case in Figure 3.7).

and 7.3×10^{11} cm^{-2} at 300K. Since the carrier concentration of semiconductor is proportional to T [30], the concentration for other T in between can be linearly interpolated, as $n_e(T) \approx (0.0072T + 5.15) \times 10^{10}$ cm^{-2}. The mobility of this sample was measured by means of the Hall effect and behaves as $\log_{10} \mu(T) \approx 0.28 \times \log_{10} T - 0.55$ m^{2}V^{-1}s^{-1} within $T = 50 \sim 300$K. For more temperature dependent factors in spin relaxations, it is referred to [23].

Figure 3.2 shows the product of the spin relaxation time with the temperature, $\tau_s T$, versus the carrier mobility μ. Its inset depicts the spin relaxation time versus the temperature of the sample. In both plots, the triangles are the experimental data measured from the sample me1831F, which is mainly governed by the EY mechanism. The black dots are calculated from the formula [16]

$$\frac{1}{\tau_s} = C_{\text{EY}} \eta^2 \left(1 - \frac{m^*}{m}\right)^2 \frac{E_{1e}}{E_g^2} kT \frac{1}{\tau_p}. \tag{3.1}$$

Therein, m is the free electron mass, m^* denotes the effective mass in the conduction band, E_g represents the band gap, E_{1e} stands for the confinement energy of the lowest electron subband, τ_s is the EY mechanism induced spin relaxation time which is equal to T_1 in Eq. (1.9), and $\eta = \Delta/(E_g + \Delta)$ with the spin orbit splitting energy Δ. The momentum relaxation time τ_p is related to the mobility μ by $\tau_p = \mu m^*/e$ and the dimensionless constant C_{EY} is believed to be of the order of unity. The black dots in Figure 3.2 are calculated from (3.1) by using the following parameters of me1831F: $\Delta \approx 0.81$ eV, $E_g \approx 0.24$ eV, $m^*/m \approx 0.014$,

Table 3.1: The simulation protocols. T_1 is calculated by (3.1), $\tau_p = \mu m^*/e$, $v_F = (\hbar/m^*)\sqrt{2\pi n_e}$, $l_{\mathrm{mfp}} = v_F \tau_p$, and ϕ is calculated by (2.45).

T(K)	50	70	100	120	150	170	200	250	300
T_1(ps)	2.54900	1.99790	1.54320	1.35230	1.15060	1.05090	0.93424	0.79486	0.69656
τ_p(ps)	0.06619	0.07263	0.08014	0.08428	0.08963	0.09278	0.09703	0.10320	0.10852
v_F(μm/ps)	1.5381	1.5580	1.5874	1.6067	1.6353	1.6540	1.6817	1.7270	1.7710
l_{mfp}(μm)	0.10180	0.11316	0.12722	0.13541	0.14656	0.15345	0.16318	0.17821	0.19219
ϕ	0.01282	0.01785	0.02531	0.03022	0.03749	0.04228	0.04937	0.06096	0.07227

$E_{1e} \approx 0.08$ eV and $C_{\mathrm{EY}} \approx 7.5$ [16]. Recall that τ_s can be affected by various scattering potentials mentioned in Sec. 1.2. Among others, phonons will become more significant at high T.

Figure 3.2 shows that both the experimental and theoretical studies give the relation $\tau_s T \propto \mu$ for most μ. But two experimental points have an opposite trend $\tau_s T \propto \mu^{-1}$ at high μ, which corresponds to the high T regime in the sample me1831F, as known from the empirical $\mu(T)$ relation mentioned at the beginning of this section. One believes that this opposite trend is because the DP mechanism overrides the EY mechanism in the high μ regime, according to the current understanding that $\tau_s T \propto \mu$ for EY mechanism and $\tau_s T \propto \mu^{-1}$ for DP mechanism [16]. The latter is supported by the observation on the sample me1833 (remotely n-doped with Te 20 nm above the well) in [16], which follows the DP mechanism and has the property $\tau_s T \propto \mu^{-1}$.

Next, the relaxation properties will be calculated by the ensemble Monte Carlo method and the semiclassical path integral method. To compare with above experimental results, the simulations needs to insert the following experimental parameters. First, the spin flip probability ϕ will be calculated by (2.45), where how $\tau_p = \mu m^*/e$ and T_1 vary with T is based on the above empirical relation $\mu(T)$ and the black dots in the inset of Figure 3.2, which are calculated from (3.1). Second, v_F can be derived from $v_F = \hbar/m^* \sqrt{2\pi n_e}$ with the above empirical electron density $n_e(T)$. Notice that since n_e lies between 5.5×10^{11} and 7.3×10^{11} cm^{-2}, the corresponding de Broglie wavelength $\lambda_F = \sqrt{2\pi/n_e}$ ranging from 34 to 30 nm is larger than the sample hight 20 nm, as shown in Figure 1. Thus, the electrons are confined in the $\mathbf{z}$ direction of the sample. Third, the size of the experimental sample was not explicitly mentioned in [16]. However, (3.1) therein is referred to [14, 15], where the sample sizes are about 2 inches (approximately 5×10^4 μm) in length. Our simulation is performed on a smaller square of 2×10^2 μm in length for less computational consumption. Both the experimental and simulation samples belong to bulk systems. Since their scales are much larger than the de Broglie wavelength λ_F ($30 \sim 34$ nm), the electron motion on the **xy** plan is more particle-like and the validity of ensemble Monte Carlo method and the semiclassical path integral method are justified. We put 4×10^6 electrons into our 2D sample, which are initially in the standard initial condition and follow the simulation protocols at $50 \sim 300$K in Table 1. The time course of the polarization $P_z(t)$ is recorded in the middle of the sample (Figure 3.1).

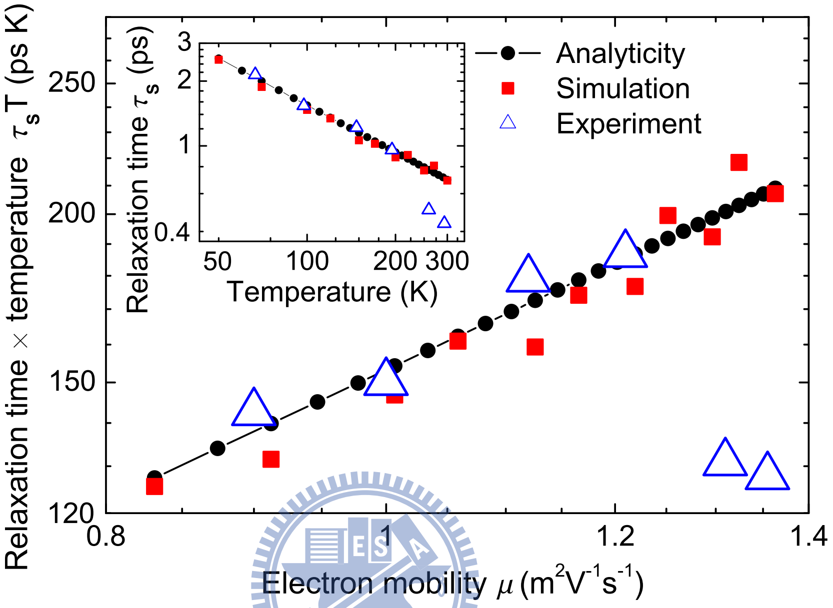

Figure 3.2: A comparison between the analytical, numerical and experimental relations between $\tau_s T$ and mobility μ, as well as between τ_s and temperature T (inset). The large triangle size indicates the experimental error bar.

The observed $P_z(t)$ is an exponential function with a relaxation time τ_s. During the temperature variation in Table 3.1, the relations $(\tau_s T, \mu)$ and (τ_s, T) can be calculated, which are plotted as red squares in the main plot and the inset of Figure 3.2, respectively. Note that our recent theoretical study and simulation reveal that the $P_z(t)$ of the DP relaxation in a narrow wire will transit from an exponential function to a Bessel function during the impurity density decline [27]. Such $P_z(t)$ deviation from an exponential function will not occur in the EY mechanism, as we shall prove in Sec. 4. Thus, here we can characterize $P_z(t)$ properly by the parameter τ_s without worrying its deformation.

The red squares in Figure 3.2 calculated by our methods show very close values to the theoretical and experimental results for most μ, with the same relation $\tau_s T \propto \mu$. The opposite experimental trend $\tau_s T \propto \mu^{-1}$ in the high μ regime is not to see in our simulation. It indirectly supports the previous hypothesis that $\tau_s T \propto \mu^{-1}$ arises from other mechanisms, because the pure EY mechanism in our ensemble Monte Carlo method and the semiclassical path integral method simulation cannot produce this trend. The main plot of Figure 3.2 does not explicitly tell us how τ_s varies with T. In fact, T can influence the sample me1831F through two ways. First, a large T will increase the electron mobility μ and subsequently $\tau_p = \mu m^*/e$, which in turn will reduce the electron scattering pro unit traveling distance. However, a large T also will enhance the spin flip probability ϕ (see Table 3.1) and make spin flip more frequently. When two effects blend together, it is hard to predict how τ_s will change with T. Nevertheless, an obvious τ_s decay is readily seen, when we transform the $(\tau_s T, \mu)$ data into the (τ_s, T) plot in the inset.

3.3 The size effect on the EY relaxation

The size effect on the spin relaxation is another interesting issue in spintronics. For instance, the group of Awschalom has carried out some measurements on the DP relaxation in narrow wires of different widths [26]. However, to the best of our knowledge, very few experiments have investigated the size effect on the EY relaxation. A study close to this topic was the EY relaxation in the granular systems [29], but the sample size there was fixed. In this section, we will study how the EY spin relaxation changes with the width of a wire. Our sample has 200 μm in length, while its width varies between 0.1 μm (narrow wire) and 200 μm (2D quantum well). We take 8×10^5 electrons in the standard initial condition and use the parameter values from Table 3.1 for simulations as before.

Figure 3.3 depicts the relaxation time τ_s versus the sample width W at various temperatures T. Three conclusions can be drawn from this plot:

(1) τ_s decreases with T.

(2) τ_s is nearly a constant for $W > 1$ μm at all T.

(3) τ_s drops abruptly to zero, when $W < 1$ μm.

Phenomenon (1) has the same reasoning as that at the end of Sec. 3.2. To account for phenomena (2) and (3), remember that for $W > 1$ μm the sample is like a bulk system. The electron spin in this system are flipped mainly by the impurities in the bulk and less by the sample boundaries. Therefore, the relaxation time τ_s is almost fully determined by the impurity density and is thus a constant of W. However, for $W < 1$ μm, the boundary induced spin flip becomes more significant. The smaller the sample width, the higher the collision frequency will

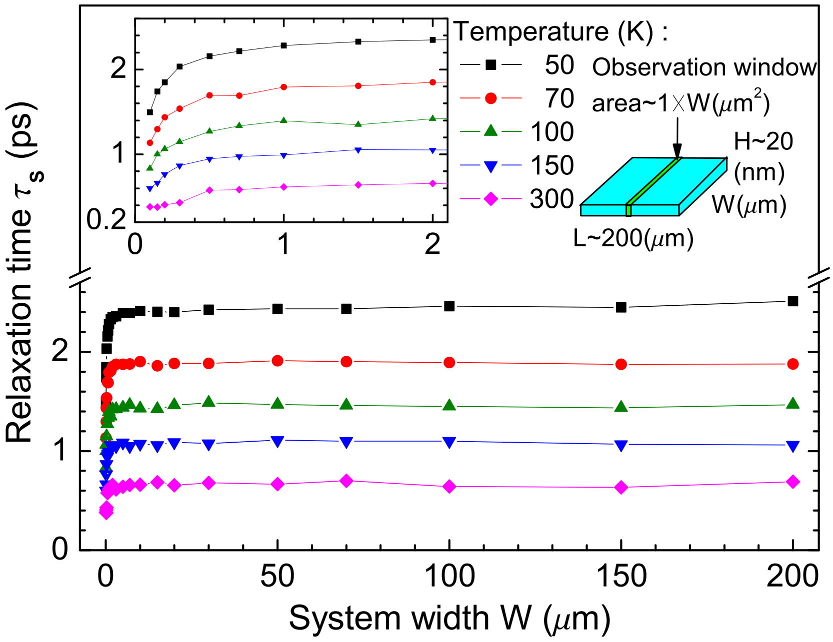

Figure 3.3: The EY spin relaxation time versus the wire width at five different temperatures, observed on a stripe of area $1 \times W$ μm^2. The inset is magnified from the main plot.

be, and the faster the spin will flip. When W approaches zero, τ_s tends to zero, because almost all electrons collide with the boundaries infinitely often, except the minority electrons moving exactly along the wire axis.

It is well known that the DP relaxation near the sample boundary behaves differently from that far from the boundary [27, 31, 32]. An interesting question is whether the EY relaxation will behave similarly on the boundary. To answer this question, we shrink the observation window to a small square of area 1×1 μm^2 and use this window to scan the local τ_s at different places along the width direction of a wire. Figure 3.4 depicts the EY relaxation time τ_s, which remains close to a constant inside the sample, up to the drops near two boundaries. How close to the boundaries τ_s will begin to drop is an open question requiring further study. Moreover, the inset of Figure 3.4 shows that $P_z(t)$ is almost flat up to the slight drops on the boundaries. These drops will become apparent, if we magnify the individual $P_z(t)$ curves.

For a comparison, we calculate the τ_s of the DP relaxations along a wire of width $6 \sim 50$ μm, as shown in Figure 3.5. The initial electron and spin states in the simulation are the same as above EY cases, while its temperature is as low as 5K to mimic the real experimental environment. The corresponding Fermi velocity and mean free path are $v_F = 0.37$ μm/ps and $l_{\mathrm{mfp}} = 0.28$ μm and its spin

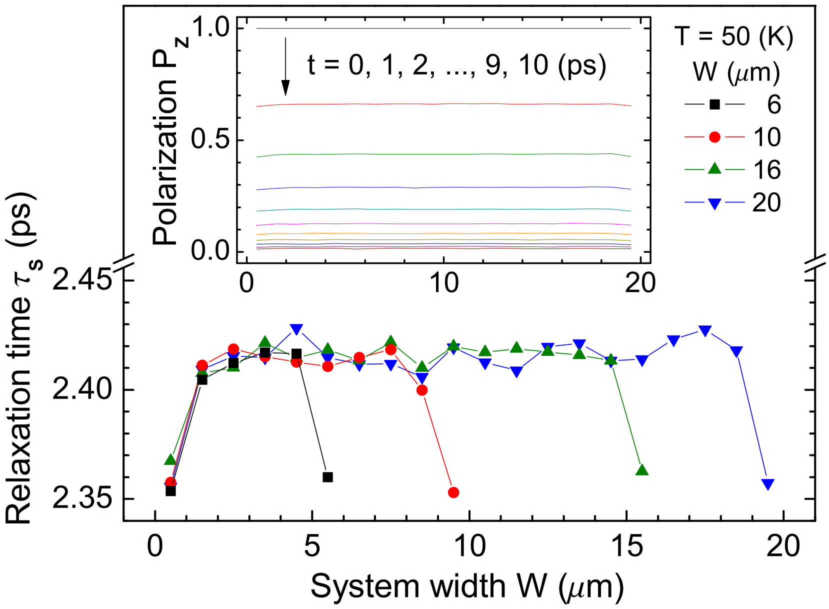

Figure 3.4: The EY spin relaxation time versus four wire widths at 50K, observed on a square of area 1×1 μm^2 scanning along the wire width in the middle of the sample. The inset is the evolution of spin polarization along the width $W = 20$ μm.

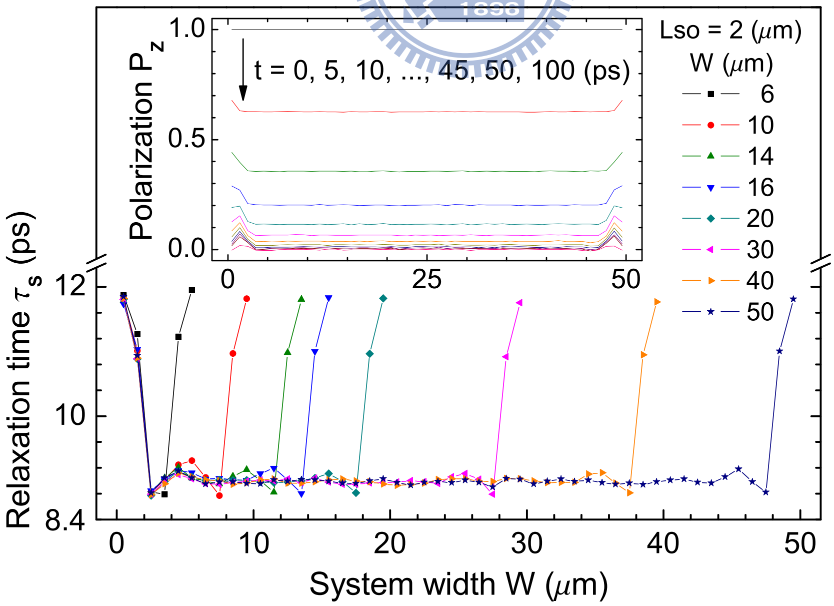

Figure 3.5: The DP spin relaxation time versus eight wire widths at $T = 5$K and $L_{so} = 2$ μm, observed on a square of area 1×1 μm^2 scanning along the wire width in the middle of the simulation sample. The inset is the evolution of spin polarization along the width $W = 50$ μm.

rotation length (as defined in [24,25,27]) is $L_{so} = 2\ \mu$m. The simulation method is referred to [27]. In contrast to the EY relaxation, the DP relaxation time near the boundary is larger than that elsewhere (Figure 3.5). Moreover, the $P_z(t)$ of the DP relaxation on the boundary exhibits a hump structure (inset of Figure 3.5), which is opposite to the EY relaxation and is a main difference between these two relaxations. The τ_s increase on the boundary in the DP relaxation is ascribed to the reversal rotation of spins [27,32], whereas the τ_s decrease on the boundary in the EY relaxation is due to more frequent boundary collisions.

3.4 The impurity effect on the EY relaxation

When the mean free path of the electrons exceeds the wire width, the system will enter the ballistic regime. The $P_z(t)$ of the DP relaxation undergoes a drastic change from an exponential function to a Bessel function during the diffusive-ballistic transition [27]. In this section, we will examine how the $P_z(t)$ of the EY relaxation behaves in the ballistic regime.

Suppose an ensemble of electrons in the standard initial condition are put in a narrow wire as in Figure 3.6. The spin polarization $P_z(t)$ observed at the origin p_0 at time t is averaged from the spin states of all electrons which arrive at p_0 at time t. These electrons can arrive through a straight trajectory or various zigzag ones, like $\overline{p_1 p_0}$ and $\widetilde{p_2 p_0}$ in Figure 3.6, all of which have the same length $l = v_F t$. Depending on the trajectory types, these electrons will launch at different x at time 0. Suppose $\tilde{s}_z(x)$ is the $\mathbf{z}$ component of the spin state of an electron at p_0 at time t when it starts at x at time 0. Then $P_z(t)$ is an average over all these spin states [27],

$$P_z(t) = \frac{\int_{-l}^{l} \tilde{s}_z(x) \rho w(x) W dx}{\int_{-l}^{l} \rho w(x) W dx}, \tag{3.2}$$

where $w(x)$ is a weight proportional to the number of electrons starting at x and contributing to $\tilde{s}_z(x)$ and ρ denotes the constant surface density of the electrons in the wire. Notice that since the spin flip in the EY mechanism is a stochastic process, two electrons, even when running along the same trajectory, may have different final spin states. Thus, the spin state $\tilde{s}_z(x)$ should be understood as an ensemble average taken from all electrons running along the same trajectory. The fluctuation around this average is extremely small for real materials having the typical electron density 10^{11} cm^{-2}. If an electron starting between x and $x+\varepsilon$ (for the case $x \geq 0$) has to arrive at p_0 at time t, its initial outgoing angle must lie between $\theta(x)$ and $\theta(x+\varepsilon)$, with $\varepsilon \ll 1$ (see the example for $x=\xi$ in Figure 3.6). Thus, the weight $w(x)$ becomes the fraction of the electrons at x running within these two angles over those within the whole 2π angle. If the electrons are uniformly distributed in the wire with isotropic outgoing angles, the fraction of electron number equals the fraction of orientation range [27],

$$\begin{aligned} w(x) &= \frac{1}{2\pi}\cdot 2\cdot[\theta(x)-\theta(x+\varepsilon)] \\ &= \frac{1}{\pi}\left[\arccos\left(\frac{x}{l}\right)-\arccos\left(\frac{x+\varepsilon}{l}\right)\right], \end{aligned} \tag{3.3}$$

where the factor 2 arises from the two mirror-symmetric orientations ±θ.

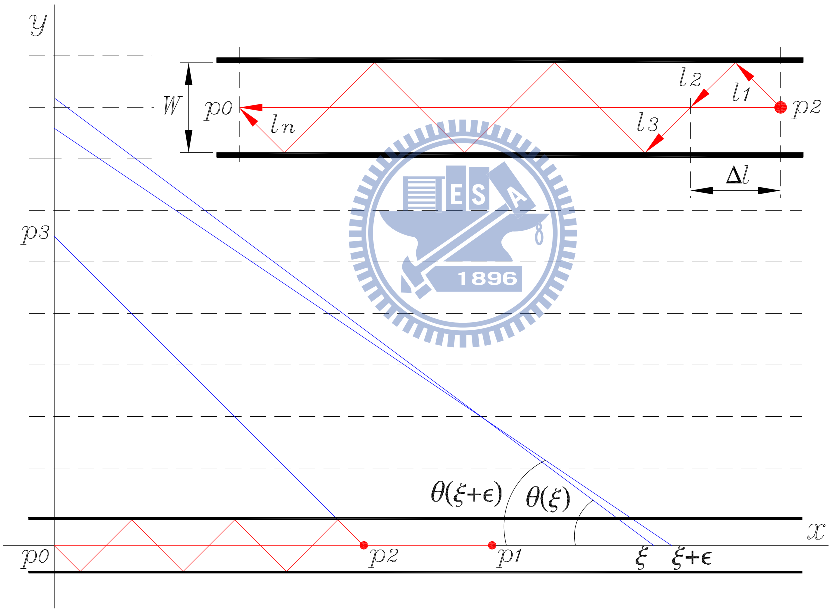

Figure 3.6: In a ballistic narrow wire, a straight trajectory $\overline{p_1p_0}$ and a zigzag trajectory $\widetilde{p_2p_0}$ have the same length $l=v_Ft$. The length of $\widetilde{p_2p_0}$ is equal to that of $\overline{p_2p_3}$, since the former can be regarded as a multiple mirror reflection of the latter with respect to the horizontal dashed lines. The values $\theta(\xi)$ and $\theta(\xi+\epsilon)$ are the outgoing angles of the electrons at ξ and $\xi+\epsilon$, respectively, along which the electrons can reach p_0 after running through the same distance l. The inset is a magnification of $\widetilde{p_2p_0}$.

While the fraction $w(x)$ for EY relaxation is similar to that for DP relaxation, $\tilde{s}_z(x)$ is completely different for both. To obtain $\tilde{s}_z(x)$ of the EY mechanism, we need to know how many scatterings an electron running from x to p_0 will encounter and how its spin state will be changed by these scatterings. If an electron is initially polarized in **z** direction and encounters n times of scattering, its **z** component of the spin state will on average change to the value (see (3.9) in Supplement)

$$\bar{s}_z(n) = \exp\left(-\frac{n}{\tau}\right), \quad \text{with } \tau = \frac{1-\phi}{2\phi}, \tag{3.4}$$

where ϕ is the spin flip probability in (2.45). Note that $s_z(t)$, $\tilde{s}_z(x)$, and $\bar{s}_z(n)$ in Eqs. (2.47), (3.2), and (3.4) describe the spin state as a function of t, x, and n, respectively. If an electron at p_2 in Figure 3.6 has the outgoing angle $\theta(p_2)$ and travels a distance $l = v_F t$ along a zigzag trajectory to arrive at p_0 at time t, it will collide with the two boundaries n times with

$$n \approx \frac{x}{\Delta l} = \frac{x}{W \cdot \cot\theta(p_2)} = \frac{\sqrt{l^2 - x^2}}{W}, \tag{3.5}$$

where Δl is the distance between two collisions projected on the x axis (inset of Figure 3.6). Inserting (3.5) into (3.4), $\bar{s}_z(n)$ becomes a function of x,

$$\tilde{s}_z(x) = \exp\left[-\left(\frac{\sqrt{l^2 - x^2}}{W}\right) \cdot \frac{1}{\tau}\right]. \tag{3.6}$$

Inserting (3.3) and (3.6) into (3.2), the evolution of $P_z(t)$ at the observation point p_0 will become completely known. Though this formula is too complicated to have a closed form, its value can be evaluated numerically.

To test the accuracy of (3.2), let us consider three wires of width $W = 0.01$, 0.02, and 0.04 μm with the parameter values of 50K in Table 3.1 and record $P_z(t)$ in the middle of the wire. In the main plot of Figure 3.7, the black squares, red circles, and blue triangles come from simulations, while the black dotted, red dotted-dashed, and blue dashed curves are calculated by (3.2). Both data agree very well with each other. They behave like exponential functions with the relaxation times plotted in the inset of Figure 3.7. In this simulation, we narrowed W down to 10 nm. This value is smaller than the height $H = 20$ nm of the experimental sample and has reached the quantum regime in the width direction, since the Fermi wavelength at 50 K is about 30 nm for semiconductors. Taking this extreme W in the simulation is to verify whether (3.2) was mathematically correctly derived. The readers should not be puzzled with the physical validity of the semiclassical approach. For samples with $W = 0.2$ μm, this formula still predicts a rather close value to the simulated relaxation time (see inset in Figure 3.7).

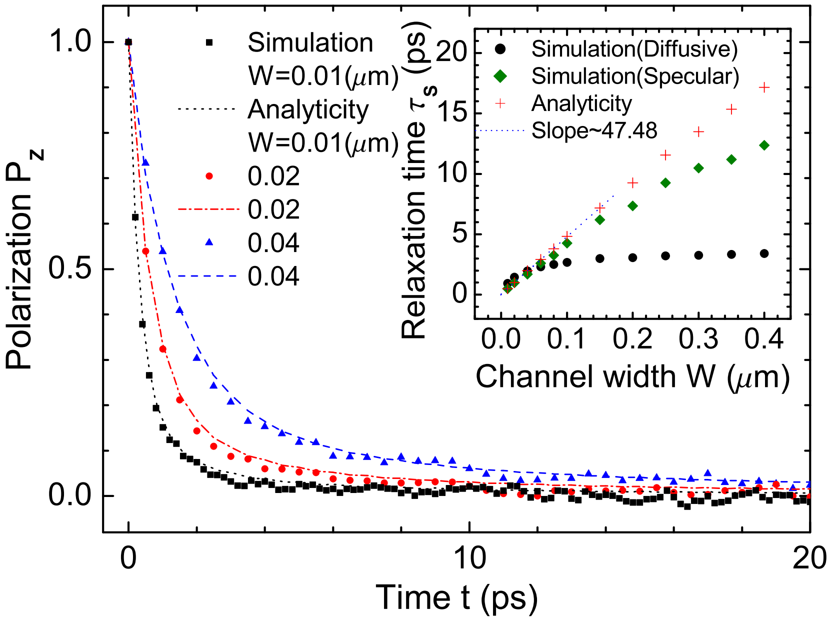

Figure 3.7: The polarization $P_z(t)$ versus the time t in three wires of different widths. The square, circle, and triangle symbols denotes the simulation data and different lines are calculated by the formula (3.2). The inset shows the spin relaxation time versus the wire width from simulations (green rhombus) and analytical approach (3.2) (red cross), fitted by a straight line (blue dotted). All these are results of (3.2) for specular boundary reflections. For diffusive reflections, the (τ_s, W) relation is plotted by the black circles in the inset.

Figure 3.7 also indicates that in a ballistic wire the DP and EY relaxation times vary rather differently with the wire width W. When $W \to 0$, the $P_z(t)$ of the DP relaxation will converge to a Bessel function [27], but that of the EY relaxation (main plot of Figure 3.7) remains as an exponential function, whose relaxation time decreases with the vanishing W. That is, at $W \approx 0$, the DP relaxation is insensitive to W, but the EY relaxation is sensitive to W. The reason is that in the limit $W \to 0$, most electrons are confined in the width direction and collide with the boundaries at very high frequencies. The spins of these electrons tend to be frozen (in width direction) in the DP mechanism, due to the motional narrowing effect [31], but will be accelerated to flip in the EY mechanism, due to the increasing collision frequency. It leads to the drastic distinction between the $P_z(t)$ of DP and EY mechanisms in the ballistic narrow wires.

In the inset of Figure 3.7, the τ_s obtained from (3.2) begin to deviate from that of EMC and SPI methods simulation at $W \approx 0.1$ μm. This W is five times larger than the sample height in [16]. Beyond this W, higher order corrections in Eqs. (3.3) and (3.6) are required to improve the accuracy of (3.2). For $W \to 0$, both simulation and exact formula give the same ratio $\tau_s/W \approx 47.48$. To account for this value, notice that the denominator of (3.2) is independent of l and t. The function $\tilde{s}_z(x)$ in the numerator varies slowly for most $x \in [-l, l]$, but increases sharply with $|x|$ in the two small regions $[-l, -l+\varepsilon']$ and $[l-\varepsilon', l]$, with the limit $\tilde{s}_z(\pm l) = 1$. In contrast, $w(x)$ increases comparatively moderately within $[-l, l]$, with the limit $w(l-\varepsilon') = \arccos(1-\varepsilon'/l)/\pi \approx (\sqrt{2\varepsilon'/l})/\pi$. Thus, $w(x)$ can be approximately regarded as a constant C and taken out of the the integral in the numerator of (3.2). Dropping all l-independent terms, one obtains the proportional relation

$$P_z(t) \propto C \int_{-l}^{l} \tilde{s}_z(x)dx \propto \int_{l-\varepsilon'}^{l} \tilde{s}_z(x)dx \approx \tilde{s}_z(x)\varepsilon'|_{x\approx l} \, . \tag{3.7}$$

Using a Taylor expansion in (3.6), it yields a rough estimation

$$\begin{aligned} P_z(t) &\propto \exp\left[-\frac{l}{\tau W}\left(1-\frac{1}{2}\left(\frac{x}{l}\right)^2 - ...\right)\right]_{x\approx l} \\ &\approx \exp\left(\frac{-v_F t}{2\tau W}\right) = \exp\left(\frac{-t}{\tau'}\right), \end{aligned} \tag{3.8}$$

where $\tau' = 2\tau W/v_F$, which, together with (3.4), gives the ratio $\tau'/W = (\frac{1}{\phi} - 1)/v_F \approx 50.08$. This ratio has been very close to 47.48 obtained from the simulation (inset of Figure 3.7), even though we only consider a small part of the integral around $x \approx \pm l$ in Eq. (3.2). Physically, it highlights the essential contribution of the electrons starting at $x \approx \pm l$. These electrons run almost along the wire axis and are nearly free from collisions with the boundaries. They have no spin flip within time t and will give the main contribution to the non-zero value of $P_z(t)$ at t.

The $P_z(t)$ discussed above comes from the expression (3.2), which is based on the assumption of specular reflections on the boundary. For diffusive reflections, a large number of new trajectories will contribute to $P_z(t)$, in additional to the old ones in (3.2). Along the channel direction, an old trajectory can only have unidirectional movement, while a new trajectory usually contains both forward and backward motions, similar to the trajectories of a random walker. Given an initial point p_2, a final point p_0, and a fixed time t, there exists only one old trajectory (Figure 3.6); however, a bunch of new trajectories are allowed under the same conditions. The shorter the distance $\overline{p_2 p_0}$, the more the allowed new trajectories can be found, just like a random walker has more possible routes to reach a point closer to its initial position. Since the trajectories of shorter $\overline{p_2p_0}$ have more boundary collisions under a fixed t, $P_z(t)$ for diffusive reflections contains on average more trajectories of high reflection frequencies than $P_z(t)$ for specular reflections. Thus, intuitively one would expect a faster polarization relaxation for diffusive reflections, which is indeed true, as confirmed by the simulations depicted by the black circles in the inset of Figure 3.7.

3.5 Conclusion

In this chapter, we apply the ensemble Monte Carlo method and the semiclassical path integral method to the systems governed by the EY relaxation mechanism. The spin relaxation times calculated by these methods are in accordance with the values measured in experiments (Figure 3.2). For the size effect, the EY relaxation time τ_s remains nearly constant for large wire width, but drops abruptly to zero if W shrinks to certain extent (Figure 3.3). This trend is robust against various temperatures, electron mobilities, and electron densities. Near the geometry boundaries, the local τ_s falls rapidly (Figure 3.4), because the boundaries enhance the scattering frequency and the spin relaxation speed, in contrast to that in the DP relaxation. The τ_s and relaxation patterns of both EY and DP mechanisms were calculated and compared (Figure 3.4 and Figure 3.5). For ballistic narrow wires, we derived an analytical formula (3.2) for the EY spin relaxation, which confirms the above simulated $P_z(t)$ (Figure 3.7). This formula explicitly relates the EY spin relaxation time τ_s to the wire width. The predicted τ_s is in a good agreement with the simulated value (inset of Figure 3.7).

The above results were calculated based on two assumptions. First, all electrons contributing to the polarization were on the Fermi surface. In reality, the electron velocity may deviate from this unique value. However, our tests on various velocity distributions showed that the spin relaxation behaviors, especially the relation $\tau_s T \propto \mu$, were less sensitive to this factor. Thus, we presented the simplest distribution concentrated at the Fermi velocity. Second, the scattering rates on the boundary and impurities were assumed to be the same. It was owing to the lack of microscopic details on each individual scattering. Despite that this assumption may not be true for general materials, it does not bother our comparison with the experimental results on the quantum wells, because these wells are so large that the details of boundary scattering is insignificant. For ballistic narrow wires, the boundary scattering becomes important and the results presented here was only a special example. Once the boundary reflection property for other systems is known, the extension of the spin relaxation study to these systems is straightforward.

3.6 Supplement: spin relaxation process

As discussed in the text before Eq. (3.3), the spin state in the EY mechanism should be understood as an ensemble average, since the spin flip in this mechanism is a stochastic process. Let $S_\uparrow(n)$ and $S_\downarrow(n)$ be the probabilities of a spin being at up and down states, respectively, after its electron encounters n times of scattering. Clearly,

$$S_\uparrow(n) + S_\downarrow(n) = 1. \tag{3.9}$$

Under the EY mechanism, we have

$$\begin{aligned} S_\uparrow(n+1) &= (1-\phi)\cdot S_\uparrow(n) + \phi \cdot S_\downarrow(n) \\ &= S_\uparrow(n)\cdot(1-2\phi) + \phi, \end{aligned} \tag{3.10}$$

with the spin flip probability ϕ for each scattering, where (3.9) has been used. After n and $n+1$ times of scattering, the average spin states in $\mathbf{z}$ component are respectively

$$\begin{aligned} \bar{s}_z(n) &= S_\uparrow(n) - S_\downarrow(n) = 2S_\uparrow(n) - 1 \\ \bar{s}_z(n+1) &= 2S_\uparrow(n+1) - 1. \end{aligned} \tag{3.11}$$

Thus, it yields the relation

$$\frac{\Delta \bar{s}_z(n)}{\Delta n} = \frac{\bar{s}_z(n+1) - \bar{s}_z(n)}{(n+1) - n} = -\frac{1}{\tau}\frac{\bar{s}_z(n+1) + \bar{s}_z(n)}{2}, \tag{3.12}$$

with $\tau = (1-\phi)/(2\phi)$. In the continuous limit, it yields

$$\frac{d\bar{s}_z}{dn} = -\frac{1}{\tau}\bar{s}_z. \tag{3.13}$$

According to this equation, if an electron is initially polarized in $\mathbf{z}$ direction, i.e., $\bar{s}_z(0) = 1$, the $\mathbf{z}$ component of this spin will evolve to

$$\bar{s}_z(n) = \exp\left(-\frac{n}{\tau}\right), \tag{3.14}$$

after n times of scattering.

Alternatively, (3.14) can be obtained through a different way. Suppose we have an ensemble of electrons initially under standard conditions in a diffusive bulk sample, with the momentum relaxation time τ_p. If the average $\mathbf{z}$ component of the spin state, $s_z(t)$, undergoes a longitudinal spin relaxation, it will decay exponentially, with the same relaxation time T_1 as that in (2.45),

$$s_z(t) = \exp\left(-\frac{t}{T_1}\right) \approx \exp\left(-\frac{n}{\tau^*}\right), \tag{3.15}$$

where $\tau^* = (1-\phi)/(2\phi)$, because $t \approx n\tau_p$ for n collisions within time t and $\tau_p/T_1 = (2\phi)/(1-\phi)$ according to (2.45). A comparison shows that τ in (3.14) and τ^* in (3.15) are exactly the same.

Bibliography

[1] S. Datta and B. Das, Appl. Phys. Lett. **56**, 665 (1990).

[2] S. A. Wolf, D. D. Awschalom, R. A. Buhrman, J. M. Daughton, S. von Molnár, M. L. Roukes, A. Y. Chtchelkanova and D. M. Treger, Science **294**, 1488 (2001).

[3] I. Žutić, J. Fabian and S. Das sarma, Rev. Mod. Phys. **76**, 323 (2004).

[4] E. L. Ivchenko and G. E. Pikus, *Superlattices and Other Heterostructures: Symmetry and Optical Phenomena* (Berlin: Springer, 1997).

[5] P. H. Song and K. W. Kim, Phys. Rev. B **66**, 035207 (2002).

[6] R. Winkler, *Spin-Orbit Coupling Effects in Two-Dimensional Electron and Hole System* (Berlin: Springer, 2003).

[7] J. Fabian and S. Das Sarma, J. Vac. Sci. Technol. B **17**, 1708 (1999).

[8] G. Dresselhause, Phys. Rev. **100**, 580 (1955).

[9] M. I. D'yakonov and V. I. Perel', Sov. Phys. JETP **33**, 1053 (1971).

[10] M. I. D'yakonov and V. I. Perel', Sov. Phys. Solid State **13**, 3023 (1972).

[11] Y. A. Bychkov and E. I. Rashba, J. Phys. C **17**, 6039 (1984).

[12] M. I. D'yakonov and V. Yu. Kachorovskii, Sov. Phys. Semicond. **20**(1), 110 (1986).

[13] J. Nitta, T. Akazaki, H. Takayanagi and T. Enoki, Phys. Rev. Lett. **78**, 1335 (1997).

[14] A. Tackeuchi, T. Kuroda, S. Muto, Y. Nishikawa and O. Wada, Jpn. J. Appl. Phys. **38**, 4680 (1999).

[15] A. Tackeuchi, T. Kuroda, S. Muto and O. Wada, Physica B **272**, 318 (1999).

[16] K. L. Litvinenko, B. N. Murdin, J. Allam, C. R. Pidgeon, M. Bird, K. Morris, W. Branford, S. K. Clowes, L. F. Cohen, T. Ashley and L. Buckle, New J. Phys. **8**, 49 (2006).

[17] R. J. Elliott, Phys. Rev. **96**, 266 (1954).

[18] W. Zawadzki and W. Szymańska, Phys. Status Solidi (b) **45**, 415 (1971).

[19] G. Fishman and G. Lampel, Phys. Rev. B **16**, 820 (1977).

[20] F. Beuneu and P. Monod, Phys. Rev. B **18**, 2422 (1978).

[21] A. A. Kiselev and K. W. Kim, Phys. Rev. B **61**, 13115 (2000).

[22] A. G. Mal'shukov, V. V. Shlyapin and K. A. Chao, Phys. Rev. B **66**, 081311(R) (2002).

[23] J. Kainz, U. Rössler and R. Winkler, Phys. Rev. B **70**, 195322 (2004).

[24] C.-H. Chang, A. G. Mal'shukov and K. A. Chao, Phys. Lett. A **326**, 436 (2004).

[25] C.-H. Chang, A. G. Mal'shukov and K. A. Chao, Phys. Rev. B **70**, 245309 (2004).

[26] A. W. Holleitner, V. Sih, R. C. Myers, A. C. Gossard and D. D. Awschalom, Phys. Rev. Lett. **97**, 036805 (2006).

[27] C.-H. Chang, J. Tsai, H.-F. Lo anf A. G. Mal'shukov, Phys. Rev. B **79**, 125310 (2009).

[28] S. M. Frolov, S. Lüscher, W. Yu, Y. Ren, J. A. Folk and W. Wegscheider, Nature (London) **458**, 868 (2009).

[29] A. Anaya, M. Bowman and D. Davidović, Phys. Rev. Lett. **93**, 246604 (2004).

[30] R. F. Pierret, *Advanced Semiconductor Fundamentals* (Prentice Hall, 2003), 116.

[31] M. A. Brand, A. Malinowski, O. Z. Karimov, P. A. Marsden, R. T. Harley, A. J. Shields, D. Sanvitto, D. A. Ritchie and M. Y. Simmons, Phys. Rev. Lett. **89**, 236601 (2002).

[32] Y. V. Pershin, Physica E **27**, 77 (2005).

Chapter 4

DP Spin Relaxation in Narrow Wires

In this chapter we apply the ensemble Monte Carlo method and the semiclassical path integral method to study spin relaxations in a narrow 2D strip with the Rashba spin-orbit interaction. Our numerical calculations show a good agreement with the experimental data. We also calculated the relaxation of a uniform spin-density distribution in the ballistic regime of very narrow wires. With the decreasing wire width, the spin polarization exhibits a transition from the exponential decay to the oscillatory Bessel-like relaxation. The *EMC* and *SPI* methods have also been employed to calculate the relaxation of the particularly long-lived helix mode. A good agreement has been found with calculations based on the diffusion theory.

4.1 Introduction

The spin relaxation rate is an important spin transport parameter. Recent calculations and measurements of this parameter in semiconductor systems have to a great extent been motivated by numerous ideas of spintronic applications [1]. In view of these applications, as well as from the fundamental point of view, one of the most interesting problem is the spin relaxation in quantum dots (QD) and quantum wires (QW). In zincblende semiconductors at low temperatures the spin lifetime is mainly determined by the D'yakonov-Perel' (DP) [2] mechanism associated with spin orbit effects. In systems with restricted dimensions this relaxation mechanism is strongly suppressed, as has been calculated in the case of QD [3] and QW [4, 5, 6]. The physics of such a suppression in QW became clear from the analytical solution of the diffusion equation for nonuniform spin distributions confined in a wire [4]. Surprisingly the suppression starts when the width w of a wire becomes less than the characteristic length L_{so} of the spin orbit interaction. In typical zincblende semiconductor systems it varies from several thousands Å up to several microns and can be much larger than the electron mean free path l. Hence, such a spin lifetime enhancement can not be considered as a manifestation of the motional narrowing effect when a restricted geometry of the system imposes the upper limit on the mean free path. Indeed, recent measurements [7] have demonstrated that the spin lifetime τ_s starts to increase already at $w \gtrsim 10\,l$. On the other hand, the observed slowdown of the spin relaxation appears to be not so strong, as expected from the theory. To understand such a behavior, one has to take into account that in experiments [7] the measured parameter is the relaxation time of a particular spatial spin distribution, rather than of an individual electron spin. At the same time, as shown in Ref. [4] only two kinds of spin distributions have very long lifetimes in narrow 2D wires. The first one corresponds to a polarization which is homogeneous along the wire with spins oriented in the plane of a 2D electron gas (2DEG) and perpendicular to the wire axis. The second distribution is a nonuniform helix mode with the wavelength determined by L_{so}. As it will be pointed out below, none of these distributions have been excited by an incident light beam in the experiment [7].

In order to interpret experimental data we will analyze relaxation of various spin distributions. We will study diffusive, as well as ballistic regimes of electron motion in the wire. The EMC and SPI methods previously applied to QD [3] will be employed to calculate the spin relaxation in a wide parameter range, including the ballistic regime $w \lesssim l$, and at time intervals less than the electron momentum relaxation time. To apply the EMC and SPI methods numerically, a large number of electrons are initially randomly distributed in the channel with uniform or helix spin configurations as explained below. In the following, we assume that the channels have smooth boundaries on which the electron reflection is specular. In the diffusive regime (as in the experimental sample in Ref. [7]), the spin relaxation behavior under this assumption is the same as in the case of non-smooth boundaries, because, even when electron trajectories are not randomized by the smooth boundary, they will be immediately randomized by the impurities near the boundaries. In the ballistic regime, the relaxation behaviors in systems with smooth and non-smooth boundaries are different. Here we focus on the simple example of specular reflection. Once the boundary roughness of a ballistic sample is known, the extension to the non-specular case is straightforward.

This chapter is organized by the following way: in Sec. 4.2 the spin relaxation of a homogeneous spin distribution is calculated and a comparison with the experiment is given; in Sec. 4.3 some analytical results are presented useful for understanding the spin relaxation behavior in the ballistic range; Sec. 4.4 is devoted to an analysis of long-lived helix spin distributions, beyond the diffusion theory of Ref. [4]. The conclusion is presented in Sec. 4.5.

4.2 Relaxation of uniform spin modes

The spin relaxation times obtained in the experiments of Ref. [7] were measured in a 2D n-InGaAs channel of the length $L = 200\,\mu$m and the width $w = 0.42 \sim 20\,\mu$m. The SOI in the sample is dominated by the Rashba coupling. In the notation of Ref. [7] it corresponds to the characteristic length $l_{SP} \simeq 1\,\mu$m, which is related to the above defined spin rotation length L_{so} as $L_{so} = 2\,l_{SP}$.

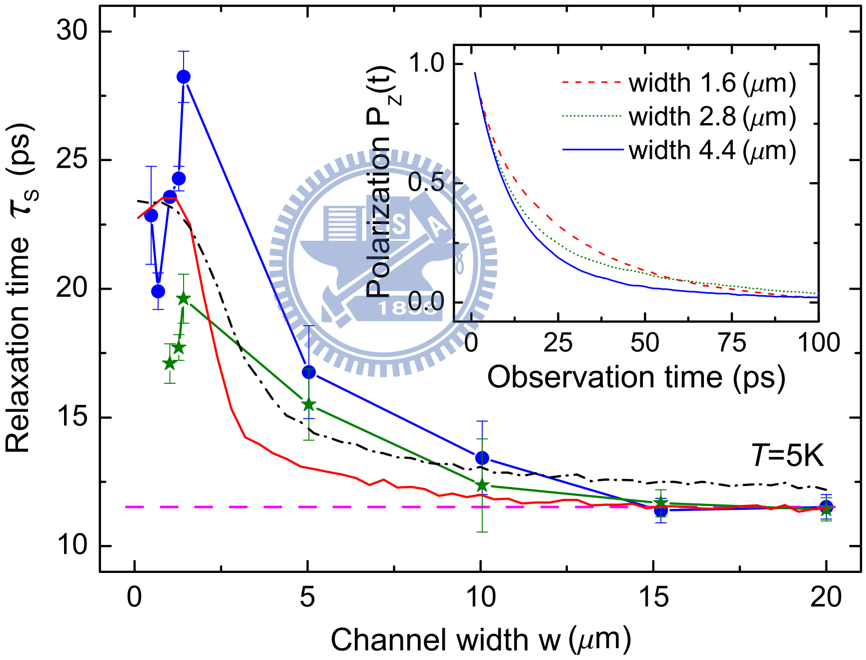

Figure 4.1: The spin relaxation times τ_s's of $[1, 0, 0]$ sample (circle) and $[1, 1, 0]$ sample (star) versus channel width w are taken from the experiments in Ref. [7]. The τ_s calculated by the EMC and SPI methods are extracted from the polarization curve $P_z(t)$, fitted by Eq. (4.1) with free parameters A and c (red solid curve) and with fixed parameters $A = 1$ and $c = 0$ (black dash-dotted curve). The experimental τ_s saturates at $11.5\,\mu$m (pink dashed straight line) for large w, the same as the analytically estimated value for $L_{so} = 2.19\,\mu$m. The inset demonstrates three examples of $P_z(t)$ for channel width $w = 1.6\,\mu$m, $2.8\,\mu$m, and $4.4\,\mu$m.

The sample is characterized by the electron mean free path $l = 0.28\,\mu$m, the momentum scattering time $\tau_M = 0.76$ ps, and its Fermi velocity can accordingly be estimated as $v_F = 0.28\,\mu\text{m}\div 0.76$ ps $\approx 0.37\,\mu\text{m/ps}$. For the carrier concentrations $n_s = 5.4 \sim 7.0 \times 10^{11}$ cm^{-2} used in Ref. [7], the de Broglie wavelength $\lambda_f = \sqrt{2\pi/n_s}$ of electrons in the 2DEG is around 30 $\sim$ 34 nm. The sample was patterned along various crystallographic directions and electron spins have been optically oriented parallel to the growth direction $[0, 0, 1]$. The relaxation times τ_s measured in Ref. [7] are replotted by the circles and the stars connected by the blue and the green curves in Fig. 4.1.

Since the width range $0.4\,\mu\text{m} \leq w \leq 20\,\mu\text{m}$ used in our calculations is much larger than the de Broglie wavelength λ_f, the quantum effects are negligible and the validity of the EMC and SPI approaches is justified. With the above experimental parameters, the EMC and SPI calculations are represented in Fig. 4.1, where the inset shows the relaxation curves $P_z(t)$ for three channels of different widths. All electron spins were initially aligned in $\mathbf{z}$ direction. The relaxation time τ_s can be determined by a fitting of these $P_z(t)$ curves with the exponential function

$$P_z(t) = A \exp(-t/\tau_s) + c. \tag{4.1}$$

For example, the (red) solid curve in Fig. 4.1 represents the relaxation time of 1.2×10^7 electrons in channels of different widths w's. A comparison with the experimental data (circles and stars) leads to following conclusions:

(i) At large widths ($w > 15$ μm), the electron spin can be regarded as relaxing in bulk systems. In the experiments in Ref. l_{SP} was estimated to be $1.0 \pm 0.1\,\mu$m, corresponding to $L_{so} = 2.0 \pm 0.2\,\mu$m. This experimental uncertainty results in $\tau_s = 9.7 \pm 2.1$ ps, when calculated by the EMC and SPI methods. However, each τ_s obtained from the EMC and SPI methods agrees very well with that determined by the analytical expression of DP relaxation $\tau_s = L_{so}^2/(4v_F\,l)$ for boundless systems. Thus, if the experimental samples are governed by pure Rashba Hamiltonian, as in our calculation, these samples most likely have $L_{so} = 2.19\,\mu$m. This value is used in our EMC and SPI simulations to obtain the red and black curves in Fig. 4.1.

(ii) For intermediate widths ($1.4\,\mu\text{m} < w < 15\,\mu$m), there is no an analytical expression for τ_s to compare with. The EMC and SPI result deviates slightly from the experimentally measured τ_s. The maximum deviation is around 3 ps for $[1, 1, 0]$ sample and 4 ps for $[1, 0, 0]$ sample at $w = 5\,\mu$m. The calculated τ_s is closer to the τ_s of the $[1, 1, 0]$ sample.

(iii) For small widths ($w < 1.4\,\mu$m), the experimentally measured τ_s saturates at 28 ps for $[0,0,1]$ sample and 20 ps for $[0,1,1]$ sample. It is assumed in Ref. [7] that this saturation might be related to other mechanisms, like the bulk inversion asymmetry. However, the calculated τ_s in Fig. 4.1 is also bounded by a maximum value around 24 ps, although in our calculation only the Rashba Hamiltonian was considered, without any additional mechanisms involved.

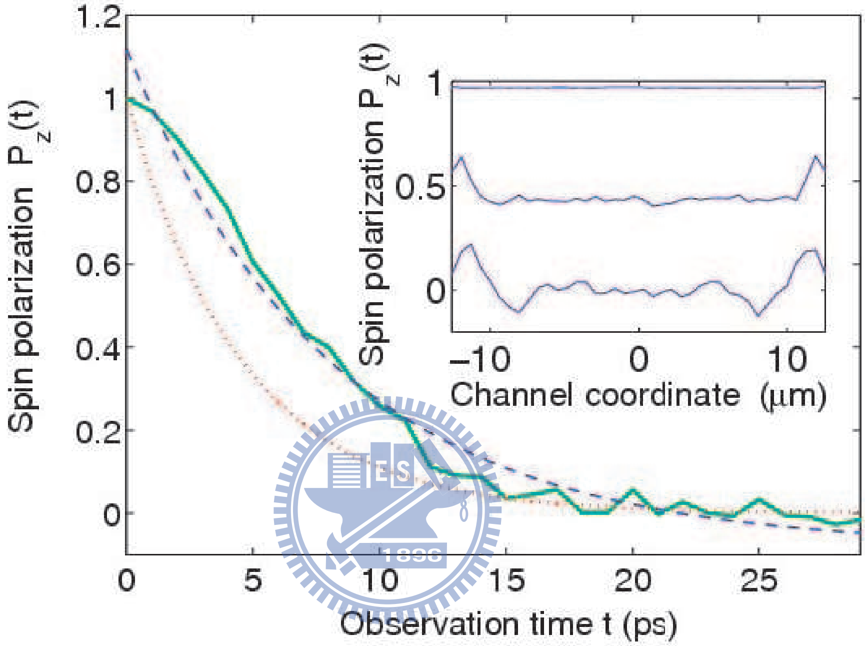

Figure 4.2: In the inset, a spin configuration in a channel of the length 8π μm relaxes to zero, depicted at three different times. These configurations are spatially uniform up to the ripples at two ends caused by boundary effect. Recording the polarization $P_z(t)$ at the middle point of the channel gives the relaxation curve (green solid thick) in the main plot. This curve can be fitted by the exponential function in Eq. (4.1) with $[\tau_s, A, c] = [7.127,\ 1.274,\ -0.055]$ (blue dashed curve) and $[\tau_s, A, c] = [4.323,\ 1,\ 0]$ (red dotted curve). For t close to zero, most electrons have not been reflected by impurities or boundaries. In this range $P_z(t)$ does not behave as an exponential function. Later, after most of the electrons and their spins have been randomized by impurities or boundaries, $P_z(t)$ became more exponential-like. The physical parameters used are $[w, L_{so}, v_F, l] = [0.1\,\mu\text{m}, 2\,\mu\text{m}, 0.37\,\mu\text{m/ps}, 0.3\,\mu\text{m}]$ with 6×10^4 electrons.

An important factor affecting the interpretation of the experimental data is how to determine the relaxation time τ_s from the function $P_z(t)$. The solid curve in Fig. 4.2 is an example of $P_z(t)$ in a channel with $w = 0.1\,\mu$m and $l = 0.3\,\mu$m. At first sight it looks like an exponential function to be fitted with a relaxation time τ_s in Eq. (4.1). But a closer look shows that it is not a pure exponential function. Indeed, if we gradually increase l by reducing the number of impurities in the channel, the monotonically decreasing $P_z(t)$ in Fig. 4.2 will transform to an oscillatory function. In the extreme case of an infinitely thin impurity-free channel, we shall prove in the next section that the evolution of $P_z(t)$ will follow the Bessel function

$$P_z(t) = J_0\left(\frac{2v_F\, t}{L_{so}}\right). \tag{4.2}$$

This analytical formula is depicted by the smooth (red) dashed curve in Fig. 4.3. A corresponding result of a numerical EMC and SPI simulations is plotted as a (green) rugged solid curve in the same figure.

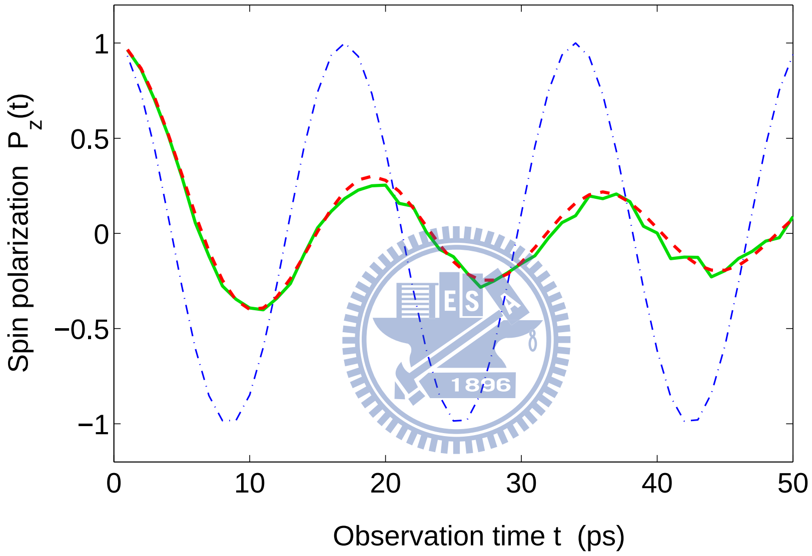

Figure 4.3: In a 1D channel without impurities, a spin polarization $P_z(t)$ behaves like a sinusoidal function Eq. (4.3) (blue dash-dotted curve). In an infinitely thin channel without impurities, $P_z(t)$ behaves like a Bessel function Eq. (4.2) (smooth red dashed curve), which agrees with the numerically obtained $P_z(t)$ simulated by 5×10^4 electrons (rugged green solid curve). The physical parameters are $[w, L_{so}, v_F, l] = [0.1\,\mu\text{m}, 2\,\mu\text{m}, 0.37\,\mu\text{m/ps}, 10^4\,\mu\text{m}]$.

During transition from the diffusive to the ballistic regime, $P_z(t)$ will undergo a crossover from an exponential to a Bessel function. In principle, it is meaningless to use an exponential function to extract τ_s from such a crossover function, especially when it is far from an exponential behavior. But if one would like to carry out this procedure, the so obtained τ_s will depend on the choice of the parameters A and c in Eq. (4.1):

(A) If $A = 1$ is chosen, Eq. (4.1) can precisely fit the real initial polarization

$P_z(t) = 1$ at $t = 0$ (red dotted curve in Fig. 4.2).

If $A \neq 1$, Eq. (4.1) can provide a better fitting to $P_z(t)$ in a wider range of times at $t > 0$ (blue dashed curve in Fig. 4.2). On this reason, such a choice of A seems to be more appropriate.

(B) Further, if $c \neq 0$ the fitted values of c and τ_s will be strongly dependent on the observation time cutoff. The reason is that usually the tail of $P_z(t)$ is oscillating, if the system within the considered range of times is not in the diffusive regime. The closer the system to the ballistic regime, the larger is the oscillation amplitude. The Bessel function in Eq. (4.2) for 'pure' ballistic regime has the largest amplitude. If the non-oscillating Eq. (4.1) is used to fit an oscillating Eq. (4.2) truncated at some cutoff, the fitted τ_s and c will depend on the cutoff. The corresponding uncertainty of τ_s will decrease with an increasing observation time.

In the experiments [7], the width of the channel varies between $w \approx 1.5\,l$ and $70\,l$. Since at the smallest w the system is not far from the ballistic regime, the difference between $P_z(t)$ and the exponential function should be observable. Indeed, the value of τ_s fitted by Eq. (4.1) with $A = 1$ and $c = 0$ (black dash-dotted curve in Fig. 4.1) is somewhat distinct from τ_s at $A \neq 1$ and $c \neq 0$ (red solid curve in Fig. 4.1). Since our observation time is sufficiently long, the fitted value of c is close to zero. A disagreement produced by different fitting procedures will become more remarkable when the system approaches the ballistic regime with strongly oscillating $P_z(t)$. Hence, when comparing τ_s's obtained by different research groups, it is important to know the whole set of the fitting parameters (A, c, and observation time). Even when the same $P_z(t)$ curve is considered, the reported τ_s's could be different. One more problem with the fitting procedure is that even in the diffusive regime the evolution of the spin polarization not necessarily follows the exponential behavior with a single relaxation time. For example, a homogeneous P_z distribution is not an eigenstate of the diffusion equation in a 2D channel. Therefore, as shown in Ref. [6], edge states can contribute to the $P_z(t)$ evolution with the relaxation time different from that of the bulk eigenstate. The weight of edge states increases with decreasing w.

In regime (ii), the experimental data deviate slightly from the EMC and SPI calculations with a maximum difference $\tau_s \approx 3 \sim 4$ ps at $w \approx 5\,\mu$m. This discrepancy is too large to be attributed to different fitting procedures. One of the explanations for such a behavior might be a specific role of long-lived edge states. The lifetime of such modes depends on the boundary conditions [6]. Our

EMC and SPI calculations assumed a specular reflection of electrons from hard wall boundaries of the wire. Probably, the experimental situation in Ref. [7] corresponds to other boundary conditions which give rise to the edge states with larger τ_s. This problem requires a more thorough analysis.

In regime (iii), the relaxation time goes to a finite value at $w \to 0$ in both experimental and EMC and SPI calculated plots in Fig. 4.1. For a homogeneous spin distribution along the channel, the diffusion theory [4] also predicts a saturation of τ_s at $w \to 0$. The saturated value should be twice of the bulk DP spin relaxation time. With the experimental bulk value τ_s=11.5 ps, one expects τ_s=22.8 ps at $w = 0$. Experimental and EMC and SPI curves at Fig. 4.1 are not far from this value, although the diffusion approximation fails at $w \simeq l$. At the same time, one should not forget that in a narrow channel the time evolution of the spin polarization strongly deviates from the exponential function. On this reason, in regime (iii) τ_s can not be a representative parameter to describe the spin relaxation.

4.3 Bessel relaxations in ballistic channels

Depending on the ratio between the channel width and the electron wavelength, one encounters two limiting cases. If the wire carries only one propagating channel, we have effectively a 1D situation. In the opposite limit, if the width of the wire is much larger than the electron wavelength, semiclassical electrons are able to move in both **x** and **y** directions. Therefore, the system is two-dimensional, even if geometrically the channel is narrow, with w much less than other characteristic lengths, such as L_{so} and l. Below, we will consider the evolution of electron polarization in the ballistic regime for these two limiting cases.

1D ballistic channels

Let us consider a 1D impurity-free channel where at $t = 0$ spins of all electrons are aligned in **z** direction. Since impurities and the electron-electron interaction are absent, electrons can only move in $+x$ or $-x$ directions along the channel axis with a constant velocity. The spins of all these electrons will rotate simultaneously along different geodesics connecting the north and south poles on the spin sphere. A 2π spin rotation takes place when an electron passes a distance πL_{so} during a time period $\pi L_{so}/v_F$. Therefore, the angular frequency of this rotation is $2\,v_F/L_{so}$, the same for all spins. The spin polarization at any place in the channel will then evolve according to

$$P_z(t) = \cos\left(\frac{2\, v_F\, t}{L_{so}}\right) \tag{4.3}$$

and oscillate without any amplitude decay, as shown by the blue dash-dotted curve in Fig. 4.3.

2D ballistic channels

Now we suppose that the channel is a 2D thin ballistic wire where all electron spins are initially aligned in the **z** direction, as in the 1D case. Given an observation point, say $p_0(x_0,\, y_0)$ in Fig. 4.4, the polarization $P_z(t)$ at x_0 at time t is the average of the spins of all electrons which will arrive at this moment at the x_0 cross section. These electrons can arrive through a straight trajectory $\overline{p_1 p_0}$ of length $l = v_F t$, or through different zigzag trajectories of the same length, as the path $\widetilde{p_2 p_0}$ in Fig. 4.4.

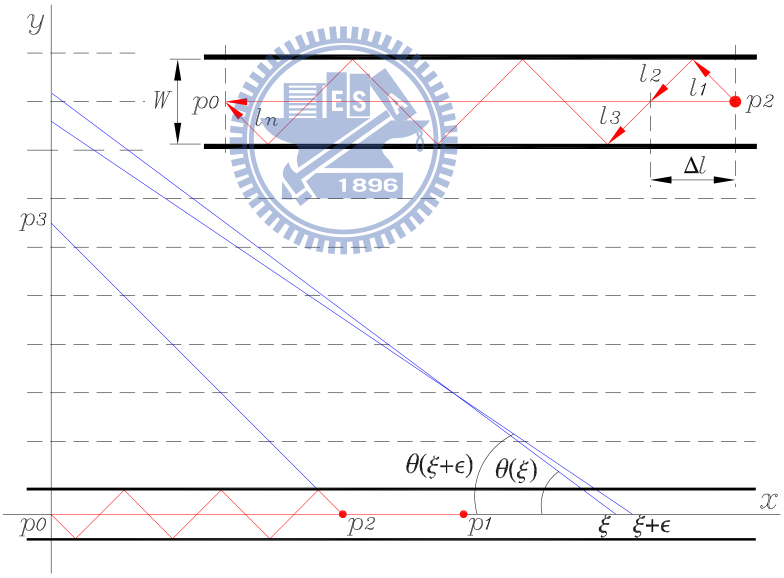

Figure 4.4: Two kinds of trajectories with the same length $l = v_F t$ in a thin channel: the straight trajectory $\overline{p_1 p_0}$ and the zigzag trajectory $\widetilde{p_2 p_0}$. The latter has the same length as the straight line $\overline{p_2 p_3}$, since it can be obtained through a multiple mirror reflection of $\overline{p_2 p_3}$ with respect to the horizontal dotted lines. The symbol $\theta(\xi)$ denotes a certain outgoing angle of an electron located at ξ, as explained in the text. The trajectory $\widetilde{p_2 p_0}$ is magnified in the inset.

As follows from Eq. (2.50), the spin state of an electron running along the zigzag trajectory $\widetilde{p_2 p_0}$ in the inset of Fig. 4.4 will evolve according to the spin evolution operator

$$
\begin{aligned}
U_{\widetilde{p_2p_0}} &= \exp\left(-i\,\frac{\boldsymbol{l}_n\cdot\boldsymbol{\sigma}}{L_{so}}\right)\ldots\exp\left(-i\,\frac{\boldsymbol{l}_2\cdot\boldsymbol{\sigma}}{L_{so}}\right)\exp\left(-i\,\frac{\boldsymbol{l}_1\cdot\boldsymbol{\sigma}}{L_{so}}\right)\\
&= \left[\mathbf{1}-i\,\frac{\boldsymbol{l}_n\cdot\boldsymbol{\sigma}}{L_{so}}+\ldots\right]\ldots\left[\mathbf{1}-i\frac{\boldsymbol{l}_2\cdot\boldsymbol{\sigma}}{L_{so}}+\ldots\right]\left[\mathbf{1}-i\,\frac{\boldsymbol{l}_1\cdot\boldsymbol{\sigma}}{L_{so}}+\ldots\right]\\
&= U_{\overline{p_2p_0}}+O\left(\frac{w^2}{L_{so}^2}\right), \qquad (4.4)
\end{aligned}
$$

Making the above expansion up to the linear in w term, the operator $U_{\overline{p_2p_0}}$ can be written as

$$
U_{\overline{p_2p_0}} := \exp\left(-i\,\frac{\boldsymbol{l}\cdot\boldsymbol{\sigma}}{L_{so}}\right) = \left[\mathbf{1}-i\,\frac{\sum_{j=1}^{n}\boldsymbol{l}_j\cdot\boldsymbol{\sigma}}{L_{so}}+\ldots\right],
$$

with the vector $\boldsymbol{l}$ pointing from p_2 to p_0. Equation (4.4) indicates that the spin evolution of an electron moving along the zigzag trajectory $\widetilde{p_2p_0}$ is approximately the same as that of an electron drifting along the shorter straight line $\overline{p_2p_0}$ with a drift velocity $v_F x/l$ slower than v_F, where $l = |\boldsymbol{l}_1| + |\boldsymbol{l}_2| + \ldots + |\boldsymbol{l}_n|$ and $x = |\boldsymbol{l}_1 + \boldsymbol{l}_2 + \ldots + \boldsymbol{l}_n|$. As discussed in the previous subsection, if an electron moves a distance x, its spin will rotate the angle $2x/L_{so}$ in the spin space. If initially this spin is aligned along the $\mathbf{z}$ direction, its $\mathbf{z}$ component will become

$$
s_z(x) = \cos\left(\frac{2x}{L_{so}}\right)+O\left(\frac{w^2}{L_{so}^2}\right). \qquad (4.5)
$$

To determine how many electrons will contribute to $P_z(t)$, let us uniformly divide the channel axis into small intervals $[\xi_i,\ \xi_{i+1}]$ of length ε separated by points ξ_i with $i = 0,\ 1,\ 2,\ \ldots$. Let $\theta(\xi_i)$ be the outgoing angle of an electron at ξ_i. This angle is chosen so that when the electron travel a zigzag path of the length $l = v_F t$, its drift length will be x. Hence, this electron will arrive at p_0 at time t. If outgoing angles are isotropically distributed, the number of such electrons within $[\xi_i,\ \xi_{i+1}]$ is proportional to the spanned angle $W(\xi_i) = \theta(\xi_i) - \theta(\xi_{i+1})$. For a given small interval $\varepsilon = \xi_{i+1} - \xi_i$ this angle is related to x by

$$
\begin{aligned}
W(x) &= \theta(x)-\theta(x+\varepsilon) = \arccos\left(\frac{x}{l}\right)-\arccos\left(\frac{x+\varepsilon}{l}\right)\\
&= \frac{\varepsilon}{\sqrt{l^2-x^2}}+O\left(\frac{\varepsilon}{l}\right), \qquad (4.6)
\end{aligned}
$$

where the outgoing angle $\theta(x)$ of the trajectory along $\widetilde{p_2p_0}$ is the same as the angle of $\overline{p_2 p_3}$ (see Fig. 4.4). According to Eq. (2.47), the spin polarization $P_z(t)$ at p_0 will be contributed from electrons traveling from different initial locations x:

$$P_z(t) = \frac{\displaystyle\int_0^l \rho\, W(x)\, s_z(x)\, dx}{\displaystyle\int_0^l \rho\, W(x)\, dx}, \tag{4.7}$$

where ρ is the line density of electrons along the channel axis. Inserting Eq. (4.5) and (4.6) into Eq. (4.7) yields

$$\begin{aligned} P_z(t) &= \frac{\displaystyle\int_0^l \frac{\varepsilon}{\sqrt{l^2 - x^2}} \cos\left(\frac{2x}{L_{so}}\right) dx}{\displaystyle\int_0^l \frac{\varepsilon}{\sqrt{l^2 - x^2}}\, dx} \\ &= J_0\left(\frac{2v_F\, t}{L_{so}}\right) + O\left(\frac{w^2}{L_{so}^2}\right), \end{aligned}$$

which at the $w \to 0$ limit is the Bessel function in Eq. (4.2). Hence, uniformly polarized spins in a ballistic narrow channel will relax to the zero polarization through a Bessel function. This phenomenon is in contrast to our conventional intuition that a relaxation is a monotonically exponential process. It is worthwhile to note that the Bessel-like spin dynamics also takes place in other SOI systems [11].

We conclude that the spin relaxation dynamics even in a very thin 2D channel is remarkably different from that in a 1D channel, as can be seen from a comparison of Eq. (4.2) with Eq. (4.3). It can be understood from the fact that no matter how narrow the width of a 2D channel is, it contains a large number of electrons moving along various zigzag trajectories bouncing between two channel boundaries. These trajectories give a significant contribution and change the dynamics of $P_z(t)$ from a sinusoidal oscillation in 1D systems to a Bessel-function decay in 2D systems.

4.4 Relaxation of helix spin modes

In previous sections, all initial electron spins were polarized along the **z** axis. The relaxation dynamics of such spin configuration does not change dramatically at small w (the maximum τ_s only reaches 28 ps in Fig. 4.1.), in agreement with the experiment [7]. In fact, this behavior is expected from the analysis of eigenstates of the spin diffusion equation. As shown in Ref. [4], the only homogeneous eigenstate is Ψ_0 in Fig. 4.5(a), which has all spins polarized in the $\mathbf{y}$ direction and whose relaxation time strongly increases in narrow wires. In addition to this mode there are two nonuniform slowly relaxing eigenstates.

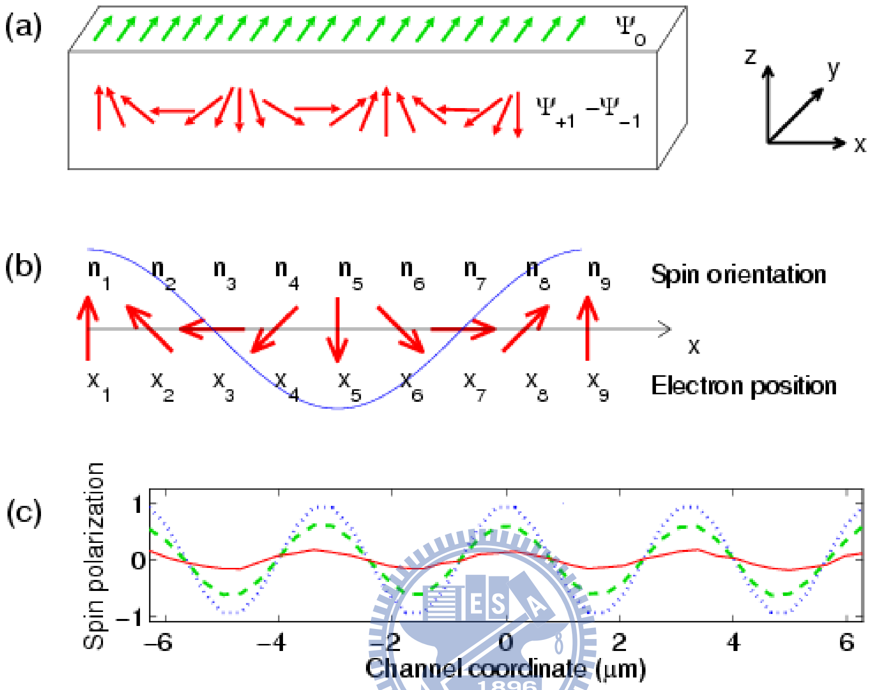

Figure 4.5: (a) Long-lived spin eigenmodes: Ψ_0 denotes the spin mode with all spins aligned in $\mathbf{y}$ direction. $\Psi_{+1} - \Psi_{-1}$ represents the helix spin modes with spin rotating on the $\mathbf{xz}$ plane. (b) An electron in the channel moves a distance πL_{so} from the left end x_1 to the right end x_9. Due to Rashba SOI, the spin of the electron precesses from $\boldsymbol{n}_1$ to $\boldsymbol{n}_9$ and completes a phase period of 2π. (c) A schematic plot of the decay of the helix mode at 1 (dotted), 35 (dash), and 170 (solid) time units. $\Psi_{\pm1}$ in Fig. 4.5(a) has been replaced by $\Psi_{+1} - \Psi_{-1}$.

These two long-lived eigenmodes exist in a 2D channel where $w \ll l_{SP}$. Using a perturbation method with respect to w/l_{SP}, one can solve a diffusion equation and obtain its unperturbed eigensolution [4]

$$\widetilde{\psi}_{M,k,m}(x,y) = \exp(ikx)\chi_m(y)\Psi_M, \tag{4.8}$$

with the eigenvalue (relaxation rate)

$$\Gamma^0_{M,k,m} = D(\pi m/d)^2 + D(k - Ml_{SP}^{-1})^2. \tag{4.9}$$

Therein, Ψ_M are the eigensolutions of the momentum operator J_y with eigenvalues $M = 0, \pm 1$ and $\chi_{2n}(y) = \cos(2\pi yn/d)$, as well as $\chi_{2n+1}(y) = -\sin[\pi y(2n+1)/d]$. In Fig. 4.5(a), $\Psi_{\pm 1}$ will construct the helix eigenmodes with the wave vectors $k = \mp 1/l_{SP}$. We note that the eigenmode of the diffusion equation is a spin configuration exponentially decreasing in time, but its shape remaining unchanged. Taking the second order correction in w/l_{SP}, one obtains

$$\begin{aligned} \Gamma_{M,k,m} &= \Gamma^0_{M,k,m} + \frac{(2-M^2)w^2}{24\tau_{s0}\, l^2_{SP}} && (4.10a) \\ &= \Gamma^0_{M,k,m} + \frac{2(2-M^2)w^2 v_F l}{3L^4_{so}} && (4.10b) \end{aligned}$$

for $\mid k - M/l_{SP} \mid \ll 1/l_{SP}$, where $\tau_{s0} = l^2_{SP}/v_F l$ and $l_{SP} = L_{so}/2$ have been used in the second equality. The modes with $m = 0$, and $k = M/l_{SP}$ will relax most slowly, since in these cases the first term $\Gamma^0_{M,k,m}$ in Eqs. (4.10a) and (4.10b) disappears. The second term indicates that the spin relaxation time $\tau_s = 1/\Gamma_{M,k,m}$ will be proportional to $1/w^2$. In the limit $L_{so} \gg w$, we thus have τ_s much larger than the D'yakonov Perel' relaxation time τ_{s0} in 2D boundless systems [2]. Such a behavior will become more clear from the following simple consideration in a 1D system. Let us consider an electron at x_1 in a 1D channel with an initial spin pointing to $\boldsymbol{n}_1$, as shown in Fig. 4.5(b). Under the Rashba SOI, the spin will rotate to $\boldsymbol{n}_2$, $\boldsymbol{n}_3$, ..., when this electron moves to x_2, x_3, ... It is easy to see that if each electron spin in an initial spin density distribution follows this (x_i, $\boldsymbol{n}_i$) relation, such a distribution will not change in time. Hence, its relaxation time is infinite. In a realistic 2D wire the relaxation time is finite at finite width. That is because electrons there can move in the **y** direction. The polarization $P_z(t)$ contributed from electrons moving along the channel is frozen, as in the 1D case, while electrons moving along the the **y** axis give rise to the relaxation of the helix distribution.

Since the above expressions have been obtained under the assumption $l \ll w \ll L_{so}$, it is interesting to extend the analysis beyond this limits. Within the EMC and SPI methods we studied the relaxation of the helix mode in the range $l \lesssim w$, choosing $L_{so} = 12.5\,\mu$m, $l = 0.5\,\mu$m, and $v_F = 0.37\mu$m/ps. Given the initial helix spin mode $\Psi_{+1} - \Psi_{-1}$ corresponding to spins oriented along the z-axis at x=0 in Fig. 4.5(a), the spin relaxation time $\tau_s(w)$ calculated by the EMC and SPI methods is represented by squares in the inset of Fig. 4.6. In the range of $w < 10\,\mu$m, this time increases dramatically and strongly deviates from the τ_s of the corresponding uniform mode (red solid curve). Note that in order to display the divergent τ_s, we choose a large τ_s-axis scale in the inset of Fig. 4.6. At this scale the uniform mode τ_s (red curve) almost overlaps with the $\tau_s = 0$ axis. The relaxation time of the uniform mode will saturate at some value for $w \to 0$. It is $\tau_s \approx 28$ ps for $[L_{so}, l, w] = [2.19, 0.28, 1.4]\,\mu$m in Fig. 4.1 and $\tau_s \approx 441.1$ ps for $[L_{so}, l, w] = [12.5, 0.5, 0.4]\,\mu$m. In contrast to these uniform modes, τ_s of the helix mode strongly increases for $w \to 0$ (if $w \gg l$). This behavior is consistent with the theoretical result Eq. (4.10a). On the other hand, if w is as large as $20\,\mu$m, the relaxation time ≈ 1927.4 ps of the helix mode is still much larger than $\tau_s \approx 241.0$ ps corresponding to the uniform mode. This difference can be easily seen by magnifying the τ_s-axis of the inset in Fig. 4.6.

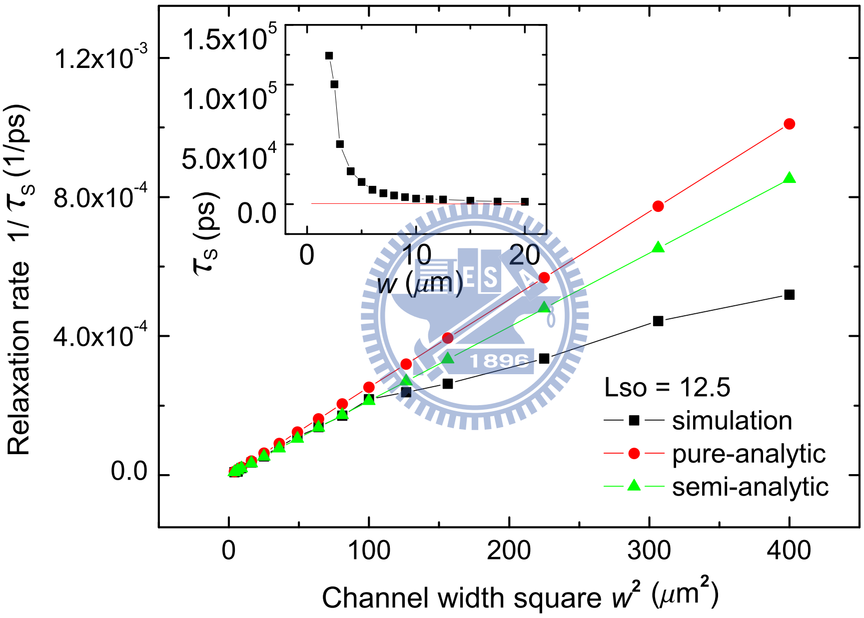

Figure 4.6: The relaxation time τ_s of the uniform mode (red solid) and the helix mode (black square) versus the channel width w in the inset. For small w, the square curve of the helix mode is redrawn as $1/\tau_s$ against w^2 in the main plot, to compare with the τ_s's derived from the analytical formula (4.10b) (red circle) and the semi-analytical formula (4.10a) (green triangular).

The main plot in Fig. 4.6 shows the $1/\tau_s$ dependence on w^2. The squares show the helix relaxation rate corresponding to the data in the inset. The line with circles for the helix mode is obtained from the analytical expression Eq. (4.10b), while the line with triangles is obtained from Eq. (4.10a). In the latter line, τ_{s0} is simulated numerically, instead of using the analytical relation $\tau_{s0} = l_{SP}^2/v_F l$ mentioned below Eq. (4.10b). The lines with circles and triangles are valid only at $l \ll w \ll L_{so}$, while that with squares is valid for all w. One can clearly see that the curve calculated by the EMC and SPI methods agrees very well with Eqs. (4.10a) and (4.10b) at small w between $w_1 = 2\,\mu\text{m}$ (the smallest calculated width) and $w_2 = 10\,\mu\text{m}$. It is interesting to note that although formula Eq. (4.10a) and (4.10b) was derived under the condition $l \ll w \ll L_{so}$, it seems to be valid in a wider range of w, because w_1 is close to the ballistic regime crossover point at $w \sim l = 0.5\,\mu\text{m}$ and w_2 is close to $L_{so} = 12.5\,\mu\text{m}$. Finally, one should not expect that the linear trend in Fig. 4.6 can continue down to $w^2 \to 0$ because in this range the system will eventually reach the ballistic regime and $P_z(t)$ will decay like a crossover function between the exponential and the Bessel functions. Similar to the discussion of the uniform initial spin configuration in Section 4.2, it does not make sense to consider τ_s at extremely small w, because $P_z(t)$ is no longer an exponential function.

4.5 Conclusion

The ensemble Monte Carlo method and semiclassical path integral method has been applied to study the spin relaxation in thin 2D wires with the Rashba spin-orbit interaction. We considered the relaxation of a uniform spin polarization along the **z** axis, as well as of the long-lived helix mode. In the former case we found a good agreement of τ_s calculated in the regime of large w ($w \approx 20\,\mu\text{m}$) with the well known bulk DP spin relaxation rate and with the experimental data from Ref. [7]. At smaller w our numerical results deviate slightly from the experimental data. The nature of this distinction is not clear. We assume that the edge spin diffusion modes can contribute to the spin relaxation, so that the conditions for electron reflections from the wire lateral boundaries become important. Also, the Dresselhaus spin orbit interaction can give rise to the observed dependence of τ_s on the orientation of the wire axis in the **xy** plane. At $w \to 0$ the relaxation time has a tendency to saturate at a value which is about twice of the bulk τ_s, as predicted by the spin diffusion theory. Although both EMC-SPI and experimental data show similar saturation behavior, one must take into account that at w approaching the crossover $w \sim l_f$ to the ballistic regime the evolution of the spin polarization can not be described by an exponential function. Hence, in this regime τ_s is not a representative parameter to describe the spin relaxation. We studied the evolution of the spin polarization in the ballistic regime and found that it is described by the Bessel function. The numerical EMC and SPI results fit well to this behavior. For the helix spin distribution, the linear dependence of $1/\tau_s$ on w^2 predicted in the framework of the diffusion theory [4] coincides precisely with that calculated by the EMC and SPI methods. The EMC and SPI methods also allowed to calculate the spin relaxation beyond the constraints of those analytic results [4].

Bibliography

[1] S. A. Wolf *et al.*, Science **294**, 1488 (2001); I. Zütic, J. Fabian, S. D. Sarma, Rev. Mod. Phys. **76**, 323 (2004); G. A. Prinz, Phys. Today **48(4)**, 58 (1995).

[2] M. I. D'yakonov and V. I. Perel', Sov. Phys. Solid State **13**, 3023 (1971).

[3] C.-H. Chang, A. G. Mal'shukov, and K. A. Chao, Phys. Rev. B **70**, 245309 (2004).

[4] A. G. Mal'shukov and K. A. Chao, Phys. Rev. B **61**, R2413 (2000).

[5] A. A. Kiselev and K. W. Kim, Phys. Rev. B **61**, 13 115 (2000).

[6] P. Schwab, M. Dzierzawa, C. Gorini, and R. Raimondi, Phys. Rev. B **74**, 155316 (2006).

[7] A. W. Holleitner, V. Sih, R. C. Myers, A. C. Gossard, and D. D. Awschalom, Phys. Rev. Lett. **97**, 036805 (2006).

[8] C.-H. Chang, A. G. Mal'shukov, and K. A. Chao, Phys. Lett. A **326**, 436 (2004).

[9] A.G. Mal'shukov, V.V. Shlyapin and K. A. Chao, Phys. Rev. B **66**, 081311(R) (2002).

[10] H. Chen, J. J. Heremans, J. A. Peters, A. O. Govorov, N. Goel, S. J. Chung, and M. B. Santos, Appl. Phys. Lett. **86**, 032113 (2005).

[11] D. Culcer and R. Winkler, Phys. Rev. B **76**, 195204 (2007).

Part II

Hydrodynamic Interactions Between Microorganism Flagella

Chapter 5

Flagellum Model under Hydrodynamic Interactions

5.1 Introduction

There are enormous swimming microorganisms living in our world. Examples include the bacteria inhabiting in our guts, the protozoa swimming in the ponds, and the algae living in the ocean. The reasons of these microorganisms move are similar. For instance, bacteria detect and move to high concentration area of nutrients; spermatozoa of many organisms swim to the ovum; cells swim to evade predators. However, the swimming strategies they use are very different from those employed by large organisms. This difference is ascribed to the low Reynolds number environment where the microorganisms live. In this environment, the damping of viscosity is paramount and inertia of the system is negligible. Swimming strategies employed by larger organisms at high Reynolds number, such as insets, birds, and fishes, are ineffective at the small scale. So that microorganisms have evolved propulsion strategies that successfully overcome their external drags. Many microorganisms use one or more appendages, termed flagellum, for propulsion. The appendages could be a relative stiff helix that is rotated by a motor embedded in the cell wall, or it could be a flexible filament undergoing whip-like motions due to the action of molecular motors distributed along the length of the filament [1].

In addition, these microorganisms usually live in a population status. Their behaviors are similar to those of the populations of macroscopic organisms, such as the wingless locusts marching, a vortex of fish school, a herd of zebra, and human traffics [2]. These systems usually have nontrivial collective motions, which cannot be easily predicted from their individual motions. Since the flagella of microorganisms quite often live in a population status, their behaviors are expected to exhibit collective effects. Studying the collective behaviors of flagella is not just due to scientific curiosity. It may also offer some real potential applications [3]. Concerning the techniques for exploring flagellum behaviors, there are at lease two possibilities. One is to observe the swimming response of these microorganisms when they swim in free space. The other is to examine the flagella response of these microorganisms when we confine these microorganisms bodies, says by optical tweezers, or immobile the microorganism bodies on a substrate surface. The former offers a comparatively realistic environment to reveal the flagellum behavior. But due to the larger degree of freedom, says the cell bodies movement and their flagella action constitute two degrees of freedom, more efforts needs to be paid to clarify the interaction between them. On the other hand, the later offers an examination environment which decreases the degree of freedom, the degree of freedom of the cell bodies movement is removed. So that the effect due to pure microorganisms flagella action behavior may be exhibited more clearly.

The microorganism carpet is a suitable experimental setup for the later approach [4]. But according to the resolution limitation of the present experimental instruments, sometimes it is still hard to realize the microorganisms flagella behavior by means of direct observation on the microorganism carpet itself. One of the strategies to overcome this obstacle is examine the tracer particle response, which is controlled at some height located over the microorganism carpet. In this article, in order to reveal the secret of the microorganisms flagella action behavior when they stay together to form a carpet, we propose a simplified microorganism-flagellum-rotor (MFR) matrix model, $\mathrm{MFR}_{\mathrm{matrix}}$, to mimic and effectively catch the real microorganism flagellum carpet behavior. The tracer particle response, which is directly mapped to the MFR matrix behavior, is presented and expected from theoretical and numerical approaches. We hope to *inversely* reveal the secret and the unknown of the MFR matrix behavior by means of *directly* observing and realizing the tracer particle response.

5.2 Microorganism-Flagellum-Rotor Model and Blake-Oseen Tensor Role

In our study, we offer a microorganism-flagellum-rotor (MFR) model to replace the so complex real microorganism flagellum, says helical-like flagellum, action behavior [5]. The MFR model is a rotor-like unit. To try to catch the whole effects produced by real microorganism flagellum, the MFR model is represented by some specified characteristic parameters. They are the rotor hight h (measured from the microorganisms planted substrate surface), rotor arm length r, rotor sphere radius a, and a thrust $\mathbf{F}_{\mathrm{th}}$ with strength F_{th} and zenith angle α and azimuthal angle β.

Note that in our analytical and numerical calculation, we treat each MFR as an *active* unit and follow the torque-speed relationship under some ion concentration [6]. This calculation strategy or assumption implies that we assign a specific strength F_{th} to each active MFR regardless of such MFR now may stays in the status which with different, higher or lower, rotation rate compared with others. The situation $\beta = 0$ is a singularity point in our calculation strategy. Since a reasonable physical picture suggests that the rotation rate of a studied MFR and the corresponding F_{th} should be zero in the situation $\beta = 0$. But base on our calculation strategy, in the situation $\beta = 0$ the $\mathbf{F}_{\mathrm{th}}$ is still assigned with a non-zero strength F_{th}. Anyhow, although such calculation strategy may cause something strange and unmeaning results in some cases, e.g., some results appeared in the circular motion mode (discussed in Subsection 6.3.1 and Figure 6.5). But it's not necessary to worry about these special cases too much, the important thing we have to keep in mind is that such calculation strategy offers two points of view to treat all studied cases in this article. The first is that it offers an absolute point of view to see what happens when we vary the strength of the thrust $\mathbf{F}_{\mathrm{th}}$ for the studied cases. The second is that it gives a relative point of view to look into what's going on when vary the ratio, ratio of normal, tangential, and z direction components of the thrust $\mathbf{F}_{\mathrm{th}}$, for the studied cases. The calculation results can be understood and reflected by both the absolute value assignment and the relative value assignment approaches for this $\mathbf{F}_{\mathrm{th}}$ parameter.

To explore the interaction between two MFRs or $N \times N$ MFRs which make up a MFR matrix. We need to assign an additional parameter d, the space between two MFRs, into our studied MFR matrix system. If we consider further step the tracer particle response. Another two parameters have to be considered for the MFR matrix system, that is the tracer particle located height H (measured from the microorganisms planted substrate surface) and the tracer particle bead radius, b. So the whole parameter set specified for the MFR matrix configuration is denoted by

$$\begin{aligned} \mathrm{MFR}_{\mathrm{matrix}} &\equiv [H, b, N \times N, h, d, r, a, \mathrm{F}_{\mathrm{th}}, \alpha, \beta] \\ &\quad (\mu\mathrm{m}, \mathrm{pN}, \text{degree or radian}). \end{aligned}$$

Thereafter it acts as a standard parameter set representation to assign our specified study case. Figure 5.1 (a) depicts the detailed aspects about these parameters tagged on the MFR matrix configuration.

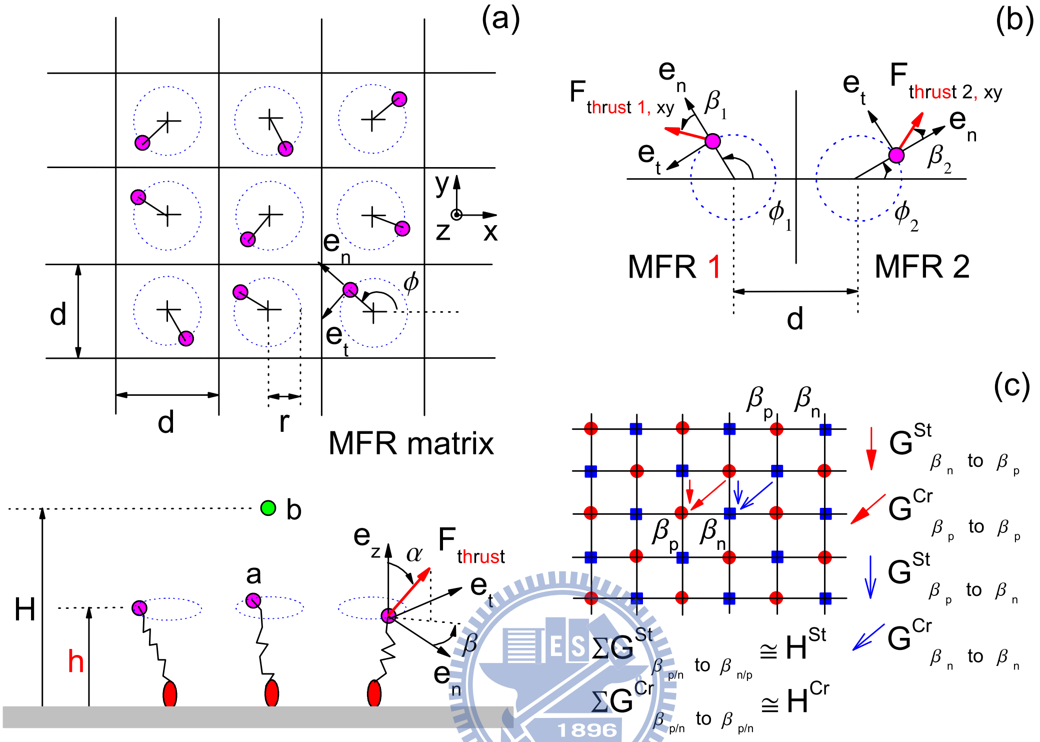

Figure 5.1: The top view (upper part) and front view (lower part) of the MFR matrix system is depicted in (a). The magenta sphere is the bead which attached on the arm end of the MFR, and the green sphere means the tracer particle. The top view of two MFRs system is depicted in (b). The checkerboard-like configuration of MFR matrix is shown in (c). The red circles and blue squares indicate the position of each MFR arm bead, where β_p and β_n tagged on them denote two different types of azimuthal angles.

Remember that the microorganisms live at low Reynolds number environment. The suitable description for these microorganisms flagella action and our MFR model is the Stokes equation for the hydrodynamic flow field $\mathbf{v}$

$$\eta\nabla^2\mathbf{v} = -\nabla P, \tag{5.1}$$

where the pressure P is a Lagrange multiplier to impose the constraint of incompressibility, $\nabla\cdot\mathbf{v} = 0$. The far field generated by a moving sphere in the vicinity of a surface can be calculated by considering the solution of the Stokes equation to a point-like force $\mathbf{F}_i$ at position $\mathbf{x}_i = \langle x_i, y_i, z_i \rangle$, which is of the form

$$\mathbf{v}(\mathbf{x}) = G(\mathbf{x}_i, \mathbf{x})\mathbf{F}_i. \tag{5.2}$$

The tensor G, termed Black-Oseen tensor (BOT), consists of a Stokeslet G^S, which describes the flow field around a small isolated particle, and an image, required to satisfy the no-slip boundary condition on the surface [7]. The image is located at the particle position, mirrored over the surface plane, $\widetilde{\mathbf{x}}_i = \mathbf{x}_i - 2z_i\mathbf{e}_z$, and consists of an anti-Stokeslet, a Stokes doublet G^{StoD}, and a source doublet G^{SouD}. The complete BOT G^C has the form

$$\begin{aligned} G^C(\mathbf{x}_i, \mathbf{x}) &= G^S(\mathbf{x} - \mathbf{x}_i) - G^S(\mathbf{x} - \widetilde{\mathbf{x}}_i) \\ &- 2z_i G^{StoD}(\mathbf{x} - \widetilde{\mathbf{x}}_i) + 2z_i^2 G^{SouD}(\mathbf{x} - \widetilde{\mathbf{x}}_i), \end{aligned} \tag{5.3}$$

with

$$\begin{aligned} G^S_{\alpha\beta}(\mathbf{x}) &= \frac{1}{8\pi\eta}\left(\frac{\delta_{\alpha\beta}}{|\mathbf{x}|} + \frac{x_\alpha x_\beta}{|\mathbf{x}|^3}\right), \\ G^{StoD}_{\alpha\beta}(\mathbf{x}) &= (1 - 2\delta_{\beta z})\frac{\partial}{\partial x_\beta} G^S_{\alpha z}(\mathbf{x}), \\ G^{SouD}_{\alpha\beta}(\mathbf{x}) &= \frac{1}{8\pi\eta}(1 - 2\delta_{\beta z})\frac{\partial}{\partial x_\beta}\left(\frac{x_\alpha}{|\mathbf{x}|^3}\right), \end{aligned} \tag{5.4}$$

where η is the fluid viscosity. The leading behavior of G^C which describes the far field, for $R \gg z_i, z$, can be recast as

$$G^A(\mathbf{x}_i, \mathbf{x}) \approx \frac{3}{2\pi\eta}\frac{z_i z}{R^3}\begin{pmatrix} \cos^2\varphi & \sin\varphi\cos\varphi & 0 \\ \sin\varphi\cos\varphi & \sin^2\varphi & 0 \\ 0 & 0 & 0 \end{pmatrix}, \tag{5.5}$$

where $\tan\varphi = (y_i - y)/(x_i - x)$ and $R^2 = (x_i - x)^2 + (y_i - y)^2$ [8].

Consider the rotation rate of an MFR member i which lay in an $N \times N$ MFR matrix. The bead center of this MFR member i is indicated by the position vector $\mathbf{x}_i = \langle x_i, y_i, z_i \rangle$. The complete equation of motion for the bead attached on this

MFR member i can be cast as

$$\begin{aligned}\mathbf{r}_i \times m_a \ddot{\mathbf{x}}_i &= \mathbf{r}_i \times (-\gamma \dot{\mathbf{x}}_i) + \mathbf{r}_i \times \mathbf{F}_{\text{thermal}} + \mathbf{r}_i \times \mathbf{F}_{\text{th},i} \\ &\quad + \sum_{j=1, j\neq i}^{N\times N} \mathbf{r}_i \times \mathbf{F}_{\text{th},j}^{BOT} + \mathbf{r}_i \times \mathbf{F}_{\text{external}}, \qquad (5.6)\end{aligned}$$

where $\mathbf{r}_i = r\mathbf{e}_{n,i}$ is the arm vector of such MFR member i, $\mathbf{e}_{n,i}$ is the normal component unit vector attached on the bead of the MFR member i as shown in Figure 5.1 (a); m_a is the bead mass of the MFR; $\gamma = 6\pi\eta a$ is the Stokes drag constant; $\mathbf{F}_{\text{thermal}}$ is the external forces induced by thermal fluctuation; $\mathbf{F}_{\text{th},j}^{BOT}$ is the equivalent force acting on the arm bead of the MFR member i which is induced from $\mathbf{F}_{\text{th},j}$ by means of BOT hydrodynamic interaction; and $\mathbf{F}_{\text{external}}$ is the other possible external forces which is excluded from those forces mentioned above, for example, the optical tweezers trapping force is one of the possible forces $\mathbf{F}_{\text{external}}$. Consider the $\mathbf{e}_z$ direction components of these torque terms described in equation (5.6). By neglecting the inertia term, and does not consider the thermal fluctuation temporarily and other external forces except for the hydrodynamic interaction which comes from other member j of this MFR matrix. Equation (5.6) can be simplified and represented as

$$\omega_i(t) = \frac{1}{r}\left(\frac{1}{\gamma}\mathbf{F}_{\text{th},i} + \left\{\sum_{j=1,j\neq i}^{N\times N} G(\mathbf{x}_j, \mathbf{x}_i)\mathbf{F}_{\text{th},j}\right\}\right)\cdot \mathbf{e}_{t,i}, \qquad (5.7)$$

where $\omega_i(t) = \frac{1}{r}\left(\mathbf{e}_{n,i} \times \dot{\mathbf{x}}_i\right)\cdot \mathbf{e}_z$ is the rotation rate of MFR member i in an $N \times N$ MFR matrix.

If we look into the tracer particle response, which is located at position $\mathbf{x} = \langle x, y, H\rangle$. The complete equation of motion for the tracer particle bead can be wrote down as

$$m_b\ddot{\mathbf{x}} = (-\gamma\dot{\mathbf{x}}) + \mathbf{F}_{\text{thermal}} + \sum_{j=1}^{N\times N} \mathbf{F}_{\text{th},j}^{BOT} + \mathbf{F}_{\text{external}}, \qquad (5.8)$$

where m_b is the tracer particle bead mass, and $\mathbf{F}_{\text{th},j}^{BOT}$ is the equivalent force acting on this tracer particle bead which is induced from $\mathbf{F}_{\text{th},j}$ by means of BOT hydrodynamic interaction. Follow the similar simplification procedure as done on equation (5.6). The simplified flow field acting on the tracer particle, which is produced only from all $N \times N$ members of an MFR matrix, can be represented as

$$\mathbf{u}(t) = \sum_{j=1}^{N\times N} \{G(\mathbf{x}_j, \mathbf{x})\mathbf{F}_{\mathrm{th},j}\}, \tag{5.9}$$

where $\mathbf{u}(t) = \dot{\mathbf{x}}$ is the flow field around the tracer particle. Equations (5.7) and (5.9) govern our study main content in this article. But because that there are some nontrivial characteristics embedded in them, a lot of interesting results should be produced from these nontrivial characteristics. We should represent and discuss these findings below.

Bibliography

[1] E. Lauga and T. R. Powers, Rep. Prog. Phys. **72**, 096601 (2009).

[2] T. Vicsek and A. Zafeiris, Phys. Rep. **517**, 71 (2012).

[3] M. J. Kim and K. S. Breuer, J. Fluid. Eng. **129**, 319 (2007); E. Steager, C.-B. Kim, J. Patel, S. Bith, C. Naik, L. Reber and M. J. Kim, Appl. Phys. Lett. **90**, 263901 (2007); M. J. Kim and K. S. Breuer, Small **4**, 111 (2008); A. Sokolov, M. M. Apodaca, B. A. Grzybowski and I. S. Aranson, Proc. Natl. Acad. Sci. U.S.A. **107**, 969 (2010).

[4] N. Darnton, L. Turner, K. Breuer and H. C. Berg, Biophys. J. **86**, 1863 (2004).

[5] N. Uchida and R. Golestanian, Phys. Rev. Lett. **104**, 178103 (2010).

[6] Y. Sowa, H. Hotta, M. Homma and A. Ishijima J. Mol. Biol. **327**, 1043 (2003).

[7] J. R. Blake, Proc. Cambridge Philos. Soc. **70**, 303 (1971).

[8] A. Vilfan and F. Jülicher , Phys. Rev. Lett. **96**, 058102 (2006).

Chapter 6

Tracer Particle Responses on Microorganism Flagellum Matrixes

6.1 Introduction

Motivated by the scientific curiosity and possible applications of microorganism flagellum matrix. Two minimal models, the microorganism-flagellum-rotor matrix ($\mathrm{MFR}_{\mathrm{matrix}}$) model introduced in Chapter 5.2 and microorganism-flagellum-rotor sweep ($\mathrm{MFR}_{\mathrm{sweep}}$) model are proposed to mimic the complex real microorganism flagellum rotation and sweep behaviors. In these two models , the hydrodynamic interaction described by the complete BOT, G^C, and its far field limit, G^A, are considered. The key issues to explore include (1) the collective motions of two MFRs, (2) the collective motions of an $N \times N$ MFR matrix, and (3) the behavior of a tracer particle exposed to an $N \times N$ MFR matrix. For (1), the solution of the synchronized motion can be analytically derived and a phase portrait is presented to show how the dynamics of the system converges to this motion. For (2), the conditions for synchronization, repellency, and freezing states are studied and the rotation rates of synchronization and repellency states are investigated. For (3), the tracer particle is found to response to the MFR matrix by three modes: circular motion (CM), linear oscillation (LO), and a sharp jumping (SJ). These behaviors of $\mathrm{MFR}_{\mathrm{matrix}}$ and $\mathrm{MFR}_{\mathrm{sweep}}$ can reasonably explain the results of some recent experiments of bacterial carpets.

6.2 The collective motions of MFRs

6.2.1 Two MFRs

Let us explore the hydrodynamic interaction between two MFRs. The system layout is depicted in Figure 5.1 (b), and Figure 5.1 (a) offers a three-dimensional structure configuration as reference. Consider the following special case, we examine two same MFRs and imposed the conditions $\beta_1 = \beta_2$ ($\beta_1 = -\beta_2$) and $d \gg r$ in them. By applying approximation G^A (equation (5.5)) we can write down the explicit forms of the rotation rates ω_1 and ω_2 for the two MFRs, respectively. If we assume the two MFRs enter into synchronization state (repellency state) as time goes on, and set a new variable $\phi = \Delta\phi = \phi_1 - \phi_2$ ($\phi = \Sigma\phi = \phi_1 + \phi_2$). Surprisingly, we find the two rotation rates $\omega_1 = \frac{d\phi_1}{dt}$ and $\omega_2 = \frac{d\phi_2}{dt}$ can combine into one simple expression

$$\mathcal{C}_0 \frac{d^2\phi}{dt^2} = -\frac{d\phi}{dt} + \mathcal{C} \cos\beta \sin\phi, \tag{6.1}$$

where $\mathcal{C}_0$ is an artificial coefficient which is just applied for representing the phase diagram ϕ - $\frac{d\phi}{dt}$ evolution, and $\mathcal{C} = -\frac{3}{2\pi\eta}\frac{h^2}{rd^3}\mathrm{F}_{\mathrm{th}}$ is the evolution coefficient for this two MFRs system. To illustrate numerically the phase diagram evolution, we assume $\eta = 1.5 \times 10^{-6}(\frac{\mu\mathrm{g}}{\mu\mathrm{m}\mu\mathrm{s}})$ that treated as a standard value and employed thereafter without change unless mentioned specially, and the standard parameter set $[H, b, N \times N, h, d, r, a, \mathrm{F}_{\mathrm{th}}, \alpha, \beta] = [\times, \times, 1 \times 2, 10, 15, 5, 1, 10, \frac{\pi}{2}, \frac{\pi}{6}]$ to calculate $\mathcal{C}$, and set $\mathcal{C}_0 = \mathcal{C}$ as both with the similar evolution strength. Here we give a very profound notice about the specification of the strength of $\mathbf{F}_{\mathrm{th}}$. In general, the strength of $\mathbf{F}_{\mathrm{th}}$ is just about in the order $\mathrm{F}_{\mathrm{th}} = 0.1$ (pN) in our considered system. The reason that we assume $\mathrm{F}_{\mathrm{th}} = 10$ (pN), this value treated as a standard value for calculation here and thereafter, is due to it can save the computer calculation time and does not lose the underlay physical intrinsic properties. The phase diagram, ϕ - $\frac{d\phi}{dt}$ evolution of expression (6.1), is depicted in Figure 6.1. As time goes on, the two MFRs system enters into a fixed point, it implies the synchronization state or repellency (and freezing) state. For checking further step whether this tendency is dependent on the assumption of the hydrodynamic interaction forms, G^C or G^A. We numerically calculate the hydrodynamic interaction between two MFRs by utilizing complete G^C. We find this tendency is still established well. These phenomena possibly imply and suggest that when we extend two MFRs system to MFR matrix system, the synchronization and repellency (and freezing) states can exist stably under some specified conditions.

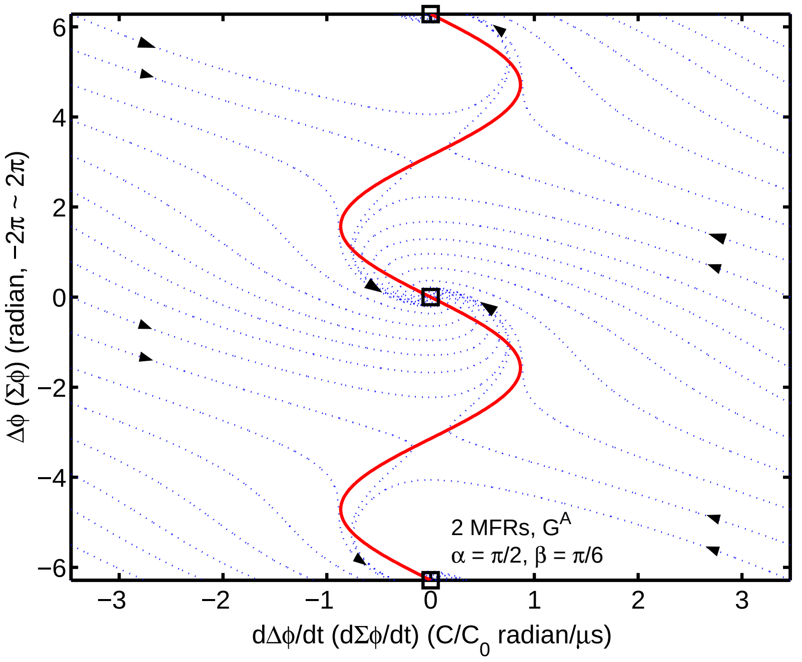

Figure 6.1: The ϕ - $\frac{d\phi}{dt}$ phase diagram, which is plotted from equation (6.1). Equation (6.1) is deduced by utilizing G^A (equation (5.5)). Note that both cases $\phi = \Delta\phi = \phi_1 - \phi_2$ and $\phi = \Sigma\phi = \phi_1 + \phi_2$ give us the same phase diagram. The red bold curve is the plot of the limiting case $\frac{\mathcal{C}_0}{\mathcal{C}} = 0$ in equation (6.1). The three black blank squares depict the fixed points of this two MFRs system.

6.2.2 Synchronization state in a uniform MFR matrix

Let us apply equation (5.7) and give the condition $\beta_i = \beta$ for all members i of the studied MFR matrix. The system configuration is shown in Figure 5(a). Assume all members i of this MFR matrix enter into synchronization state, then equation (5.7) can be simplified as

$$\begin{aligned} \omega_i(t) &\approx \frac{1}{r}\left(\frac{1}{\gamma}\mathbf{F}_{\text{th}} + \left\{\sum_{j=1,j\neq i}^{N\times N} G(\mathbf{x}_j,\mathbf{x}_i)\right\}\mathbf{F}_{\text{th}}\right)\cdot\mathbf{e}_t \\ &\approx \frac{1}{r}\left(\frac{1}{\gamma}\mathbf{F}_{\text{th}} + \zeta\mathcal{G}_{RR}\mathbf{F}_{\text{th}}\right)\cdot\mathbf{e}_t \\ &\approx \frac{1}{r}\mathrm{F}_{\text{th}}\sin\alpha\sin\beta\left(\frac{1}{\gamma} + \zeta\mathcal{G}_{RR,11}\right). \end{aligned} \tag{6.2}$$

Here base on the numerical calculation analysis, we define

$$\begin{aligned} \zeta \mathcal{G}^{C/A}_{RR} &= \left\{ \sum_{j=1,j\neq i}^{N\times N} G^{C/A}(\mathbf{x}_j,\mathbf{x}_i) \right\} \\ &\approx \zeta \begin{pmatrix} \mathcal{G}^{C/A}_{RR,11} & & 0 \\ & \mathcal{G}^{C/A}_{RR,22} & \\ 0 & & \mathcal{G}^{C/A}_{RR,33} \end{pmatrix} \\ &\approx \zeta \mathcal{G}^{C/A}_{RR,11} \begin{pmatrix} 1 & & 0 \\ & 1 & \\ 0 & & \delta^{C/A}_{RR} \end{pmatrix}, \end{aligned} \tag{6.3}$$

where $\delta^{C}_{RR} \approx 1$ for small $N \times N$ but $\delta^{C}_{RR} \approx 0$ for large $N \times N$, and $\delta^{A}_{RR} = 0$ for all $N \times N$, and $\zeta = \frac{3}{2\pi\eta}\frac{h^2}{d^3}$ is a normalized unit which is related to the leading behavior of G^C. Here and thereafter the superscripts C/A attached on each tensors, says $\mathcal{G}$, $\mathcal{H}$ and $\mathcal{I}$, denote that they are calculated by applied $G^{C/A}$, respectively. Look into deeply the equation (6.3), we find $\mathcal{G}_{RR}$ is just like a function of variables h, d, r and N. We can treat $\mathcal{G}_{RR}$ as a pure geometry function determined only by this studied MFR matrix configuration.

Apply equations (6.2) and (6.3), the semi-analytical calculation result of ω_i by utilizing both $G^{C/A}$ is plotted in Figure 6.2. Note that ω_i, here plotted in Figure 6.2, is the rotation rate of member i MFR which located at around the center region of the studied MFR matrix. It acts as a representative role. Because that due to the loss of the symmetric property for a finite members MFR matrix, ω_i should exhibit somewhat difference between the member i located at around the center region and near around the marginal region. Figure 6.2 also shows the numerical calculation result of ω_i by inputing the standard parameter set $[H, b, N \times N, h, d, r, a, \mathrm{F}_{\mathrm{th}}, \alpha, \beta] = [\times, \times, 50 \times 50, 10, 15, 5, 1, 10, 90^\circ, 0^\circ \sim 40^\circ]$ specified for the MFR matrix configuration. At the same time, the normalization unit $\zeta = \frac{3}{2\pi\eta}\frac{h^2}{d^3} \approx 9.4314 \times 10^3 (\frac{\mu\mathrm{s}}{\mu\mathrm{g}})$ is obtained, this value is treated as a standard one applied here and thereafter without change unless mentioned specially. It shows that the semi-analytical and numerical calculation results are very consistent in the region $\beta = 0^\circ \sim 40^\circ$ for both $G^{C/A}$. We also find that when $\beta > 40^\circ$ the MFR matrix system enters into vortex or random phase state, regardless of the calculation is for cases $G^{C/A}$ and for almost various MFR matrix configuration that specified by various parameter sets. This is a very interesting phenomenon. There seems to exist a universal critical azimuthal angle $\beta \approx 40^\circ$ which switches

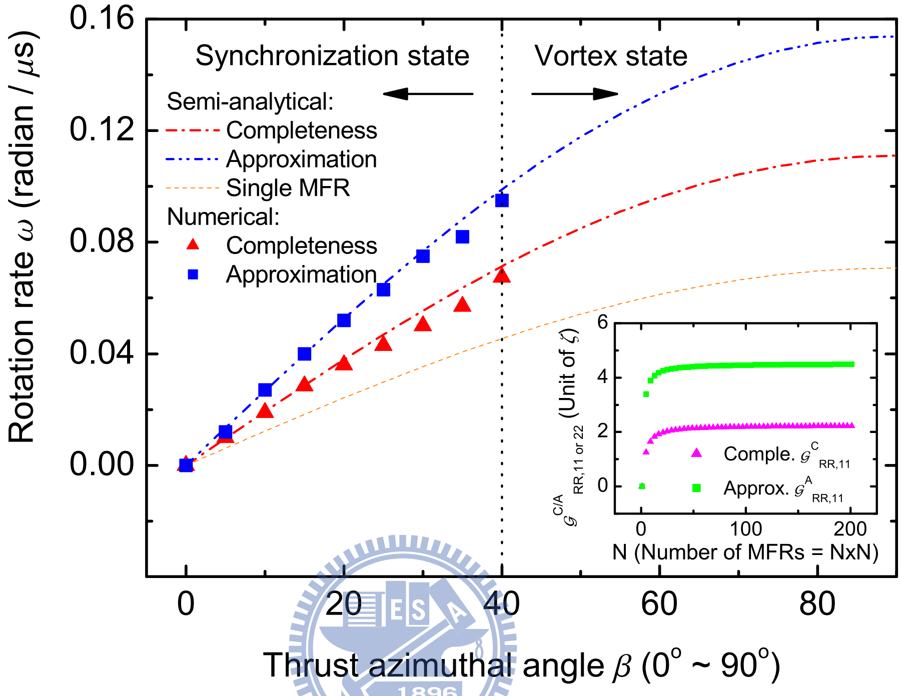

Figure 6.2: Plot of rotation rate ω versus the thrust azimuthal angle β for the case of a studied MFR matrix stays in the synchronization state. The red dash-doted and blue dash-dot-doted curves denote the semi-analytical calculation results which are plotted from equations (6.2) and (6.3) by applying both G^C (equations (5.3) and (5.4)) and G^A (equation (5.5)). The numerical calculation result of $\mathcal{G}_{RR}^{C/A}$ in equation (6.3) is shown in the inset, where the magenta triangle and green square symbols denote $\mathcal{G}_{RR}^{C}$ and $\mathcal{G}_{RR}^{A}$, respectively. The orange doted curve shown in the main plot is also plotted from equation (6.2), but we ignore the contribution of $\zeta\mathcal{G}_{RR,11}$ (equation (6.3)). It is just right the $\omega_0(t)$ shown in equation (6.4). The red triangle and blue square symbols are the numerical calculation results by utilizing both $G^{C/A}$, respectively. Due to the study of such MFR matrix system here, we numerically find that there seems to exist a universal critical azimuthal angle $\beta \approx 40°$. The synchronization state can be established stably when $\beta < 40°$, but once $\beta > 40°$ the MFR matrix should enter into vortex or random phase state.

on the circuit that connects the two different states.

To realize the effect that comes from other members, the member i is excluded, in a studied MFR matrix. We define an indicator

$$\chi \ = \ \frac{\omega_i(t)}{\omega_0(t)} = \frac{\frac{1}{\gamma} + \zeta \mathcal{G}_{RR,11}}{\frac{1}{\gamma}}, \tag{6.4}$$

to reveal such effect. The rotation rate $\omega_0(t)$ is just comes from the single MFR itself, but the speeded-up $\omega_i(t)$ is contributed from both the member i itself and other synchronized members in the studied MFR matrix. Applying the standard parameter set, utilized in Figure 6.2, we obtain $\chi \approx 1.57$ and $\chi \approx 2.18$ in the cases of G^C and G^A for all β, respectively. χ offers a very profound hint to explain the onset of a possible synchronization status in a microorganism cluster. According to the torque-speed relationship [1], the speeded-up $\omega_i(t)$ for member i implies that a larger thrust and consequently a larger flow field can be created from this speeded-up effect. From the following two points of view, (1) larger flow field that produced from MFR rotation, can be relatively equivalent to a smaller thermal fluctuation and (2) larger flow field seems to able to redistribute the thrust $\mathbf{F}_{\mathrm{th}}$ components, that is, larger flow field seems to be able to shrink the azimuthal angle β. Base on smaller thermal fluctuation extends the upper bond of β, that the synchronization state can exist stably when β smaller this upper bond, and small β benefits to the synchronization state exists stably [2]. The onset of a possible synchronization state in an MFR matrix can be attributed to the increase of χ. The recent experiments [3] offers a test bed to judge this scenario. And our theoretical and numerical approaches seems to give a reasonable explanation and consistent prediction to these experiments.

6.2.3 Repellency and freezing states in a checkerboard-like MFR matrix

Let us apply equation (5.7) and give the condition $\beta_p = \beta$ and $\beta_n = -\beta$ where members n are the nearest neighbors of members p. The two different kinds of member sets p and n form a checkerboard-like configuration in a studied MFR matrix. The system configuration is shown in Figures 5.1 (a) and 5.1 (c). Assume this studied MFR matrix enters into repellency state, then equation (5.7) can be simplified as

$$
\begin{aligned}
&\omega_{p/n}(t)\\
\approx\;& (+/-)\frac{1}{r}\\
&\left(\begin{array}{c}\frac{1}{\gamma}\mathbf{F}_{\text{th},p/n}\\ +\left\{\sum_{j=1,j\in p/n,j\neq p/n}^{(N\times N)/2} G(\mathbf{x}_j,\mathbf{x}_{p/n})\right\}\mathbf{F}_{\text{th},j}\\ +\left\{\sum_{j=1,j\in n/p}^{(N\times N)/2} G(\mathbf{x}_j,\mathbf{x}_{p/n})\right\}\mathbf{F}_{\text{th},j}\end{array}\right)\cdot\mathbf{e}_{t,p/n}\\
\approx\;& (+/-)\frac{1}{r}\left(\begin{array}{c}\frac{1}{\gamma}\mathbf{F}_{\text{th},p/n}\\ +\zeta\mathcal{H}^{Cr}_{RR}\mathbf{F}_{\text{th},p/n}\\ +\zeta\mathcal{H}^{St}_{RR}\mathbf{F}_{\text{th},n/p}\end{array}\right)\cdot\mathbf{e}_{t,p/n}\\
\approx\;& (+/-)\frac{1}{r}\mathrm{F}_{\text{th}}\sin\alpha\\
&\left(\begin{array}{c}\frac{1}{\gamma}\sin\beta\\ +\zeta\left\{\mathcal{H}^{Cr}_{RR,11}\sin\beta-\mathcal{H}^{St}_{RR,11}\sin(\Delta\phi+\beta)\right\}\end{array}\right),
\end{aligned}
\tag{6.5}
$$

where $\Delta\phi = \phi_p - \phi_n$. Here we define two tensors $\mathcal{H}^{St}_{RR}$ and $\mathcal{H}^{Cr}_{RR}$. Base on the numerical calculation analysis, the two tensors have the following characteristics

$$
\left\{\begin{array}{l}\mathcal{H}^{C,St}_{RR}\approx\mathcal{H}^{C,Cr}_{RR};\quad \mathcal{H}^{C,St}_{RR}+\mathcal{H}^{C,Cr}_{RR}\approx\mathcal{G}^{C}_{RR}\\ \mathcal{H}^{A,St}_{RR}\approx 2\mathcal{H}^{A,Cr}_{RR};\quad \mathcal{H}^{A,St}_{RR}+\mathcal{H}^{A,Cr}_{RR}\approx\mathcal{G}^{A}_{RR}.\end{array}\right.
\tag{6.6}
$$

Since these tensors $\mathcal{H}^{C/A,St \text{ or } Cr}_{RR}$ are related to tensors $\mathcal{G}^{C/A}_{RR}$ shown in equation (6.3). The characteristics of these tensors are similar to the one of the tensors $\mathcal{G}^{C/A}_{RR}$, and can be realized by referred to the statement about the tensors $\mathcal{G}^{C/A}_{RR}$.

Utilize equations (6.5) and (6.6), we can plot the semi-analytical calculation results of $\omega_{p/n}$. As the notice mentioned in the subsection Synchronization state in MFR matrix shown above, the rotation rates $\omega_{p/n}$ plotted in Figure 6.3 by applying G^C and in Figure 6.4 by using G^A is just a representative value. It is right the calculation result for the member p/n located at around the center region of the studied MFR matrix. Due to the loss of the symmetric property for a finite members MFR matrix, some deviation should appear for the member p/n which located near around the marginal region. Figures 6.3 and 6.4 also depict the numerical calculation results of $\omega_{p/n}$ with the standard parameter set $[H, b, N\times N, h, d, r, a, \mathrm{F}_{\text{th}}, \alpha, \beta] = [\times, \times, 50\times 50, 10, 15, 5, 1, 10, 90^\circ, 15^\circ \sim 60^\circ]$

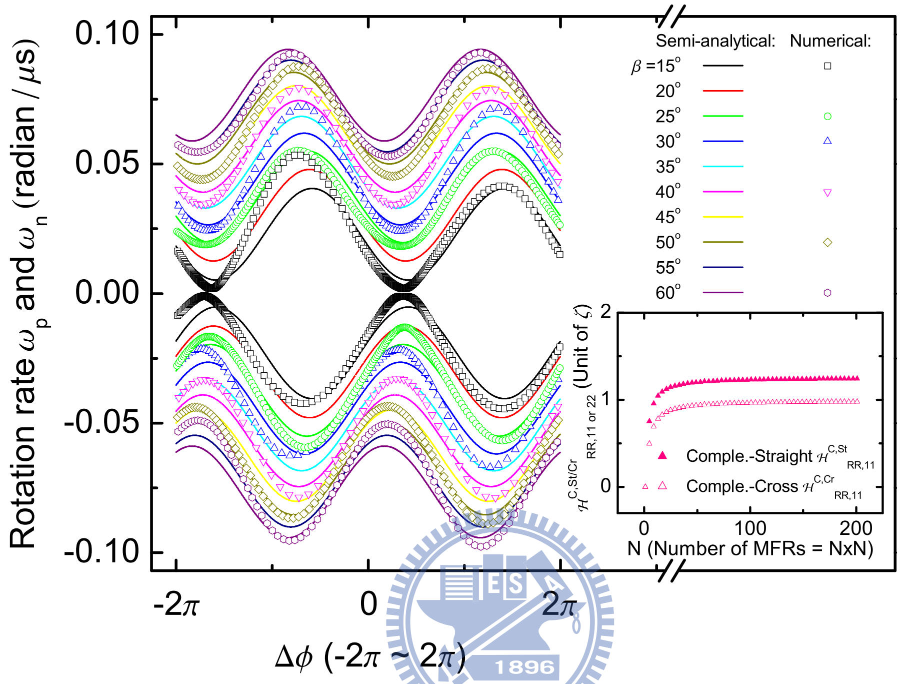

Figure 6.3: Plot of rotation rates ω_p (upper set) and ω_n (lower set) versus $\Delta\phi$ ($= \phi_p - \phi_n$) for the case of a studied MFR matrix stays in the repellency and freezing states. The various colored curves denote the semi-analytical calculation results corresponding to the thrust azimuthal angle $\beta = 15^\circ \sim 60^\circ$, which are plotted from equations (6.5) and (6.6) by applying G^C (equations (5.3) and (5.4)). The numerical calculation results of $\mathcal{H}^{C,St}_{RR}$ and $\mathcal{H}^{C,Cr}_{RR}$ in equation (6.6) are shown in the inset, where the pink filled triangle and pink blank triangle symbols denote $\mathcal{H}^{C,St}_{RR}$ and $\mathcal{H}^{C,Cr}_{RR}$, respectively. The various colored symbols are the numerical calculation results corresponding to some chosen β ranged between $15^\circ \sim 60^\circ$ by employing G^C (equations (5.3) and (5.4)). In the studied MFR matrix system here, we find numerically the repellency state can be established stably when β lay about in the range $15^\circ \sim 60^\circ$. Once $\beta < 15^\circ$ ($\beta > 60^\circ$) this MFR matrix should enter into freezing state (vortex or random phase state).

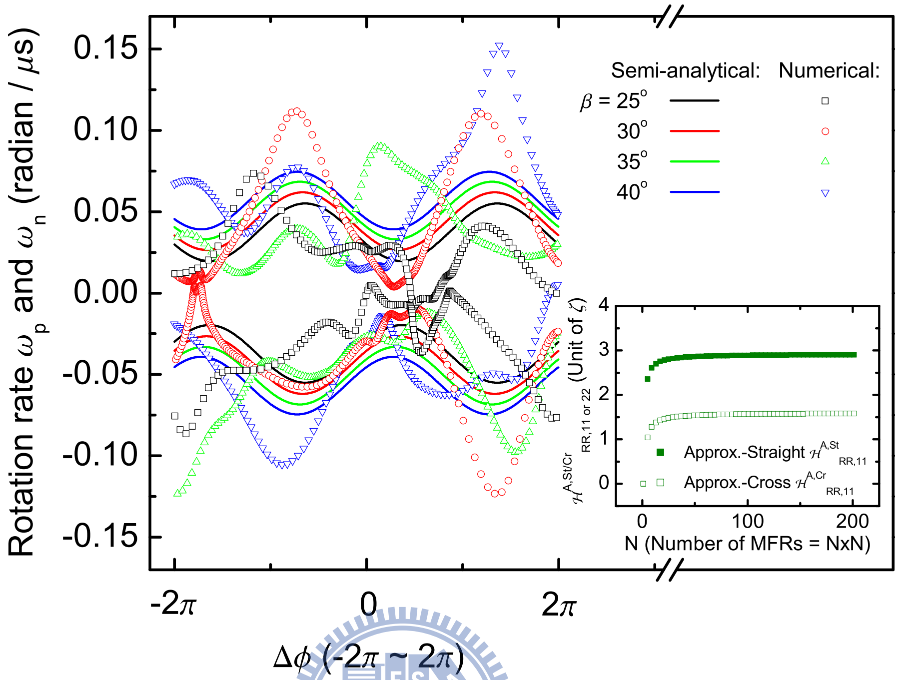

Figure 6.4: Plot of rotation rates ω_p (upper set) and ω_n (lower set) versus $\Delta\phi$ ($= \phi_p - \phi_n$) for the case of a studied MFR matrix stays in the repellency and freezing states. The various colored curves denote the semi-analytical calculation results corresponding to the thrust azimuthal angle $\beta = 25° \sim 40°$, which are plotted from equations (6.5) and (6.6) by applying G^A (equation (5.5)). The numerical calculation results of $\mathcal{H}^{A,St}_{RR}$ and $\mathcal{H}^{A,Cr}_{RR}$ in equation (6.6) are shown in the inset, where the olive filled square and olive blank square symbols denote $\mathcal{H}^{A,St}_{RR}$ and $\mathcal{H}^{A,Cr}_{RR}$, respectively. The various colored symbols are the numerical calculation results corresponding to some chosen β ranged between $25° \sim 40°$ by exploiting G^A (equation (5.5)). When applying G^A (equation (5.5)) to calculate ω_p and ω_n (equations (6.5) and (6.6)), we find an interesting phenomenon. Because that the G^A (equation (5.5)) loses its accuracy in the near field situation, the numerical calculation results reflect such property of G^A. Although the numerical calculation results try to follow the prediction of the semi-analytical calculation, anyhow an obvious distortion appearing and the range of β, which the repellency state is still remained somewhat stably, is shrank about into $25° \sim 40°$. Once $\beta < 25°$ ($\beta > 40°$) this MFR matrix should enter into freezing state (vortex or random phase state).

specified for the studied MFR matrix configuration. Interestingly, in the case of G^C shown in the Figure 6.3, the semi-analytical and numerical calculation results are so consistent in the region $\beta = 15^\circ \sim 60^\circ$. But, an obvious deviation appears between the semi-analytical and numerical calculation results for the case of G^A shown in Figure 6.4. The secret embedded in this phenomenon comes from the usage of G^A. The suitable situation of employing G^A is when we consider and concern the far field phenomena. G^A overvalues and distorts the flow field in near field. It has to be very careful in theoretical deduction and numerical calculation when one applies the G^A.

Our study in the repellency state in MFR matrix here shows us some new findings which do not appear in the case of the synchronization state in MFR matrix as discussed in the previous subsection. One of them is that when the azimuthal angle $\beta \leq 15^\circ$, a new state appears. We name it as freezing state. Such naming is for catching the characteristics of zero rotation rate tendency in each MFR member. It comes from the equal competition strengths between the two oppositely rotated tendency MFR member sets p and n. It is an unstable state, can be easily destroyed by some surrounding fluctuation, for example, the thermal fluctuation. Verification of this freezing state is an attractive thing in future experimental study. Another new finding is the upper bound of the azimuthal angle β can be extended up to $\beta \approx 60^\circ$. When $\beta \leq 60^\circ$ the repellency state in the checkerboard-like configuration of MFR matrix still can remain stably. We guess the reasons are due to in a checkerboard-like configuration of MFR matrix, the member belongs to member set p and the member belongs to member set n feel a weakened BOT hydrodynamic interaction each other. So that a stable repellency state still can survive even though the azimuthal angle β has reached about 60°.

6.3 Tracer particle responses on an MFR matrix

As usually seen in microscopic scale manipulation, the behavior of a system can be detected and revealed from the response of some trackers. A prominent example is the optical tweezers-microsphere assay, which is employed to explore the microorganism flagellum behavior. To unravel the flagellum behavior, we offer a direct mapping between the tracer particle responses and the microorganism flagellum matrix behavior. The tracer particle exhibits nontrivial behaviors in response to various subtle types of behaviors of the microorganism matrix. We discovered three response modes, tried to apply them to account for the recently found experimental outcomes, and use them as a guidance for designing new experiments for future studies.

6.3.1 Circular motion mode

Suppose a tracer particle is trapped at around the position $\mathbf{x} = \langle x, y, H \rangle$, by applying the hydrodynamic interaction BOT G and our MFR matrix model, the flow field acting on this tracer particle can be cast as shown in equation (5.9). Consider the case that this underlay MFR matrix stays in the synchronization state. The equation (5.9) then can be simplified as

$$\begin{aligned} \mathbf{u}(t) &\approx \left\{ \sum_{j=1}^{N\times N} G(\mathbf{x}_j, \mathbf{x}) \right\} \mathbf{F}_{\text{th}} \\ &= \zeta \mathcal{G}_{RP} \mathbf{F}_{\text{th}}. \end{aligned} \tag{6.7}$$

Base on the numerical calculation analysis, we define

$$\begin{aligned} \zeta \mathcal{G}_{RP}^{C/A} &= \left\{ \sum_{j=1}^{N\times N} G^{C/A}(\mathbf{x}_j, \mathbf{x}) \right\} \\ &\approx \zeta \begin{pmatrix} \mathcal{G}_{RP,11}^{C/A} & & 0 \\ & \mathcal{G}_{RP,22}^{C/A} & \\ 0 & & \mathcal{G}_{RP,33}^{C/A} \end{pmatrix} \\ &\approx \zeta \mathcal{G}_{RP,11}^{C/A} \begin{pmatrix} 1 & & 0 \\ & 1 & \\ 0 & & \delta_{RP,CM}^{C/A} \end{pmatrix}, \end{aligned} \tag{6.8}$$

where $\delta_{RP,CM}^{C} \approx 1$ for small $N \times N$ but $\delta_{RP,CM}^{C} \approx 0$ for large $N \times N$, and $\delta_{RP,CM}^{A} = 0$ for all $N \times N$, and $\zeta = \frac{3}{2\pi\eta}\frac{h^2}{d^3}$ is a normalized unit which is related to the leading behavior of G^C. Look into deeply the equation (6.8), we find $\mathcal{G}_{RP}$ is just like a function of variables H, h, d, r and N. We can treat $\mathcal{G}_{RP}$ as a pure geometry function determined only by the tracer particle combined MFR matrix configuration. The characteristics of this tensor $\mathcal{G}_{RP}^{C/A}$ is almost similar to the one of the tensor $\mathcal{G}_{RR}^{C/A}$ discussed in section 6.2.2.

Substitute equation (6.8) into equation (6.7) we get

$$\mathbf{u}(t) \quad \approx \quad \zeta \mathcal{G}^{C/A}_{RP,11} \mathrm{F}_{\mathrm{th}} \begin{pmatrix} \sin\alpha \cos\left(\beta+\phi\right) \\ \sin\alpha \sin\left(\beta+\phi\right) \\ \delta^{C/A}_{RP,CM} \cos\alpha \end{pmatrix}, \tag{6.9}$$

note that here in fact $\frac{d\phi}{dt} = \omega_i(t)$ as shown in equation (6.2). We decompose $\mathbf{u}(t)$ into $\mathbf{u}_{xy}(t)$ and $\mathbf{u}_z(t)$, it then gives the form

$$\begin{cases} \mathrm{u}_{xy} = \zeta \mathcal{G}^{C/A}_{RP,11} \mathrm{F}_{\mathrm{th},xy} \text{ and } \left\langle \mathbf{u}_{xy}(t) \right\rangle_{\phi \text{ or } t} = 0 \\ \mathrm{u}_z = \left\langle \mathbf{u}(t) \right\rangle_{\phi \text{ or } t} = \zeta \mathcal{G}^{C/A}_{RP,33} \mathrm{F}_{\mathrm{th},z}, \end{cases} \tag{6.10}$$

where $\mathrm{F}_{\mathrm{th},xy} = \mathrm{F}_{\mathrm{th}} \sin\alpha$, $\mathrm{F}_{\mathrm{th},z} = \mathrm{F}_{\mathrm{th}} \cos\alpha$, and $\langle \cdots \rangle_{\phi \text{ or } t}$ denotes the ϕ or t average.

In the low Reynolds number environment according to the Stokes' law, the flow field acting on the tracer particle can be equivalently treated as existing a drag force imposing on it. So equations (6.9) and (6.10) show us that the tracer particle should exhibit a 3-dimensional (3D) cone-shrinking-like ($\alpha < \frac{\pi}{2}$) or cone-expanding-like ($\alpha > \frac{\pi}{2}$) helical trajectory as time goes on; or a 2-dimensional (2D), on xy plane, circular ($\alpha = \frac{\pi}{2}$) trajectory. We name these 3D helical or 2D circular trajectories as Circular motion (CM) mode.

The radius of this 2D circular motion trajectory can be easily calculated

$$R_{CM} = \frac{\mathrm{u}_{xy}}{\omega_i(t)}. \tag{6.11}$$

Since $\omega_i(t) \propto \sin\beta$, according to equation (6.2), we find R_{CM} with such characteristics $R_{CM} \propto \csc\beta$. Figure 6.5 shows the semi-analytical and numerical calculation results for the 2D circular motion trajectory case by employing the standard parameter set $[H, b, N \times N, h, d, r, a, \mathrm{F}_{\mathrm{th}}, \alpha, \beta] = [20/40, 1, 50 \times 50, 10, 15, 5, 1, 10, 90°, 15° \sim 60°]$ specified for the studied tracer particle and MFR matrix combined configuration. A so consistent outcome calculated from both approaches above is observed in Figure 6.5.

Note that sometimes in real experimental situation, for instance, in the performing an optical tweezers microsphere assay, limited by the sampling frequency resolution of the observation equipments, says order 1 (Hz). The recorded data for this tracer particle response is a time average outcome. Because the rotation rate of the microorganism flagellum is usually lay in the order 10^2 or 10^3 (Hz), compare

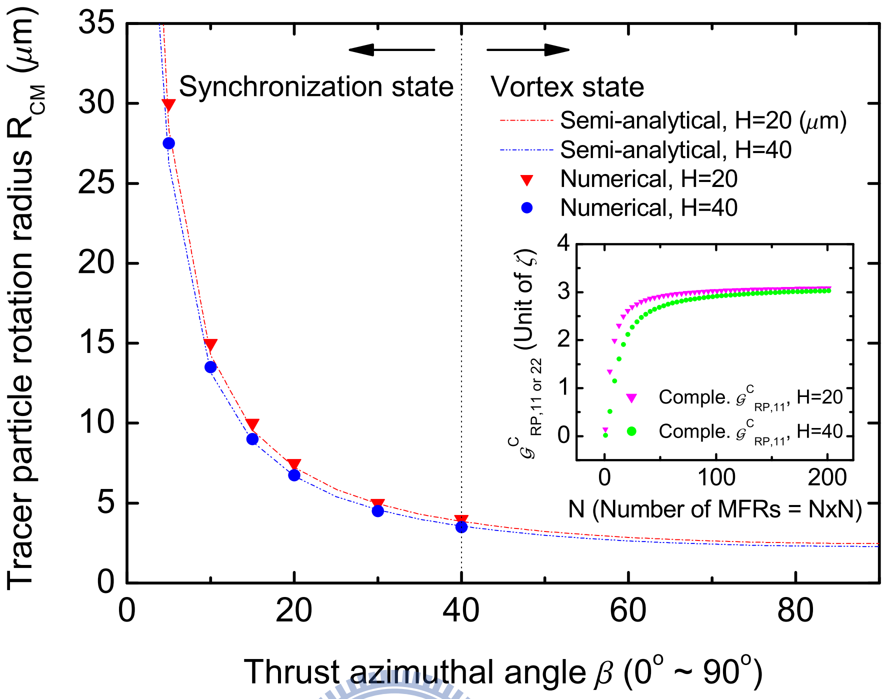

Figure 6.5: Plot of tracer particle rotation radius R_{CM} versus thrust azimuthal angle β for the case of circular motion mode. The red dash-doted and blue dash-dot-doted curves denote the semi-analytical calculation results corresponding to the tracer particle located at $H = 20$ and $H = 40$ (μm), respectively. They are calculated from equation (6.11). The numerical calculation results of $\mathcal{G}^C_{RP}$ for both $H = 20$ and $H = 40$ (μm) in expression (6.8) is shown in the inset, where the magenta reverse-triangle and green circle symbols denote $\mathcal{G}^C_{RP}$ for both $H = 20$ and $H = 40$ (μm), respectively. The red reverse-triangle and blue circle symbols are the numerical calculation results corresponding to some chosen β ranged between $5^\circ \sim 40^\circ$ by using G^C (equations (5.3) and (5.4)). In this plot, we find some interesting phenomena. One of them is, the tracer particle located height H seems not to give a significant effect on R_{CM}. This phenomenon can be realized by inspecting the inset of this plot. We observe that when $N = 50$ (our calculation standard employment), the difference of $\mathcal{G}^C_{RP,11}$ in both $H = 20$ and $H = 40$ (μm) cases is small. The second is, from Figure 3 we find the rotation rate $\omega(t) \to 0$ when $\beta \to 0$. So inserting it into equation (6.11), we get $R_{CM} \to \infty$. A singularity point $\beta = 0$ and the corresponding strange phenomenon $R_{CM} = \infty$ are found in this plot. The reasonable physical picture should give us that $R_{CM} = 0$ when $\beta = 0$. This strange phenomenon is nothing but just comes from the calculation strategy (or assumption) exploited in our MFR matrix model as mentioned in Chapter 5.2.

this with the sampling frequency which lay in the order 1 (Hz), the plane components $\mathbf{e}_x$ and $\mathbf{e}_y$ of the flow field should be washed out. Recently, the group [3] performed an experiment which shows that (1) an attractive (or repulsive) force F_z acting on the tracer particle that located at height H (measured from a bacterial carpet stuck substrate surface) with the trend $\mathrm{F}_z \propto H^{-3}$ (2) there are no forces can be detected in the plane components $\mathbf{e}_x$ and $\mathbf{e}_y$ direction from the optical microsphere assay. These phenomena can be explained easily from our circular motion mode viewpoint. We find that an MFR matrix with members about the order 10, the trend $\mathrm{F}_z \propto H^{-3}$ can be reappeared by calculated from equation (6.10). Besides, equations (6.9) and (6.10) reply the question why the measured drag force can be detected only in $\mathbf{e}_z$ component.

6.3.2 Linear oscillation mode

Suppose a tracer particle is trapped at around the position $\mathbf{x} = \langle x, y, H \rangle$, by applying the hydrodynamic interaction BOT G and our MFR matrix model, the flow field acting on this tracer particle can be casted as shown in equation (5.9). Consider the case of this MFR matrix stays in the repellency and freezing states. The equation (5.9) then can be simplified as

$$\begin{aligned} \mathbf{u}(t) &\approx \left\{ \sum_{j=1, j\in p}^{(N\times N)/2} G(\mathbf{x}_j, \mathbf{x}) \right\} \mathbf{F}_{\mathrm{th},p} \\ &+ \left\{ \sum_{j=1, j\in n}^{(N\times N)/2} G(\mathbf{x}_j, \mathbf{x}) \right\} \mathbf{F}_{\mathrm{th},n} \\ &\approx \zeta \mathcal{I}_{RP} \left\{ \mathbf{F}_{\mathrm{th},p} + \mathbf{F}_{\mathrm{th},n} \right\}. \end{aligned} \tag{6.12}$$

Due to the symmetry characteristics between $\left\{\sum_{j=1,j\in p}^{(N\times N)/2} G(\mathbf{x}_j, \mathbf{x})\right\}$ and $\left\{\sum_{j=1,j\in n}^{(N\times N)/2} G(\mathbf{x}_j, \mathbf{x})\right\}$ viewed from the tracer particle itself , we assume

$$\begin{aligned} &\zeta \mathcal{I}_{RP} \\ \approx\ & \left\{ \sum_{j=1, j\in p}^{(N\times N)/2} G(\mathbf{x}_j, \mathbf{x}) \right\} \approx \left\{ \sum_{j=1, j\in n}^{(N\times N)/2} G(\mathbf{x}_j, \mathbf{x}) \right\} \\ \approx\ & \frac{1}{2} \left\{ \sum_{j=1}^{N\times N} G(\mathbf{x}_j, \mathbf{x}) \right\}. \end{aligned} \tag{6.13}$$

In addition base on the numerical calculation analysis, we define

$$\begin{aligned}
\zeta\mathcal{I}_{RP}^{C/A} &\approx \left\{\sum_{j=1, j\in p \text{ or } n}^{(N\times N)/2} G^{C/A}(\mathbf{x}_j,\mathbf{x})\right\} \\
&\approx \zeta\begin{pmatrix} \mathcal{I}_{RP,11}^{C/A} & & 0 \\ & \mathcal{I}_{RP,22}^{C/A} & \\ 0 & & \mathcal{I}_{RP,33}^{C/A} \end{pmatrix} \\
&\approx \zeta\mathcal{I}_{RP,11}^{C/A}\begin{pmatrix} 1 & & 0 \\ & 1 & \\ 0 & & \delta_{RP,LO}^{C/A} \end{pmatrix},
\end{aligned} \tag{6.14}$$

where $\delta_{RP,LO}^{C} \approx 1$ for small $N\times N$ but $\delta_{RP,LO}^{C} \approx 0$ for large $N\times N$, and $\delta_{RP,LO}^{A} = 0$ for all $N\times N$, and $\zeta = \frac{3}{2\pi\eta}\frac{h^2}{d^3}$ is a normalized unit which related to the leading behavior of G^C. Look into deeply the equation (6.14), we find $\mathcal{I}_{RP}$ is just like a function of variables H, h, d, r and N. We can treat $\mathcal{I}_{RP}$ as a pure geometry function determined only by the tracer particle and MFR matrix combined configuration. The characteristics of the tensors $\mathcal{I}_{RP}^{C/A}$ shown above is similar to the tensors $\mathcal{H}_{RR}^{C/A,St \text{ or } Cr}$ shown in equation (6.6) of section 6.2.3.

Substitute equation (6.14) into equation (6.12), we get

$$\begin{aligned}
&\mathbf{u}(t) \\
\approx\ & \zeta\mathcal{I}_{RP,11}^{C/A}\mathrm{F}_{\mathrm{th}} \\
&\left\{\begin{pmatrix} \sin\alpha\cos(\beta+\phi_p) \\ \sin\alpha\sin(\beta+\phi_p) \\ \delta_{RP,LO}^{C/A}\cos\alpha \end{pmatrix} + \begin{pmatrix} \sin\alpha\cos(-\beta+\phi_n) \\ \sin\alpha\sin(-\beta+\phi_n) \\ \delta_{RP,LO}^{C/A}\cos\alpha \end{pmatrix}\right\} \\
\approx\ & \zeta\mathcal{I}_{RP,11}^{C/A}\mathrm{F}_{\mathrm{th}} \\
&\left\{\begin{pmatrix} \sin\alpha\cos(\beta+\phi) \\ \sin\alpha\sin(\beta+\phi) \\ \delta_{RP,LO}^{C/A}\cos\alpha \end{pmatrix} + \begin{pmatrix} \sin\alpha\cos(-\beta-\phi) \\ \sin\alpha\sin(-\beta-\phi) \\ \delta_{RP,LO}^{C/A}\cos\alpha \end{pmatrix}\right\} \\
=\ & \zeta\mathcal{I}_{RP,11}^{C/A}2\mathrm{F}_{\mathrm{th}}\begin{pmatrix} \sin\alpha\cos(\beta+\phi) \\ 0 \\ \delta_{RP,LO}^{C/A}\cos\alpha \end{pmatrix},
\end{aligned} \tag{6.15}$$

here note that in fact $\frac{d\phi_{p/n}}{dt} = \omega_{p/n}(t)$ as shown in equation (6.5), and $\phi = \phi_p = -\phi_n$

is set. We decompose $\mathbf{u}(t)$ into $\mathbf{u}_{xy}(t)$ and $\mathbf{u}_z(t)$, it then gives the form

$$\begin{cases} \mathrm{u}_{xy} = \zeta \mathcal{I}^{C/A}_{RP,11} 2\mathrm{F}_{\mathrm{th},xy} \cos\left(\beta+\phi\right) \\ \mathrm{u}_z = \langle \mathbf{u}(t) \rangle_{\phi \text{ or } t} = \zeta \mathcal{I}^{C/A}_{RP,33} 2\mathrm{F}_{\mathrm{th},z}, \end{cases} \tag{6.16}$$

where $\mathrm{F}_{\mathrm{th},xy} = \mathrm{F}_{\mathrm{th}} \sin\alpha$, $\mathrm{F}_{\mathrm{th},z} = \mathrm{F}_{\mathrm{th}} \cos\alpha$, and $\langle \cdots \rangle_{\phi \text{ or } t}$ denotes the ϕ or t average.

.

In the low Reynolds number environment according to the Stokes' law, the flow field acting on the tracer particle can be equivalently treated as existing a drag force imposing on it. So equations (6.15) and (6.16) show us that the tracer particle should exhibit a 3-dimensional (3D), in fact it is just lay on a 2-dimensional (2D) xz plane, cone-shrinking-like ($\alpha < \frac{\pi}{2}$) or cone-expanding-like ($\alpha > \frac{\pi}{2}$) zigzag oscillation trajectory; or a 2-dimensional (2D), on xy plane, linear oscillation ($\alpha = \frac{\pi}{2}$) trajectory. We name these 3D zigzag or 2D linear trajectories as Linear oscillation (LO) mode.

In the 2D linear oscillation trajectory case ($\alpha = \frac{\pi}{2}$), the maximal displacement L_{LO} of the tracer particle can be calculated by integrating its $\mathbf{u}(t)$ spanned one fourth of oscillation period T

$$\begin{aligned} L_{LO} &\approx 2\int_0^{\frac{T}{4}} |\mathbf{u}(t)| dt \\ &\approx 2\zeta \mathcal{I}^{C/A}_{RP,11} 2\mathrm{F}_{\mathrm{th},xy} \\ &\quad \int_{\beta+\phi=0}^{\beta+\phi=\frac{\pi}{2}} \frac{1}{\omega_{p/n}(t)} \cos\left(\beta+\phi\right) d\left(\beta+\phi\right) \\ &\approx 2\zeta \mathcal{I}^{C/A}_{RP,11} 2\mathrm{F}_{\mathrm{th},xy} \left\langle \omega_{p/n}(t) \right\rangle^{-1}_{\phi \text{ or } t}. \end{aligned} \tag{6.17}$$

If we approximate $\left\langle \omega_{p/n}(t) \right\rangle_{\phi \text{ or } t} \propto \sin\beta$, according to equation (6.5), L_{LO} reveals us the characteristics $L_{LO} \propto \csc\beta$. Figure 6.6 shows the semi-analytical and numerical calculation results for the 2D linear oscillation trajectory case by applying the standard parameter set $[H, b, N \times N, h, d, r, a, \mathrm{F}_{\mathrm{th}}, \alpha, \beta] = [20/40, 1, 50 \times 50, 10, 15, 5, 1, 10, 90^\circ, 15^\circ \sim 60^\circ]$ specified for the studied tracer particle and MFR matrix combined configuration. In general, the two approaches give us a so consistent outcome. But, there is a little bit discrepancy appearing in the region of small β. The reasons maybe come from the competition characteristics embedded in the repellency state due to the underlay checkerboard-like configuration of MFR matrix. In the stronger competition situation, says small β region, tracer particle approaches to the freezing state regime. So that tracer particle can not move

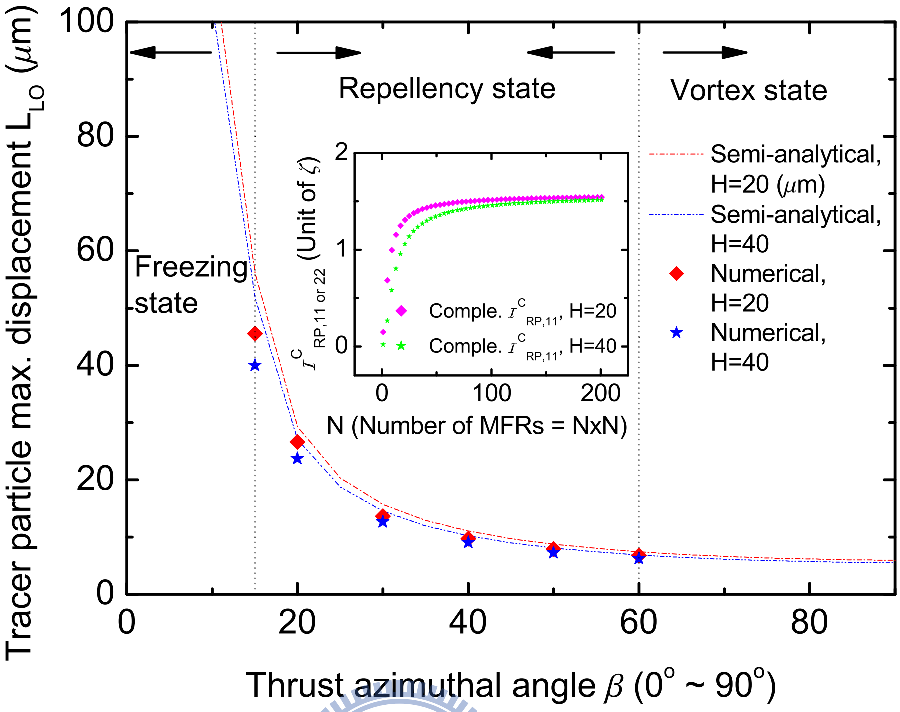

Figure 6.6: Plot of tracer particle maximal displacement L_{LO} versus thrust azimuthal angle β for the case of linear oscillation mode. The red dash-doted and blue dash-dot-doted curves denote the semi-analytical calculation results corresponding to the tracer particle located at $H = 20$ and $H = 40$ (μm), respectively. They are calculated from equation (6.17). The numerical calculation result of $\mathcal{I}^C_{RP}$ for both $H = 20$ and $H = 40$ (μm) in expression (6.14) is shown in the inset, where the magenta rhombus and green asterisk symbols denote $\mathcal{I}^C_{RP}$ for both $H = 20$ and $H = 40$ (μm), respectively. The red rhombus and blue asterisk symbols are the numerical calculation results corresponding to some chosen β ranged between $15° \sim 60°$ by using G^C (equations (5.3) and (5.4)). In this plot, we find some interesting phenomena. At first, the tracer particle located height H seems not to give an significant effect in L_{LO}. This phenomenon can be realized easily by inspecting the inset of this plot. We observe that when $N = 50$ (our calculation standard employment), the difference of $\mathcal{I}^C_{RP,11}$ in both $H = 20$ and $H = 40$ (μm) cases is small. The second is, the more obvious deviation appearing when $\beta \longrightarrow 15°$. The reasons maybe come from that when $\beta \rightarrow 15°$, the underlay MFR matrix approaches to the freezing state. We can image that when MRF approaches to the freezing state, the resultant u_{xy} (equation (6.16)) may be frozen at some position (possibly nearby $(\Delta\phi + \beta) \approx \frac{\pi}{2}$ as shown in equation (6.5) and the plots depicted in Figures 6.3 and 6.4) which gives a smaller magnitude than the average one that is taken when we perform the integral calculation (equation (6.17)).

freely and then gives us somewhat smaller displacement value than the expected outcome calculated from semi-analytical calculation.

6.3.3 Sharp jumping mode

The strategies that the microorganisms change their movement direction or stop movement are exploited by means of, says the tumble process or the sweep process. The tumble process is said the microorganisms change their flagella motors to run from counterclockwise (CCW) to clockwise (CW) and makes the flagella filaments work independently, then the microorganisms bodies move erratically with little net displacement [4]. The sweep process means that the microorganisms sweep abruptly their flagella filaments into a new direction, such that a thrust is accompanied during this sweep process and makes the orientation of these microorganisms bodies change [5].

Here we combine the sweep process function into our MFR matrix model. Although in this article the study is focus on the situation which the microorganisms bodies are fixed. The consideration of the sweep process is still able to offer some interesting and useful information to realize the microorganisms swimming and movement action. To try to precisely describe the sweep process, by taking the viewpoint of constructing a minimal parameter model, we propose a three characteristic parameters constituted sweep model , $\mathrm{MFR}_{\mathrm{sweep}}$, to represent the microorganism flagellum sweep press,

$$\begin{aligned}\mathrm{MFR}_{\mathrm{sweep}} &\equiv [\phi_{\mathrm{onset}}, \phi_{\mathrm{jump}}, \mathbf{F}_{\mathrm{sweep}}] \\ &\quad (\mathrm{degree\ or\ radian, pN}).\end{aligned}$$

ϕ_{onset} is a sweep onset indicator. When the microorganism flagellum rotation phase ϕ of some studied MFR member reaches ϕ_{onset}, ϕ is counted immediately when a sweep event happens, the microorganism flagellum sweep process is turned on. ϕ_{jump} is a sweep jumping or sweep shifting indicator. It is obvious that the role of ϕ_{jump} is like a bonus given to ϕ. Mathematically it means that $\phi|_{t=t} \rightarrow (\phi + \phi_{\mathrm{jump}})|_{t=t+\delta t}$, where δt is the sweep process action duration and we assume $\delta t \approx 0$. And $\mathbf{F}_{\mathrm{sweep}}$ indicates the sweep inducing thrust that can be spread by means of hydrodynamic interaction. $\mathbf{F}_{\mathrm{sweep}}$ is a vector that includes both strength $\mathrm{F}_{\mathrm{sweep}}$ and orientation $\mathbf{e}_n(\phi|_{t+\delta t} = \phi|_t + \phi_{\mathrm{jump}})$. The orientation $\mathbf{e}_n(\phi|_{t+\delta t} = \phi|_t + \phi_{\mathrm{jump}})$ is the normal component unit vector of the studied MFR, which is specified by time-dependent argument ($\phi|_t + \phi_{\text{jump}}$).

Once the reasonable parameter values are given to the sweep model $\text{MFR}_{\text{sweep}}$, the combined process that constituted by $\text{MFR}_{\text{matrix}}$ and $\text{MFR}_{\text{sweep}}$ models can be explored. In order to offer a clearer physical picture, we consider and illustrate the following case. Consider a tracer particle that located over an MFR matrix which originally stays in the synchronization state. Then by adding the sweep process function $\text{MFR}_{\text{sweep}}$ and varying these parameter values therein, we can see what happens on such tracer particle response trajectory. Figure 6.7 shows us this scenario by utilizing the parameter sets $\text{MFR}_{\text{matrix}} = [20, 1, 50 \times 50, 10, 15, 5, 1, 10, 90°, 20°]$ and $\text{MFR}_{\text{sweep}} = [2\pi, \pi, 10/100/500/1000)]$ for cases (a) $\sim$ (d), respectively. In all cases the calculation time step is set as 2 (μs), and the total calculation time period is 1200 (μs). Inspect Figure 6.7 in detail, we can find many interesting phenomena induced from $\text{MFR}_{\text{sweep}}$ model. The underlay MFR matrix behavior is affected by both thrust $\mathbf{F}_{\text{th}}$, always accompanied with each MFR member, and sweep induced thrust $\mathbf{F}_{\text{sweep}}$, added when the summation of phase ϕ of some studied MFR member reaches the onset value ϕ_{onset}. So by separating the effects of $\mathbf{F}_{\text{th}}$ (acting on the tracer particle) and $\mathbf{F}_{\text{sweep}}$ (acting on the tracer particle), the tracer particle behavior responded or mapped to the underlay MFR matrix action behavior can be realized more clearly.

In Figure 6.7, the blue, magenta, and green curves in each case (a) $\sim$ (d) are the tracer particle response trajectories that correspond to consider the hydrodynamic interaction BOT from thrust $\mathbf{F}_{\text{th}}$, sweep inducing thrust $\mathbf{F}_{\text{sweep}}$, and both of the thrust $\mathbf{F}_{\text{th}}$ and sweep inducing thrust $\mathbf{F}_{\text{sweep}}$, respectively. At first, let us compare the blue and green curves in cases (a) and (b). When a sweep event $\text{MFR}_{\text{sweep}}$ happened, the parameter ϕ_{jump} functions the MFR bead or the phase ϕ of almost all members in the studied MFR matrix to jump or shift synchronously to a new starting position. And concurrently the sweep inducing thrust $\mathbf{F}_{\text{sweep}}$ tends to jump or shift the tracer particle to a new position immediately. The tracer particle jumping displacement can be calculated easily

$$\begin{aligned}
\mathbf{L}_{SJ} &\approx \mathbf{u}(t)\Delta t \\
&= \left\{ \sum_{j=1}^{N\times N} G(\mathbf{x}_j, \mathbf{x}) \left(\mathbf{F}_{\text{th},j} + \mathbf{F}_{\text{sweep},j} \right) \right\} \Delta t \\
&\approx \left\{ \sum_{j=1}^{N\times N} G(\mathbf{x}_j, \mathbf{x}) \right\} \left(\mathbf{F}_{\text{th}} + \mathbf{F}_{\text{sweep}} \right) \Delta t \\
&= \zeta \mathcal{G}_{RP} \left(\mathbf{F}_{\text{th},j} + \mathbf{F}_{\text{sweep},j} \right) \Delta t, \qquad (6.18)
\end{aligned}$$

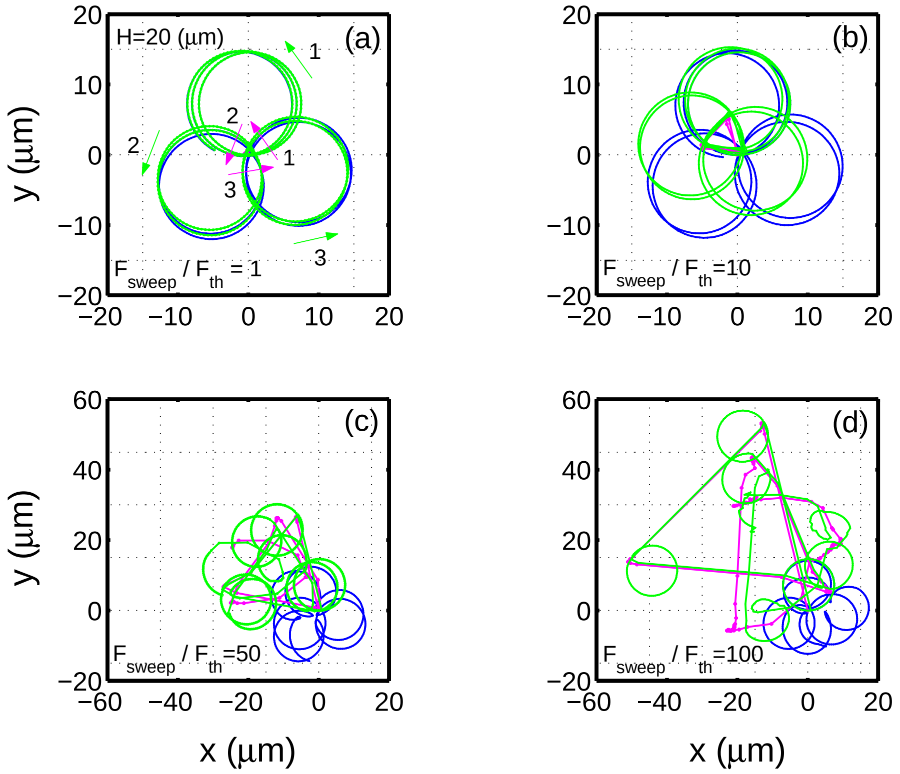

Figure 6.7: Plot of the tracer particle response trajectories. The tracer particle is located over an MFR matrix, which originally stays in the synchronization state. Here we concern the MFR$_{\mathrm{matrix}}$ and MFR$_{\mathrm{sweep}}$ combined process. (a) $\sim$ (d) show us the tracer particle response trajectories by exploiting the parameter sets MFR$_{\mathrm{matrix}}$ $= [20, 1, 50 \times 50, 10, 15, 5, 1, 10, 90°, 20°]$ and MFR$_{\mathrm{sweep}}$ $= [2\pi, \pi, 10/100/500/1000]$, respectively. In all cases the calculation time step is 2 (μs) and the total calculation time is 1200 (μs). In general, the green curve are the superposition of blue and magenta curves in all cases (a) $\sim$ (d). The tracer particle is originally located at $\langle 0, 0, 20\rangle$ (μm) and it undergoes about 7 circles based on the circular motion characteristics of CM mode, the measured $R_{CM} \approx 7.5$ μm coincides with the results shown in equation (6.11) and Figure 6.5. And in the numerical calculation, the initial phase ϕ for each member of the underlay MFR matrix is set $\phi = -20°$. Look into (a), the green (/magenta) arrows and the accompanied numbers tagged nearby them illustrate the first three circles, here for both green and blue ones, rotation orientation (/the first three sharp jumping displacements direction) and their corresponding appearance sequence. A very small magenta triangle-like curve with side length ≈ 0.55 (μm) depicts the corresponding first three sharp jumping displacements. Note that even though the strength of F$_{\mathrm{sweep}}$ is larger than F$_{\mathrm{th}}$ up to one order scale $\frac{\mathrm{F}_{\mathrm{sweep}}}{\mathrm{F}_{\mathrm{th}}} = \frac{0\sim100}{10}$, the underlay MFR matrix seems to still stay in the original synchronization status. Such phenomena are revealed in cases (a) and (b). Anyhow once we increase the strength of $\mathbf{F}_{\mathrm{sweep}}$ up to about two order scale, $\frac{\mathrm{F}_{\mathrm{sweep}}}{\mathrm{F}_{\mathrm{th}}} = \frac{500}{10}/\frac{1000}{10}$, larger than the strength of $\mathbf{F}_{\mathrm{th}}$, a very obvious distorted appearance is observed on the tracer particle response trajectories as shown in the blue, magenta and green curves of (c) and (d).

where $\zeta\mathcal{G}_{RP}$ can be obtained from equation (6.8) and the inset of Figure 6.5. For the 2D case

$$L_{SJ} \approx \mathrm{u}_{xy}\Delta t, \tag{6.19}$$

where u_{xy} is right the one appeared in equation (6.10), but $\mathrm{F}_{\mathrm{th},xy}$ has to be substituted by $(\mathbf{F}_{\mathrm{th}} + \mathbf{F}_{\mathrm{sweep}})_{xy}$ therein, and Δt is the numerical calculation time step, $\Delta t = 2$ (μs) used here. Apply equation (6.19) to calculate L_{SJ} for cases (a) $\sim$ (d), the outcomes are given about 0.55/5.5/27.5/55 (μm), respectively. The magenta curves depict the jumping displacement, the so consistent results can be found between equation (6.19) and cases (a) $\sim$ (d). The characteristics of the blue and green curves in cases (a) and (b) exhibits a CM mode. The measured $R_{CM} \approx 7.5$ μm coincides with the results shown in equation (6.11) and Figure 6.5, it implies that the underlay MFR matrix is still to stay in the synchronization state. Such profound finding reveals us, even though the strength of $\mathrm{F}_{\mathrm{sweep}}$ is larger than the strength of F_{th} up to one order scale $\frac{\mathrm{F}_{\mathrm{sweep}}}{\mathrm{F}_{\mathrm{th}}} = \frac{0\sim100}{10}$, the underlay MFR matrix seems to still stay in the original synchronization status. As time goes on, the tracer particle response trajectories, green curves in (a) and (b), exhibit jumping or shifting-like appearance. Here the reasons that produce the three circles-like main configuration are due to the assignment of $\phi_{\mathrm{onset}} = 2\pi$ such that a complete circle can be formed, and $\phi_{\mathrm{jump}} = \frac{2\pi}{3}$ so then an equilateral triangle like jumping is established as shown in the magenta curves of (a) and (b) (or even for all cases (a) $\sim$ (d)). Look into case (a), the arrows and the accompanied numbers tagged nearby the blue and green curves (green arrows)/magenta curves (very small triangle with side length ≈ 0.55 (μm), magenta arrows) illustrate the first three circles rotation orientation and their corresponding appearance sequence/first three sharp jumping displacements direction. In general, the green curve is the superposition of blue and magenta curves in all cases (a) $\sim$ (d). For such new and interesting phenomenon, indicated by blue or magenta or green curves, we name it as Sharp jumping (SJ) mode.

Turn to the cases (c) and (d), a very obvious distorted and/or jumping appearance in blue, magenta and green curves are observed. The sharp jumping effect which denoted by the ratio $\frac{\mathrm{F}_{\mathrm{sweep}}}{\mathrm{F}_{\mathrm{th}}}, \frac{\mathrm{F}_{\mathrm{sweep}}}{\mathrm{F}_{\mathrm{th}}} = \frac{500}{10}/\frac{1000}{10}$ in case (c)/(d), is too large to sustain the underlay MFR matrix to keep in the synchronization state stably. We have examined the time evolution of phase ϕ for each MFR member in the studied MFR matrix and verify the correctness of such opinion above. This phenomenon looks like reasonable and coincides with our intuition at first glance.

Larger fluctuation destroys the underlay MFR matrix stability and then pushes it into vortex or random phase state. But think about this phenomenon deeply, this stability breakdown is happened in the situation that the strength of $\mathbf{F}_{\mathrm{sweep}}$ up to almost two order scale larger than the strength of $\mathbf{F}_{\mathrm{th}}$. The two order scale magnitude for the ratio $\frac{\mathrm{F_{sweep}}}{\mathrm{F_{th}}}$ is seldom observed in real microorganisms. This is the position to make a short complement and summary about the study in SJ mode. The original state, says the synchronization or repellency sates, of the MFR matrix does not be destroyed by purely varying the parameters ϕ_{onset} and ϕ_{jump} ($\mathrm{MFR}_{\mathrm{sweep}} = [\phi_{\mathrm{onset}}, \phi_{\mathrm{jump}}, \times]$). The tracer particle trajectory still retains the original characteristics, says CM or LO modes, which is reflected by the underlay MFR matrix state. When the parameter $\mathbf{F}_{\mathrm{sweep}}$ is considered, and once the strength of $\mathbf{F}_{\mathrm{sweep}}$ beyond some threshold, the original state of the underlay MFR matrix should be destroyed and consequently map to an obvious distorted and jumping tracer particle trajectory.

Recent experiments [6] described the tracer particle that located over a bacterial carpet exhibits a sub-diffusion behavior. In order to inspect the bacterial flagella behavior in the underlay bacterial carpet, this group recorded the response of two beads, each bead is attached on a bacterial flagellum and these two bacteria are located nearby each other. Such experiments exhibit and imply a synchronized-like sweep behavior between these two adjacent bacteria. Base on these findings, this group suggests that a synchronization state maybe exist in a bacterium cluster with small members that located at the bacterial carpet. At first glance, such sub-diffusion behavior seems to violate our intuition. Because that an abrupt sweep process seems to enhance the fluid fluctuation and make the tracer particle to tend to a super-diffusion behavior. But if we assume the underlay bacterium carpet, or just need to assume the underlay bacterium cluster with small members, to stay in a synchronization state. Then from the viewpoint of sharp jumping mode, such sub-diffusion behavior can be explained reasonably. Since the strength of $\mathbf{F}_{\mathrm{sweep}}$ is just about one order scale larger than the strength of $\mathbf{F}_{\mathrm{th}}$ as measured and estimated from experiments [6], the underlay MFR matrix is still remained in the synchronization state and does not be destroyed by the sweep process. From Figure 6.7 (a) and (b), the tracer particle is still caged in a small region even though the sweep process is functioning and consequently a sub-diffusion behavior is observed.

6.4 Conclusion and outlook

The microorganism flagellum behavior is a fascinating phenomenon in the microscopic natural world. Trying to explore and realize such phenomenon is not just due to scientific curiosity, but because it also offers a potential in academic and industrial application. In this study, we propose two minimal models, the microorganism-flagellum-rotor matrix ($\mathrm{MFR}_{\mathrm{matrix}}$) and the microorganism-flagellum-rotors with sweep process ($\mathrm{MFR}_{\mathrm{sweep}}$), to get insight into these complex systems. By employing these two models, we explore the hydrodynamic interaction between flagella through the complete Blake-Oseen tensor G^C and the approximated Blake-Oseen tensor G^A, in the following systems: (1) 2 MFRs (2) $N \times N$ MFR matrix (3) a tracer particle over an $N \times N$ MFR matrix.

In issue (1), a phase portrait reveals the synchronization and repellency states, which can exist stably and correspond to the fixed points in the portrait. In issue (2), (a) the synchronization state can exist stably when the azimuthal angle β is smaller than some threshold, and (b) the repellency state can exist stably when the β lies within some range and concurrently freezing state can exist unstably in small β regime. In issue (3), our studies reveal that the tracer particle can exhibit (a) a circular motion (CM) mode, (b) a linear oscillation (LO) mode, and (c) a sharp jumping (SJ) mode. These studies provide some hints to understand several recent experimental findings. Firstly, our results supports the experimentally measured decay $\mathrm{F}_z \propto H^{-3}$ of the hydrodynamic drag force strength F_z along the distance H measured from the substrate surface of the bacterial carpet. Secondly, it seems to exist a rotation rate threshold which switches on the synchronized behavior in the underlay bacterial carpet. Thirdly, a tracer particle can exhibit a sub-diffusive behavior even though it locates over a bacterial carpet in which the flagella can sweep.

Although this article has presented a lot of phenomena in the microorganism flagellum matrix, there still exist many others waiting for exploring. For example, we have found some interesting and new modes in the tracer particle trajectory when the particle is located over an MFR matrix which stays in a vortex or random phase state. In the future, we should try to unravel more interesting phenomena about the microorganism flagellum matrix and carpet behavior, which includes thermal fluctuations. Although our original formalisms in equations (5.6) and (5.8) also include these fluctuations, their effects are neglected in this study. Certainly, it is a topic which can be included in the future discussion.

Bibliography

[1] Y. Sowa, H. Hotta, M. Homma and A. Ishijima J. Mol. Biol. **327**, 1043 (2003).

[2] N. Uchida and R. Golestanian, Phys. Rev. Lett. **104**, 178103 (2010).

[3] J.-H. Wang, Y.-T. Hsiao, J. Tsai, C.-H. Chang, C.-J. Lo and W. Y. Woon (unpublished private communication).

[4] H. C. Berg, Phys. Today **53**, 24 (2000).

[5] L. Xie, T. Altindal, S. Chattopadhyay and X.-L. Wu, Proc. Natl. Acad. Sci. **108**, 2246 (2011).

[6] Y.-T. Hsiao, J.-H. Wang, Y.-C. Hsu, C.-C. Chiu, C.-J. Lo, C.-W. Tsao and W. Y. Woon, Appl. Phys. Lett. **100**, 203702 (2012).

Chapter 7

Hydrodynamic Spreading of Forces from Bacterial Carpet

7.1 Introduction

The phenomena of collective motions in self-propelled particles (SPP) are ubiquitous in nature [1]. Under complex interplay between external driving and local interactions, the orientational and velocity correlation length in a SPP system can be several orders of magnitude larger than the individual characteristic dimension. The interaction between each SPP constantly competes with dissipation and random noises in the system. Presence of boundaries enforces constraints on available states and spreading of interactions. Rich phenomena are therefore expected when ratio between each competing terms are varied or boundary conditions are changed. From the viewpoint of statistical physics, SPP system provides an ideal test bed for non-equilibrium many-body physics [2].

Among all SPP systems, bacterium is probably the most thoroughly studied due to its biological importance [3]. The complexity of behaviors that come from these micro-organisms with such simple structures challenges our understanding in fluid dynamics and evolutionary biology [4]. Bacteria adapt to lives at low Reynolds number with their flagellar motors that possess near-perfect torque-speed relation [5]. For example, for a single polarly-flagellated bacterium, rotation of the filamental helical propeller in counterclockwise (CCW) or clockwise (CW) senses [6] exerts thrusts to the surrounding fluid environment and leads to forward or backward (defined by the orientation of cell body) swimming motions. In free space the force exerted from a swimming bacterium can be modeled as a force dipole under far field approximation and spread into the fluidic environment through hydrodynamic interactions with one r^{-2} dependence [7]. At close proximity to surface, the swimming behavior of bacterium has been found to alter dramatically due to complex interactions with boundaries [8,9,10], while the form of hydrodynamic spreading of force generated from the swimming bacterium is also changed [11]. The above effects are suggested to have significant impact on cell signaling and bio-film formation [9]. The rich phenomena arise from collective interactions between SPP and boundaries are interesting fluid dynamics issues to be explored.

On the other hand, collective flow patterns have been observed and theoretically predicted in fluidic environment near bacteria attached surfaces, namely bacterial carpets [12,13,14,15]. Under hydrodynamic interactions with the form of long ranged Blake-Oseen tensor (BOT), transition to synchronization of flagellar rotation can be found. Theoretically, synchronization requires phase lock between adjacent rotors. Thrusts from neighboring rotors are propagated to one another through the BOT. The accumulated thrusts lead to acceleration of phase changing rate and enable phase synchronization between rotors. Moreover, it was suggested that the modes of rotor motion could affect the degree of synchronization, in which normal component thrust is more favorable than the tangential counterpart. To date, no experimental examination of above statement has been conducted in any physical or biological systems. Furthermore, whether there exists a threshold in coupling strength above which onset of synchronization take place is still an open issue. On the other hand, the collective flow patterns have been suggested to be utilized in microfluidic devices for transport manipulation [16,17]. Studies on hydrodynamics near the bacterial carpets and manipulation of bacterial distribution near surface could help advancing our understanding in collective bacterial behaviors and present opportunities for microbial-fluid interface engineering that could boost microfluidic developments.

7.2 Experimental approaches and results

In this letter, we investigate hydrodynamics near bacterial carpets by piconewton force measurement with optical tweezers-microsphere assay. Single polarly-flagellated bacterium strains with tunable flagellar rotational rate are employed. Dense bacterial carpets with random cell orientation are formed by flow deposition of bacteria in microchannel. By conducting force measurements at varying heights above bacterial carpet, the forms of the hydrodynamic spread of forces are determined. An effective attractive (repulsive) force is detected at height ≤ 20 μm above bacterial carpets. We found that the collective force takes the form of force quadrupole or source doublet like behavior. The strength of force exhibits an abrupt transition upon high flagellar rotational rate driving, suggesting a coupling strength dependent collective effect akin to hydrodynamic synchronization. Difference in the force magnitude from the two bacterial carpet formed with different strain suggests that degree of hydrodynamic synchronization may depend on the mode of flagellar motions.

The sample preparation method is similar to what described elsewhere [15]. Two single polarly-flagellated bacterium strains are employed in this work. The wild type *vibrio alginolyticus* VIO5 and its mutant strain NMB136 were kind gifts from M. Homma [5]. The two strains differ in their swimming patterns. For VIO5, the flagellar rotational sense could be CCW or CW, switched with a large angle flicking motion. The typical trajectories of VIO5 are shown in Figure 7.1 (a). Abrupt changes in swimming directions take places when flagellum performs large angle flicking. Contrary to VIO5, NMB136 could only swim forward due to lack of CW flagellar rotation (Figure 7.1 (b)). The bacteria containing solution was densified to 20 folds higher in concentration (final concentration $\sim 10^{10}$ cell/μl) than its original state at the time it was harvested, before injected into a custom made 180 μm high, poly-L-lysine pre-treated micro-channel. When anchored to solid substrate, most of the cell bodies stuck to substrate while the flagellum is free to rotate. Under the dense injection condition, we seldom see tethered cell (one to two cases in a 100×100 μm^2 viewing plane) as the cell body seems to attach more favorably on the pre-treated substrate. Most of the bacteria are observed to lie flat on the substrate, probably due to the downward force induced by the interactions with boundary [8]. To make sure if the flagellar rotation for attached bacterium in a dense bacterial carpet is similar to its free swimming counterpart, we employ standard bead assay [5] with a high speed CCD camera (CR450×2, Optronis) with 1 KHz frame rate. To allow for bead assay measurement of the flagellar rotation under the above condition, solution contains low concentration of 1 μm fluorescence polystyrene bead was mixed with the bacterial solution and incubated for about half an hour before densification. Empirically, we find that, contrary to fluorescence labeled polystyrene microsphere, normal polystyrene microspheres do not tend to attach to flagellum under above treatment, probably due to worse affinity between the unlabeled surfaces to the flagellum surface. Alternatively, measuring rotational rate of the rare tethered cell also provide the required information by considering the difference in Stokes drag between flagellum and cell body [18]. Typical trajectories of tethered cell body attached are shown in Figures 7.1 (c) and 7.1 (d) for VIO5 and NMB136, respectively. NMB136 shows stable, single frequency CCW rotation. On the other hand, for VIO5, there are clearly CW and CCW motions. As *v. alginolyticus* belongs to the category of sodium-motive cells, both strains allow for precise rotational rate tuning by Na$^+$ concentration control in the motility buffer. Figures 7.1 (e) and 7.1 (f) show the measured rotational rate for each case. The distribution of CW and CCW rotation duration shift more towards CW side as Na$^+$ concentration is increased. The flagellum spends more time in rotating in CW than in CCW sense. At Na$^+$ concentration > 50 mM, flagellum spends ~ 80 percent time in CW motions (Figure 7.7 in Supplement). Furthermore, for VIO5, due to the large angle flicking motions, centers for CCW and CW motions are distinctively separated, especially at high Na$^+$ concentration. Apart from the tangential component from the rotational flagellar motions, the flicking motions introduce additional normal components in the thrust to be propagated through BOT. The NMB136 deposited bacterial carpet is an ideal experimental system for examination of theoretical model by Uchida *et. al.*, while the VIO5 deposited carpet can serve as a good reference system to check the effect on the collective hydrodynamics under different mode of flagellar motions. It is also noteworthy that we failed to form bacterial carpet with another mutant strain, NMB102, which shows CW flagellar motion only and always swims backward [19]. For NMB102, clustering of bacteria always occurs and it causes highly non-uniform bacterial carpet formation. Nevertheless, since VIO5 spends most time in rotating in CW senses at Na$^+$ concentration > 50 mM, its effect on the nearby flow field may be quite similar to NMB102.

After the flow deposition process, low concentration (average ~ 1 particle in 100×100 μm^2 view) 2 μm polystyrene particles are injected in 10 percent glycerol mixed motility buffer. As the density is matched, particles can be found at all heights in the micro-channel. As no pre-treatment was carried out for the polystyrene particle, there is no observable attachment of the 2 μm particle on flagellum in all the experiments conducted, judging from the particle trajectories. From previous study [15], we found significant sub-diffusive behavior in the lateral trajectories at height around 10 μm above the VIO5 deposited carpet by mean square displacement (MSD) measurement. The MSD converges to normal Brownian motions as measured height > 20 μm (Figure 7.8 in Supplement). The sub-diffusion observed was speculated to be correlated to the synchronous flicking motions of flagella, as data showed shorter waiting duration between two adjacent flicking when stronger sub-diffusive behavior was observed. Recent simulation

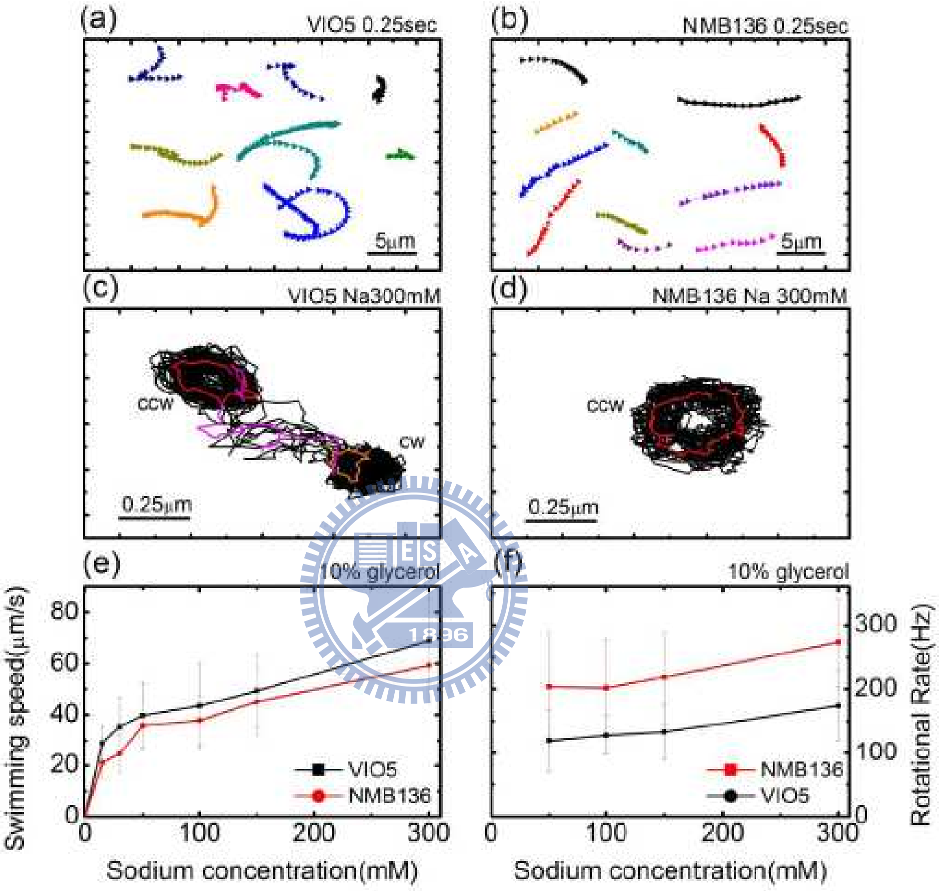

Figure 7.1: The typical trajectories of VIO5 are shown in (a). Abrupt changes in swimming directions take places when flagellum performs large angle flicking. Contrary to VIO5, NMB136 could only swim forward due to lack of CW flagellar rotation shown in (b). Typical trajectories of tethered cell body attached are shown in (c) and (d) for VIO5 and NMB136, respectively. (e) and (f) show the measured rotational rate for each case.

shows possibility of sub-diffusive behavior due to synchronous back-and-forth flicking induced forces from a matrix of rotors [20]. However, the order of magnitude of the force to be spread to the tracer particle through hydrodynamic interaction still remains unclear. Moreover, as the cell orientation on the deposited bacterial carpet is basically random, it is unclear whether a collective force could be generated and spread into the fluidic environment simply through hydrodynamic interaction.

Implementation of an optical tweezers into the above system allows us to examine the hydrodynamic spreading of force generated from the bacterial carpet. Fig. 7.2 (a) shows the schematic plot of the experiment setup. A focused 633 nm He-Ne laser is introduced into the bacterial carpet micro-channel through 60 X oil immersion microscope objective (Olympus UPLAPO, N. A. = 1.25). Calibration of laser power and strength of random noises for precise determination of effective trapping force on the 2 μm polystyrene particle was carried out under similar conditions (Figure 7.9 in Supplement). A motorized 3-D stage enables manipulation of particle positions down to precision of 0.1 μm. We purposely restrain the measurement height to above 10 μm in order to alleviate the possibility of direct contact between tracer particle and flagellum. Furthermore, as we observed, tracer particles could easily become attached to the underlying cell bodies and get stuck, if kept at a height < 10 μm. The force at each measuring location is then determined by continuously decreasing laser power until the tracer particle is no longer trapped at the laser focus [21].

Figure 7.2 (b) shows the forces measured at various heights above bacterial carpets. For NMB136 deposited carpet, a net attractive force (pulled toward to bacterial carpet surface) is measured at each height. The magnitudes of the forces decay as distances from bacterial carpet increase. Increase of Na^+ concentration in the motility buffer to above 100 mM leads to significant increase in the force magnitude. On the contrary, VIO5 deposited carpets result in net repulsive forces (pushed away from bacterial carpet surface). Interestingly, fitting of all curves render a force form inversely proportional to cubic power of distance. As shown in the inset of Figure 7.2 (b), normalizations of each curves with respect to the force magnitude measured at 10 μm respectively lead to collapse of data points into one curve with power $= -3$. On the other hand, no detectable force can be measured in the lateral directions using this methodology, for all cases (Figure 7.10 in Supplement).

The above observation suggested that flow field induced by bacterium with rotating flagellum attached on substrate may be explained by a superposition of

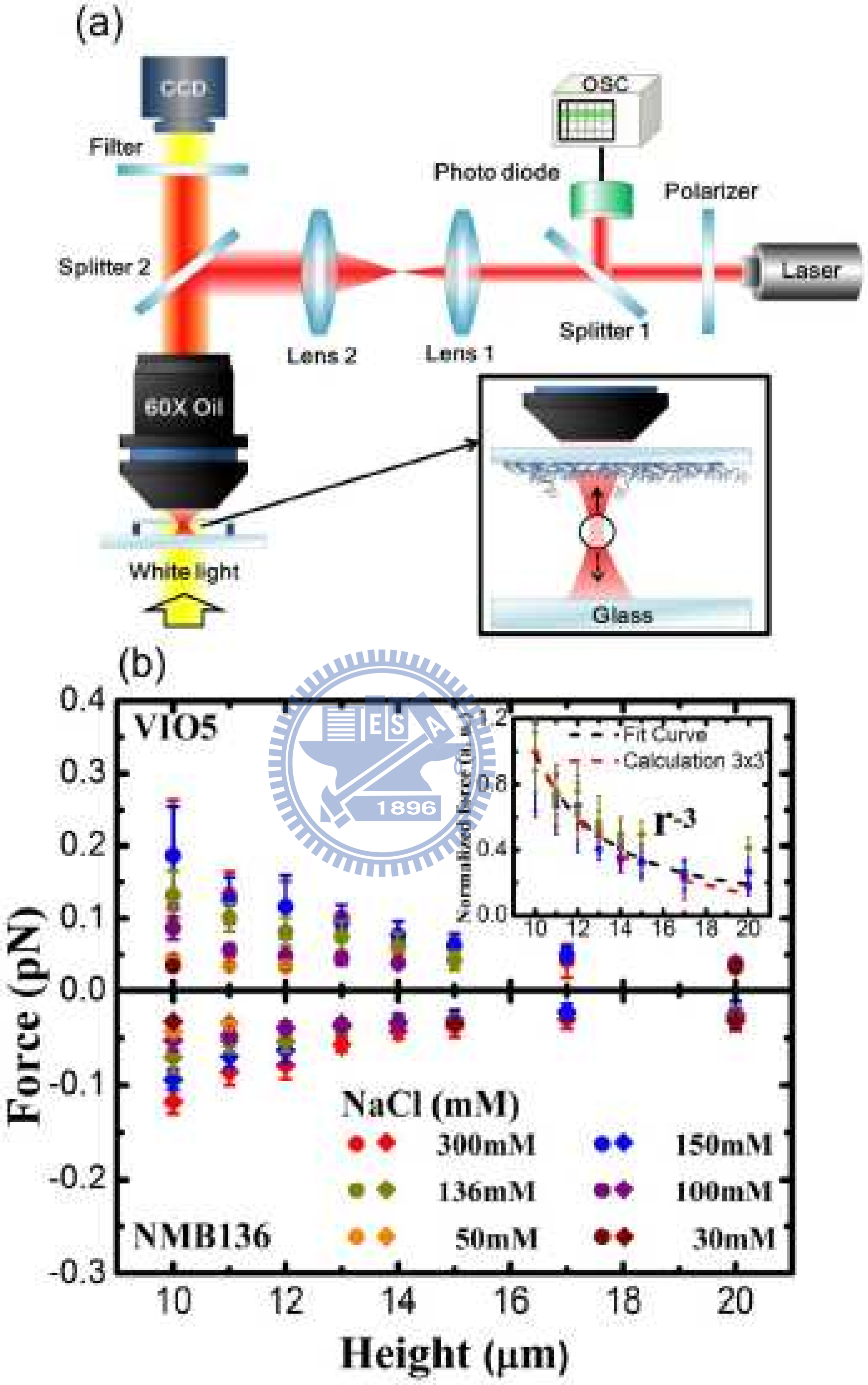

Figure 7.2: (a) shows the schematic plot of the experiment setup. (b) shows the forces measured at various heights above bacterial carpets.

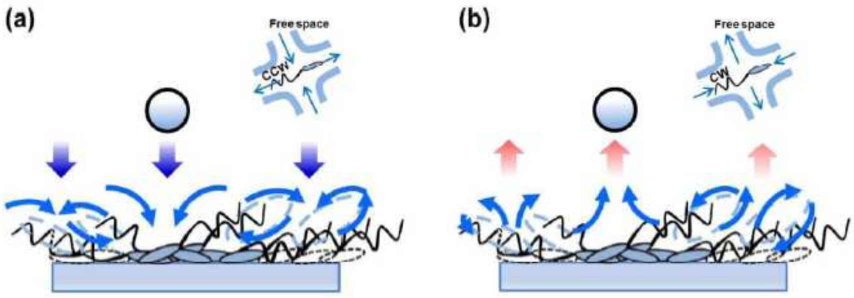

Figure 7.3: The distortion of flow fields may be pictured as the schematic plots in (a) and (b).

fields due to the anchored force monopole and its associated image flow fields located on the other side of the surface. It is known that the image system for a force monopole parallel to a no-slip surface includes anti-force monopole, force doublet, and source doublet terms [8, 23]. Physically, the anchoring of cell body leads to vanishing of the forward flow field for a force dipole model used in free space due to symmetry breaking and the close proximity of the surface boundary inevitably results in back-flowing of the towards-surface flow components in the flow field. Moreover, in bacterial carpet condition, the cell to cell distance between each bacterium constitutes additional boundary condition that promotes bending of flow lines. Considering the above scenarios, the distortion of flow fields may be pictured as the schematic plots in Figure 7.3, where a far field velocity field with force quadrupole or source doublet like behavior is expected.

The force measured by the optical tweezers-microbead assay is time averaged result of such forces over a period > 0.1 sec, according to the temporal resolution limit of the instrumentation. Experimentally, the measured force curves can be fitted by

$$F(r) = \frac{\alpha}{r^{\beta}}, \tag{7.1}$$

with β ranging from 3.01 $\sim$ 3.02. The numerical calculation also gives force curve with inverse cubic law, for 3×3 MFR matrix (cluster) case, as the dashed line plotted in the inset of Figure 7.2 (b). We extract the coefficient α for each Na^{+} concentrations. The Na^{+} concentration effects on flagellar rotational rate and torque exerted on the surrounding fluid is well documented [5]. In Figure 7.4, the extracted values are plotted versus rotational rate measured under the dense bacterial carpet conditions. The curve can be well fitted with a Boltzmann

Sigmoidal function with

$$\alpha \propto \frac{1}{1+\exp\left(-\gamma(\omega-\omega_c)\right)} \tag{7.2}$$

where γ is a strain dependent coefficient. The curve shows a phase transition like behavior. Upon a critical ω_c, the force spread through hydrodynamic coupling increase abruptly. Similarly, as plotted in the inset of Figure 7.4, the force curves with respect to sodium concentration (χ) also show sigmoidal form. From the above measurement, it is possible that at high rotational rate, each flagellum exerts stronger thrust to the surrounding fluid, results in stronger hydrodynamic coupling between neighboring flagella, and leading to phase locking between each flagellar rotation. The numerical calculation also supports this scenario above. Under reasonable parameters assigned, each rotor's rotational rate can speed up about 2 times when a considered 3 × 3 MFR matrix (cluster) enters into the synchronization state (Figure 7.6). The observation is reminiscence of theoretical simulation by Uchida *et. al.* [12], where reduction of noise level leads to more pronounced synchronization in rotor matrix. Similar concept has been shown recently in Koumakis *et. al.* [24] where phase synchronization of rotating colloidal particles occurs more easily when the rotational speeds become faster due to stronger hydrodynamic coupling from the neighbors. Our force measurement result shares the common features and may be attributed to the hydrodynamic synchronization of flagellar rotations when rotational rate exceed a threshold value. Nevertheless, further experimental and theoretical works are needed in order to clarify the statement above.

The force generated from the bacterial carpet in micro-channel may present opportunity for flow manipulation in microfluidic devices. For instance, the attractive force from a rotor carpet may be utilized for decontamination of solution. Alternatively, by engineering the relative angles of channel walls, the repulsive force from carpet can be utilized for flow pumping enhancement. Our work demonstrate the possibility of such collective flow patterns, which hopefully could pave the way for more sophisticated manipulation scheme in microfluidics devices.

In conclusion, we experimentally demonstrate the collective force generations through hydrodynamic coupling from randomly oriented bacterial carpet matrix. The senses of flagellar rotational motions determine the direction of forces. Attractive and repulsive forces are generated from carpet deposited with bacterium

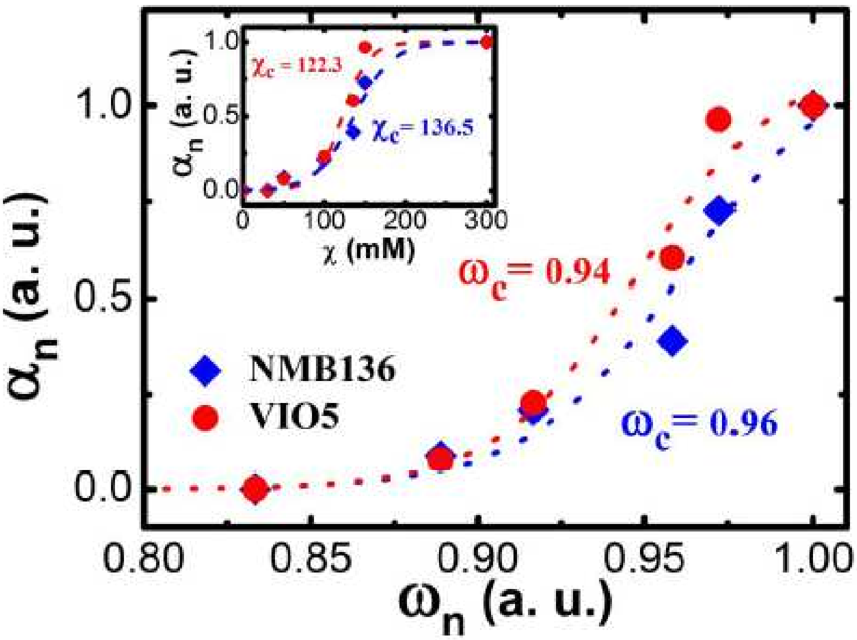

Figure 7.4: The extracted values are plotted versus rotational rate measured under the dense bacterial carpet conditions.

strain with CCW and CW flagellar rotations, respectively. The forces show behavior r^{-3}. The collective backflows from boundaries (image force monopole) are attributed to the generation of force quadrupole or source doublet like force form. Significantly stronger forces are detected upon increasing flagellar rotational rate by increasing Na^+ concentration in motility buffer. In particular, upon flagellar rotation rate tuning above a threshold value, phase transition like behavior is observed. The observation is attributed to probable transition to a state with synchronous flagellar rotations under stronger hydrodynamic coupling.

7.3 MFR matrix model explanation

To explain the two main experimental results (1) $F_z \propto H^{-3}$ and (2) a phase transition occurs in the plot of F_z versus ω when ω reaches a threshold. We employ the MFR_{matrix} model to explain these findings. At first let us try to explain the finding (1). If we assume the underlay MFR matrix or just assume a cluster that is constituted of finite amount of MFR members enters into the synchronization state, then the content in Chapter 6.3.1 (The circular motion mode) can be fully applied. The calculation parameter set is taken as $MFR_{matrix} = [H, b, N \times N, h, d, r, a, F_{th}, \alpha, \beta] = [10 \sim 40, b, 1 \times 1 \sim 61 \times 61, 7, 1.2, 0.5, a, F_{th}, \alpha, \beta]$.

The reasons why we specify such values to these parameter are try to mimic the real experimental situation. And because in our calculation, we just try to find the trend between F_z and H. Some parameters just affect the proportional coefficient such that they act as free parameters and are not relevant to our calculation, so here we do not mention them precisely. Figure 7.5 shows the calculation result. This figure reveals us that when the amount of MFR members $N \times N \leq 5 \times 5$, the calculated F_z decreases along with the increase of the tracer particle located height H, in almost the whole calculation range $10 \sim 40$ μm, by a power law decay with exponent about -3. This calculation result is consistent with our experimental outcome which the tracer particle located height H, varied in the range $10 \sim 20$ μm, controlled by means of optical tweezers-microsphere assay. That is the MFR matrix model implies a synchronized cluster can be established with the MFR members $N \times N \leq 5 \times 5$. This is a very reasonable magnitude, because there are many defects existing in our experimental samples, so the formation of a synchronized cluster with a large MFR members is unrealistic. But we have to notice that we also perform the calculation in the situation that the MFR cluster stays in the vortex or random phase state. We find it also gives the same result as the one which MFR cluster stays in the synchronization state. The reason is easily understood. Because that in the $\mathbf{F}(t)$ measurement, our sampling time is a little bit large. So during the sampling process each MFR member in some cluster, regardless of the cluster is in a synchronization state or in a random phase state, can sweep over all phase. After time average, we cannot distinguish the system stays in which one states. That is just base on the experimental result (1) $\mathrm{F}_z \propto H^{-3}$, it is not enough to claim the bacterium carpet has entered into some synchronization state.

Next let us consider the finding (2). Again if we assume the underlay MFR matrix or just assume a cluster that is constituted of finite number of MFR members enters into the synchronization state, then the content in Chapter 6.3.1 (The circular motion mode) can be fully exploited. Figure 7.6 illustrates the calculation result about the ratio $\frac{\omega_i}{\omega_0}$ versus the number of MFR members $N \times N$ which constitute a synchronized cluster, by utilizing the parameter set $\mathrm{MFR}_{\mathrm{matrix}} = [H, b, N \times N, h, d, r, a, \mathrm{F}_{\mathrm{th}}, \alpha, \beta] = [\times, \times, 1 \times 1 \sim 201 \times 201, 7, 1.2, 0.5, 0.1/0.3/0.5, \mathrm{F}_{\mathrm{th}}, \alpha, \beta]$. As we mentioned in Chapter 6.2.2 (Synchronization state in a uniform MFR matrix), the ratio $\frac{\omega_i}{\omega_0}$ offers an indicator to reveal the enhanced rotational rate of the studied rotor, the enhancement comes from the contribution of other synchronized MFRs acting on the studied MFR due to BOT hydrodynamic interaction. Figure 7.6 reveals that the rotational rate ω_i which is an indicator for most MFR members

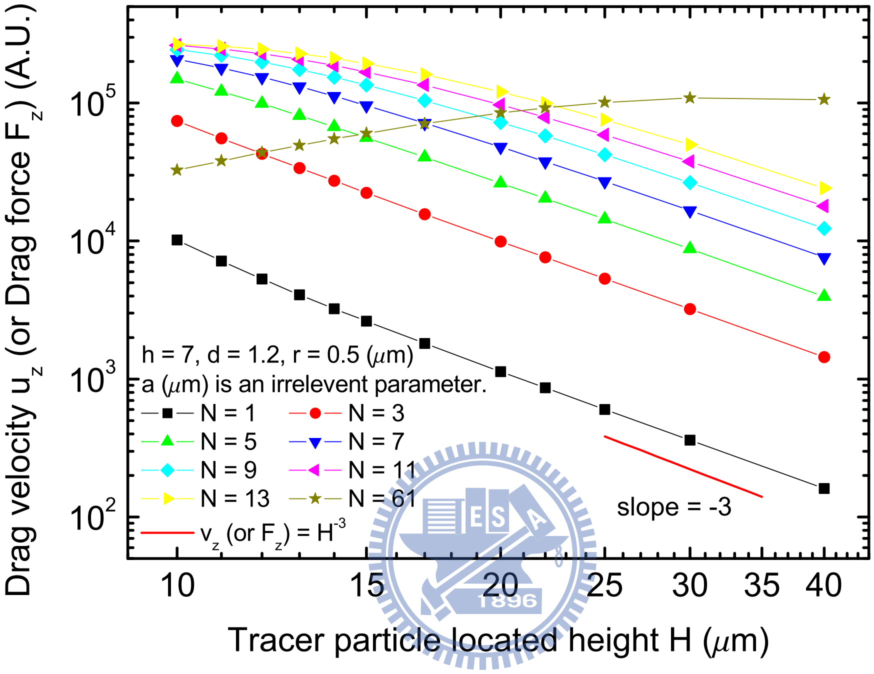

Figure 7.5: Plot of drag velocity u_z (or drag force F_z) versus tracer particle located height H. The various colored curves denote the drag velocity (equivalent to drag force) varied along with the tracer particle located height variation in case of different amount of MFR members. They are calculated by using the parameter set $\mathrm{MFR}_{\mathrm{matrix}} = [H, b, N \times N, h, d, r, a, \mathrm{F}_{\mathrm{th}}, \alpha, \beta] = [10 \sim 40, b, 1 \times 1 \sim 61 \times 61, 7, 1.2, 0.5, a, \mathrm{F}_{\mathrm{th}}, \alpha, \beta]$. Notice that in the far field situation ($H \gtrapprox 20$ μm), such relationship u_z(or F_z) $\propto H^{-3}$ is established. But in near field situation ($H \lessapprox 20$ μm), the exponent of H can vary ranged about $\approx -3.34 \sim\approx 1.35$ corresponding to $N = 1 \sim N = 61$. That is depends on the amount of MFR members $N \times N$ specified, the different exponent value is obtained.

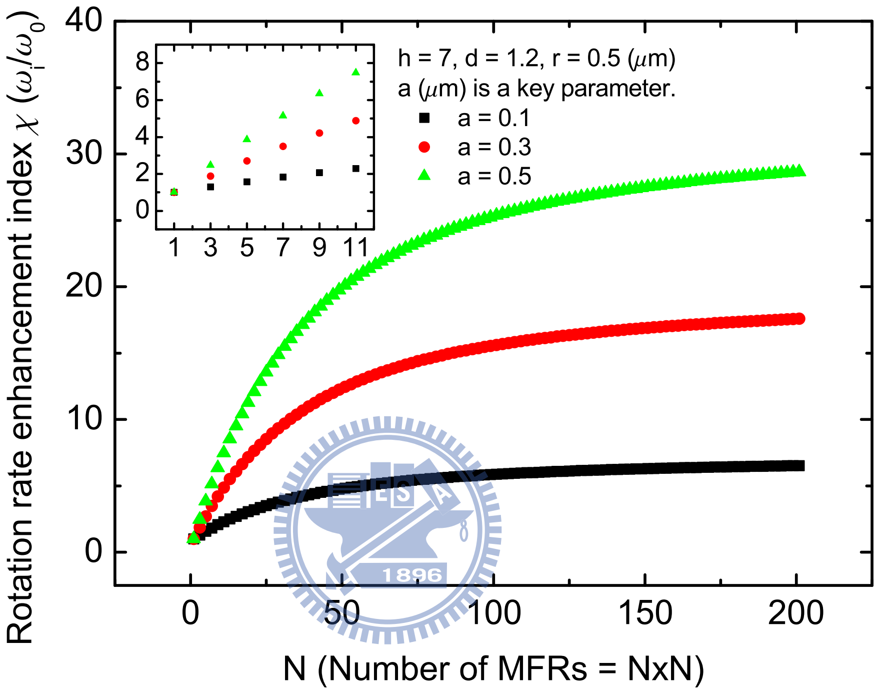

Figure 7.6: Plot of rotation rate enhancement index $\chi = \frac{\omega_i}{\omega_0}$ versus number of MFRs ($N \times N$). In this plot, we can find the bead radius of MFR arm a is a key parameter. χ increases along with the increase of a, the reason is due to the application of Stokes' law in our MFR model. Larger bead radius a corresponds to larger drag force when the drag velocity, which comes from the other surrounding MFR members, is given. Estimate and make sure the scale of a is an interesting and meaningful task by means of experimental and theoretical approaches in future.

in a synchronized MFR cluster, may increase up to several times when the amount of MFR members, says $N \times N \leq 5 \times 5$. The ratio $\frac{\omega_i}{\omega_0}$ depends on the choice of a (the radius of the MFR arm), but provided a within about the range $0.1 \sim 0.5$ μm, $\frac{\omega_i}{\omega_0}$ should exhibit a profound magnitude. We think that the bacterial flagella rotate in a real low Reynolds number fluid, the parameter a which is denoted equivalently the drag force strength acting on the bacterial flagella, is reasonable to locate in the range of $0.1 \sim 0.5$ μm. So we can suggest and assume that when the rotation rate of the bacterial flagella reaches some threshold, a cluster with the amount of MFR members $N \times N \leq 5 \times 5$ should enter into a synchronization state. The reason is due to the BOT hydrodynamic interaction, the rotation rate ω_i of most of the MFR members in the synchronized cluster should increase up to at least 2 times. Base on the Stokes' law and our MFR model, this situation means that at least 2 times of thrust strength can be exerted by each MFR member. From the same logic and calculation procedure as done for getting Figure 7.5, we can find a phase transition may appear between F_z and ω when ω reaches some threshold. So the MFR matrix model could gives us a consistent and plausible explanation to our experimental main result (2).

Finally, let us discuss a little bit about the issue of what possible reasons could cause the existence of a rotation rate threshold which makes the onset of a synchronized cluster. We offer two plausible reasons to account for this possibility. One is that after exploring the MFR model, we understand the key parameter to cause the MFR matrix entering into synchronization state is the azimuthal angle β. If β larger than some threshold which is about 40^o for almost various parameter sets employment, the synchronization state cannot be established stably. So we can imagine that fast rotation rate may shrink the azimuthal angle β. The reason is that fast rotation rate seems to benefit to push out the flow in the tangential direction $\mathbf{e}_t$ of the MFR and then shrink the azimuthal angle β. Another possible reason is that fast rotation rate seems to be able to increase the flow strength and then benefit to cause the bacteria flagella to form a bundle-like cluster or gather each other more closely. We have calculated the $\mathbf{F}_z$ by varying the rotors space d, we find a variation trend between F_z and d with the form $\mathrm{F}_z \propto \frac{1}{d}$. This calculation justifies such argument.

7.4 Supplement

Figures 7.7 $\sim$ 7.10 are some additional experimental results to verify our experiments situation.

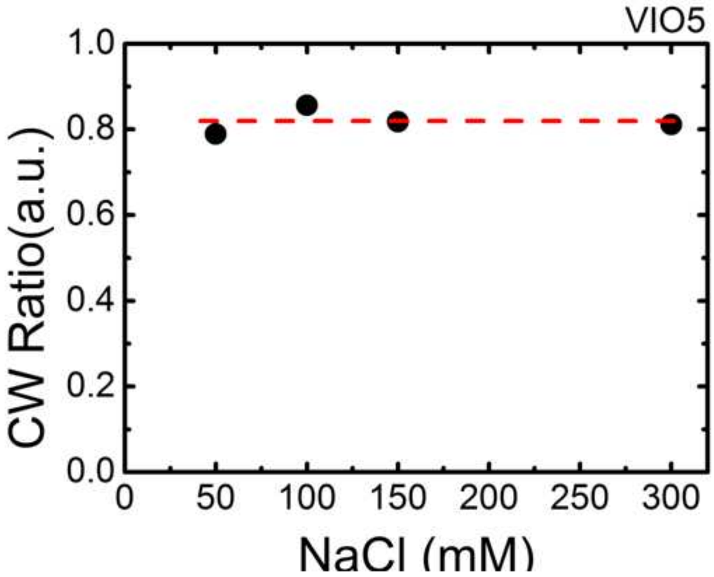

Figure 7.7: At Na^+ concentration > 50 mM, flagellum spends ~ 80 percent time in CW motions.

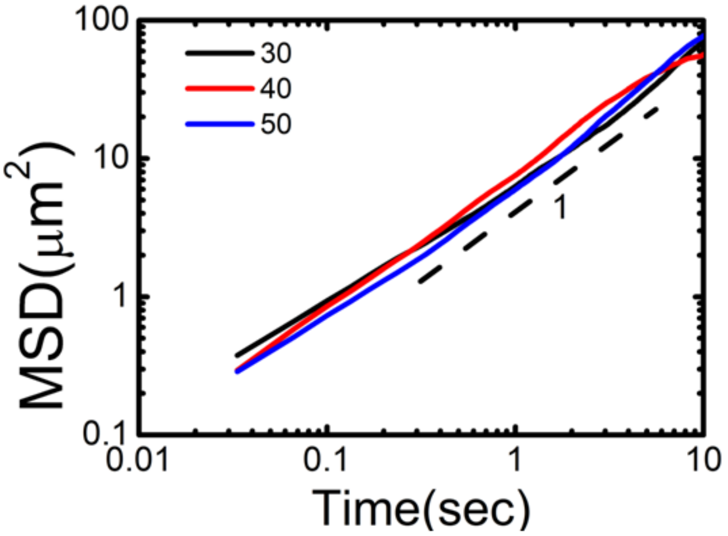

Figure 7.8: The MSD converges to normal Brownian motions as measured height > 20 μm.

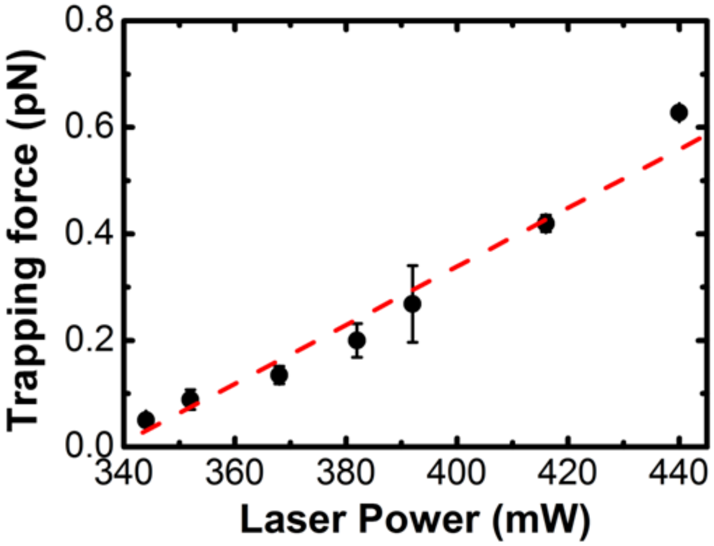

Figure 7.9: Calibration of laser power and strength of random noises for precise determination of effective trapping force on the 2 μm polystyrene particle was carried out under similar conditions.

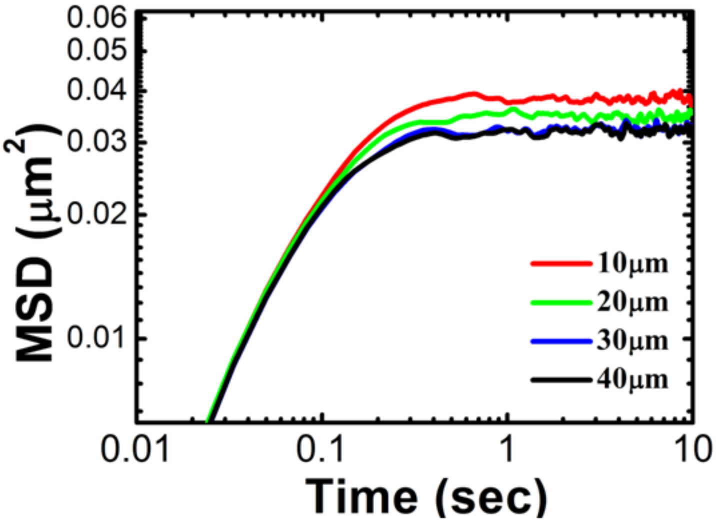

Figure 7.10: There is no detectable force can be measured in the lateral directions.

Bibliography

[1] J. Toner, Y. H. Tu and S. Ramaswamy, Annals. Phys. **318**, 170 (2005).

[2] T. Vicsek and A. Zafeiris, Phys. Rep. **517**, 71 (2012).

[3] D. L. Koch and G. Subramanian, Ann. Rev. Fluid Mech. **43**, 637 (2011).

[4] H. C. Berg, Phys. Today **53**, 24 (2000).

[5] Y. Sowa, H. Hotta, M. Homma and A. Ishijima J. Mol. Biol. **327**, 1043 (2003).

[6] L. Xie, T. Altindal, S. Chattopadhyay, X. L. Wu, Proc. Natl. Acad. Sci. **108**, 2246 (2011).

[7] Q. Liao, G. Subramanian, M. P. DeLisa, D. L. Koch and M. Wu, Phys. Fluid. **19**, 061701 (2007).

[8] A. P. Berke, L. Turner, H. C. Berg, E. Lauga, Phys. Rev. Lett. **101**, 038102 (2008).

[9] J. W. Costerton, et. al., Ann. Rev. Microbiol. **49**, 711 (1995).

[10] W. R. DiLuizo, et. al., Nature **435**, 1271 (2005).

[11] S. E. Spagnolie and E. Lauga, J. Fluid. Mech. **700**, 105 (2012).

[12] N. Uchida and R. Golestanian, Phys. Rev. Lett. **104**, 178103 (2010).

[13] N. Darnton, L. Turner, K. Breuer, H. C. Berg, Biophys. J. **86**, 1963 (2004).

[14] L. Turner, R. J. Zhang, N. Darnton, H. C. Berg, J. Bacteriol. **192**, 3259 (2010).

[15] Y.-T. Hsiao, J.-H. Wang, Y.-C. Hsu, C.-C. Chiu, C.-J. Lo, C.-W. Tsao and W. Y. Woon, Appl. Phys. Lett. **100**, 203702 (2012).

[16] M. J. Kim and K. S. Breuer, Small **4**, 111 (2008).

[17] M. J. Kim, K. S. Breuer, J. Fluid. Eng. Trans. ASME **129**, 319 (2007).

[18] S. Chattopadhyay, R. Moldovan, C. Yeung, X. L. Wu, Proc. Natl. Acad. Sci. **103**, 13712 (2006).

[19] Y. Magariyama, et. al., Biophys. J. **88**, 3648 (2005).

[20] J. Tsai, C.-H. Chang, J.-H. Wang, Y.-T. Hsiao, W. Y. Woon (unpublished private communication).

[21] M. Grimm, T. Franosch, S. Jeney, Phys. Rev. E **86**, 021912 (2012).

[22] A. Vilfan and F. , Phys. Rev. Lett. **96**, 058102 (2006).

[23] J. R. Blake, Proc. Cambridge Philos. Soc. **70**, 303 (1971).

[24] N. Koumakis and R. Di Leonardo, Phys. Rev. Lett. **110**, 174103 (2013).

自傳

(Vita)

Jengjan Tsai, a little boy who always feels and keeps interests in surrounding world. He is a lucky boy who owns some sensitive senses and a little bit talent to feel and realize the so complex world.

A Chinese motto says “生也有涯，知也無涯”... This little boy really realizes the deep meaning of this motto. Well…, although his life is so limited, he still tries to reveal and enjoy the so deep and broad world during his life. Wish this little boy can reveal more mysteries of the colored world and enjoy the wonderful world in his so short life. Go ahead! Little boy Jengjan~~